UNIVERSITÀ DEGLI STUDI ROMA TRE

DIPARTIMENTO DI MATEMATICA E FISICA

DOTTORATO DI RICERCA IN FISICA

XXX CICLO

REGIONAL IONOSPHERE CHARACTERIZATION THROUGH VERTICAL AND OBLIQUE RADIO-SOUNDING DATA ASSIMILATION

Candidato
Dario Sabbagh

Relatore interno
Prof. Vittorio Sgrigna

Relatore esterno
Dr. Carlo Scotto

Abstract

The knowledge of the physical state of the ionosphere is important in many technological applications involving radio signals, such as HF frequency radio communications, over-the-horizon radar techniques and Global Navigation Satellite Systems (GNSS). For this reason, the study of phenomena of solar origin that produce variations in the magnetic fields and the plasma in the space around the Earth (Space Weather) has acquired increasing importance. In the attempt to mitigate its harmful effects on technological systems, many efforts are being directed to the development of prediction models of short-term disturbances of the ionosphere, which make use of data assimilation techniques. For the assimilation in these models, there is a growing interest in collecting real-time ionospheric data.

Despite the development of numerous methods of investigation, which make use both of satellite and ground-based instruments, the vertical radio-sounding technique is still the most used one, thanks to the worldwide network of modern ionosondes, which can provide vertical ionograms in a digital format, and the use of software for their automatic interpretation (autoscaling). Another possibility is to direct efforts to allow also the oblique radio-sounding technique to be used for ionospheric monitoring purposes, through the autoscaling of oblique ionograms. Some advantages of this technique are the possibility to obtain information on the ionosphere in large geographical areas, corresponding to the radio propagation channel between the transmitter and the receiver, and to provide them on areas where ionosondes for vertical radio-soundings cannot be installed, as over oceans and desert areas.

This work is focused on the development of a regional 3D ionospheric model able to ingest vertical and oblique radio-sounding data, and on achieving improvements on oblique ionograms autoscaling.

The Regional Assimilative Three-dimensional Ionospheric Model (RATIM) has been firstly developed to ingest vertical plasma frequency profiles $f_p(h)$ and tested over the Italian area, using data from the ionospheric stations of Rome (41.8º N, 12.5º E), Gibilmanna (37.9º N, 14.0º E) and San Vito dei Normanni (40.6º N, 18.0º E). It is constructed based on empirical values for a set of ionospheric parameters over the considered region, some of which can vary in order to fit the actual ionospheric condition through an assimilation procedure. The procedure consists in minimizing the root-mean-square deviations (*RMSD*s) between the observed and modeled values of $f_p(h)$ at the points where observations are available.

The interest has been to obtain and verify appropriate capability to adapt to any ionospheric condition. For this reason, the model has been tested in quiet and disturbed conditions, and during day-time and night-time hours in different seasons, having selected two different periods during June-July 2013, and February 2014. A further test has been performed during the March 20, 2015 partial solar eclipse over Italy, improving the model performance by adding new empirical formulations for the ionospheric critical frequencies during solar eclipse conditions.

The model has been then applied to the Japanese-South Korean region, where oblique radio-soundings are systematically performed. The data used are vertical ionograms recorded at Jeju (South Korea, 33.4° N, 126.3° E) and Icheon (South Korea, 37.1° N, 127.5° E), and oblique ionograms recorded between Kokubunji (Japan, 35.7° N, 139.5° E) and Icheon, from which autoscaled Maximum Usable Frequency (MUF) values are ingested. Assimilating data from oblique radio-soundings is in fact of particular interest. Furthermore, the combined ingestion of vertical and oblique radio-soundings data is often possible when oblique radio-soundings are performed, thanks to the availability of vertical data at the receiver and the transmitter.

As the quality of Kokubunji-Icheon test-mode oblique ionograms is still poor, improvements on autoscaled MUF values reliability have been obtained before applying the assimilation procedure. Several filters have been applied to the ionograms to reduce the noise before autoscaling the MUF values by the Oblique Ionogram Automatic Scaling Algorithm (OIASA). Eventually, a procedure made by the combined use of OIASA and Autoscala programs has been applied to reduce the percentage of wrong MUF estimates. This procedure makes use of the conversion of oblique ionograms in vertical equivalent ones to be processed by

Autoscala, and it has shown good results when applied to a set of high-quality oblique ionograms recorded in Australia during 2015.
A procedure for the MUF assimilation in RATIM has been then proposed and applied to MUF values autoscaled by OIASA from the Kokubunji-Icheon oblique ionograms. Applying an ionospheric ray-tracing technique based on the ray equation, simulated values of the ground range for Kokubunji-Icheon radio-link have been obtained from the MUF provided by OIASA. A simplified ionosphere between the transmitter and the receiver, obtained starting from RATIM ionospheric representation, has been assumed. A comparison between the real and simulated ground range values is performed for each combination of the RATIM free parameters tested during the $f_p(h)$ ingestion, introducing a further condition to the $f_p(h)$ *RMSD* minimization. When applied to ionosonde data recorded in oblique radio-sounding areas, the system proposed could be used for the estimation of the regional electron 3D density distribution, making use of information from both vertical and oblique ionospheric radio-soundings.

Contents

1. The Earth's ionosphere and the Space Weather

The ionosphere is a product of the Earth-Sun interaction, representing a natural plasma created by the ionization of the neutral upper atmosphere, essentially due to solar radiation. The existence of an ionized layer in the upper atmosphere able to reflect radio waves back to the Earth surface was postulated by A.E. Kennelly and O. Heaviside in 1902, to explain long-range radio transmissions carried out by G. Marconi in 1901 across the Atlantic Ocean. In 1926, E. V. Appleton and M.A.F. Barnett in England, and G. Breit and M.A. Tuve in U.S.A (Appleton, 1947) experimentally verified the existence of such a reflective conductive region, transmitting vertical short radio impulses and measuring the time delays of the reflected echoes.
The reflection of radio waves in the ionosphere is due to the coherent oscillation of free electrons in response of the oscillations of the wave electromagnetic fields. Nevertheless, although the proportion of free electrons present in the Earth's ionosphere is sufficient to significantly affect radio wave propagation, the ionospheric plasma is actually weakly ionized, being neutral atmospheric particles still outnumber free electrons by not less than 1000:1. Extended approximately from 50 to 2000 km, the Earth's ionosphere consists thus in a partially ionized plasma region embedded in the Earth Magnetic Field (EMF), which affects its properties, and strongly coupled with the neutral atmosphere and the overlying magnetosphere through continuous exchange of momentum and energy.
The strong influence on the refractive index for radio waves is the most important feature of the ionosphere, as its reflection and radio propagation properties have quickly led to the widespread use of the long-distance HF radio communications for civil and military purposes all over the world (Kirby et al, 1934; Yeang C., 2004). Nowadays, numerous further technological applications exploit the propagation of radio waves through the ionosphere, like over-the-horizon radar techniques and Global Navigation Satellite Systems (GNSS). For the influence of the physical state of the ionosphere on the performance and reliability of such systems, it is crucial to understand the ionospheric behaviour in every condition. Long-term variations and correlations with solar cycles are well understood (Rawer K., 1963), while short-term variations are still object of study, with real-time data analysis providing a description of the ionosphere within certain degrees of reliability. For this reason, also the study of phenomena of solar origin that produce irregular variations in the magnetic fields and the plasma in the space around the Earth, known as Space Weather, has acquired increasing importance. Indeed, solar emissions of extremely energetic radiation towards the Earth are the primary sources of strong ionospheric perturbations, whose prediction could mitigate their harmful effects on technological systems.

1.1 Electronic equilibrium in the ionospheric plasma

As already mentioned, the radio wave propagation through the ionosphere is affected essentially by the presence of free electrons. Indeed, both the positive and negative ions are too heavy to respond to the oscillations of the electric field carried by the radio waves at HF frequencies. For this reason, the electron density per unit volume N is commonly considered the most significant characteristic parameter of the ionosphere. Its value varies from point to point as a result of a dynamic equilibrium between different processes of production, disappearance and transport of electrons (Aminaei et al., 2006). This balance can be expressed as follows:

$$\frac{dN}{dt} = q - l + d, \tag{1.1}$$

where q is the production rate of electrons, l is the disappearance rate and d is the transport rate, all of them varying from point to point for each different chemical species present in the atmosphere.
The main source of ionization is solar EUV, UV, and X-ray radiation (Hargreaves et al., 2007; Frank-Kamenetsky and Troshichev, 2012), but magnetospheric electric fields and particle precipitation also have

a significant effect (Hargreaves, J.K., 2010). Energetic particles are primarily of solar origin as well, although to a lesser extent they come from the Galaxy, the magnetosphere and the ionosphere itself. They can precipitate as a result of perturbations in the Van Allen radiation belts, or penetrate beyond the magnetosphere in the auroral zones, following the EMF lines. Particularly at low and middle latitudes, the largely predominant production process is the photoionization of the atmospheric gases by the solar photons with energy $h\nu$ high enough to dislodge electrons from neutral gas atoms or molecules upon collision. The process can be described as follows:

$$X + h\nu \longrightarrow X^+ + e^-, \tag{1.2}$$

where:

$$h\nu \geq E_{\text{ion}}, \tag{1.3}$$

being X a neutral gas atom or molecule, ν the frequency of the ionizing radiation, and E_{ion} the ionization energy. Under simplifying hypothesis, the theory of the photoionization in the Earth's atmosphere was developed by Chapman (Hargreaves, 1992), with the photoionization rate q assumed proportional to the intensity I of solar radiation and the density n of the neutral species considered:

$$q = \eta\sigma nI, \tag{1.4}$$

being σ the absorption cross-section, and η the ionization efficiency, that is the fraction of the absorbed radiation that goes into producing ionization. Considering a plane stratified atmosphere, composed of a single gas species exponentially distributed with constant scale height H, a solar radiation in parallel rays, and a constant absorption coefficient, the Chapman production function can be expressed in a normalized form as:

$$q = q_{m0} exp(1 - z - \sec\chi\, e^{-z}). \tag{1.5}$$

Here, $z = (h\text{-}h_{m0})/H$ is the reduced height for the neutral gas, χ is the solar zenith angle, h_{m0} is the height of maximum production rate when the Sun is overhead ($\chi = 0$), and q_{m0} is the production rate at h_{m0}. As shown in Fig. 1.1, the height variation of q is governed by the interplay between the decreasing n and the increasing I with increasing h. This leads to the formation of a production layer, the maximum of which occurs at a height where the radiation is still sufficiently intense to yield a large amount of ionization and the gas density becomes large enough to absorb a significant amount of the incident radiation (Prölls, 2004).
As regard the loss of freedom of the electrons, it can occur by two distinct processes. The recombination involves electrons and positive ions to form neutral atoms or molecules. It can occur directly (radiative recombination), with the final release of electromagnetic energy, following the scheme:

$$X^+ + e^- \longrightarrow X + h\nu. \tag{1.6}$$

However, it occurs much more frequently in a two-stage process, in which a positive charge is exchanged between a positive ion and a molecule, with the formation of a new ion, which subsequently dissociates through recombination with an electron, with the final formation of a couple of neutral atoms (dissociative recombination). This process can be described as follows:

$$X^+ + A_2 \longrightarrow AX^+ + A, \tag{1.7a}$$
$$AX^+ + e \longrightarrow A + X, \tag{1.7b}$$

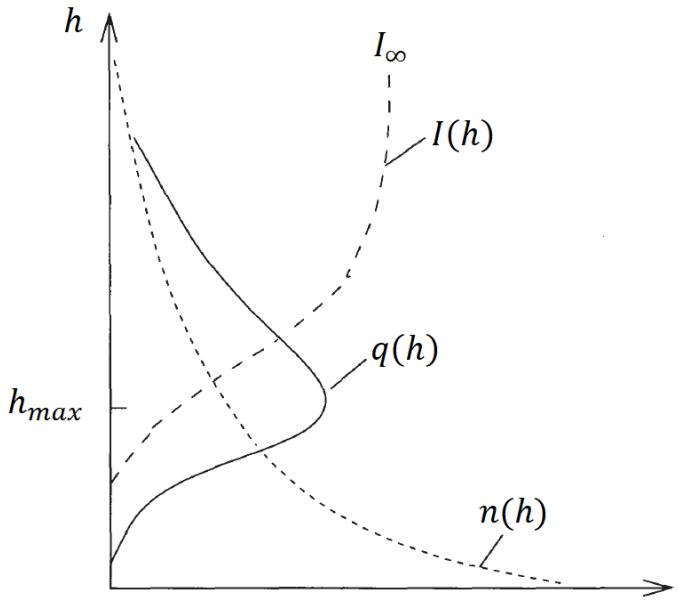

Fig. 1.1. Interplay between $I(h)$ and $n(h)$ in the formation of an ionization production layer (Prölls, 2004).

where A_2 is one of the common molecular species like O_2 and N_2. Conversely, in a capture process a free electron and an atom or molecule join to form a negative ion, with final release of electromagnetic energy:

$$X + e^- \longrightarrow X^- + h\nu. \tag{1.8}$$

The differences in relative abundances of distinct atmospheric constituents from point to point result in a layering of the ionosphere with altitude, as barometric laws have a strongly dependence with height. The best way to represent the ionospheric layers is considering them as peaks in ionization levels, in which *N* slowly increases with height, reaching a maximum after which it drops abruptly with further increasing altitude. The resulting typical *N* vertical profile presents an absolute maximum around 250-300 km, which commonly divide the ionosphere into two parts, known as bottom-side and top-side, namely the regions underlying and overlying the *N* absolute maximum, respectively. The bottom-side is stratified in different layers dominated by different processes and elements population.

In the mesosphere (D region), the ion-electron production is dominated by UV and X-ray wavelengths, being NO^+ the predominant ion component. The ionization level in this region is very low, with *N* not greater than 10^9 m^{-3}, and chemical and dynamical processes are dominated by the neutral component, responsible of strong absorption of HF radio waves below 90 km altitude. EUV ionizing component dominates in the lower thermosphere (E region), where molecular oxygen O_2 is mainly ionized, while above 150 km (F region) ionization of the lighter atomic oxygen O dominates. During day-time, this region can split in two different layers (F_1 and F_2), being the F_2 layer considered the most important ionospheric region, as it is the densest plasma in the near-Earth space, with *N* up to 10^{12} m^{-3}. However, it is also the layer most difficult to understand and model, as it does not follow the behaviour described by the Chapman theory. At higher altitudes, the number of O^+ ions decreases and lighter ions such He^+ and H^+ become dominant. *N* begins to monotonously decrease as well, and the top-side ionosphere slowly fades into the overlying plasmasphere, or inner magnetosphere. It is noteworthy that sometimes *N* values even higher that the maximum value in the F_2 region may occur at heights typical of E region. This arises because of the occasional formation of so-called sporadic E (E_s) layers, corresponding to strong peaks of ionization, whose occurrence is generally irregular and not predictable.

Being generated by radiative interaction with the Sun, the ionospheric properties variation is closely related also to solar activity, latitude, seasons, and hour, mainly due to the variation of χ. Moreover, ionospheric structure varies significantly from day to night, being solar photons the major ionizing factor. By way of

example, typical day-time and night-time vertical electron densities profiles in the mid-latitude ionosphere are shown in Fig. 1.2, in different solar activity conditions.

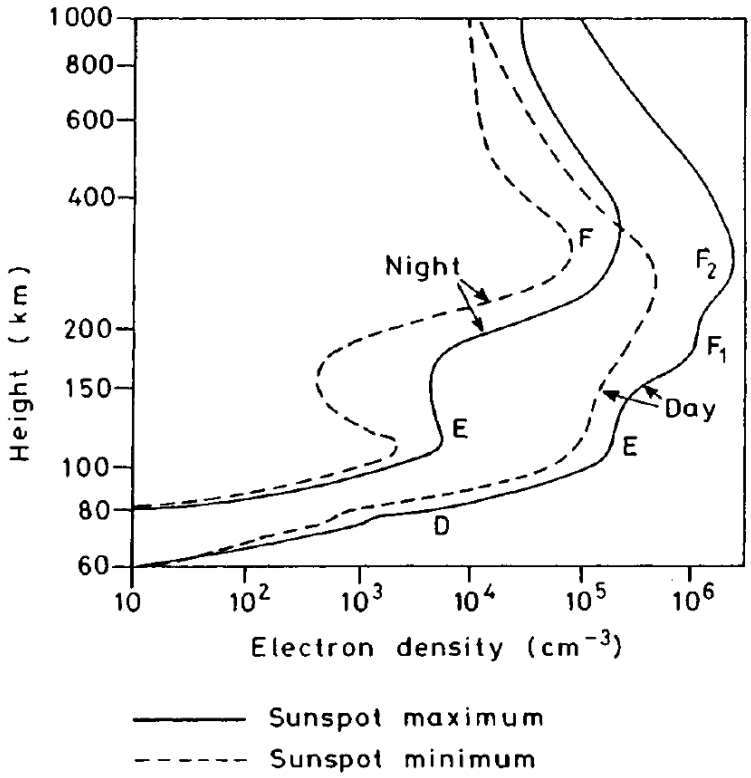

Fig. 1.2. Typical vertical profiles of electron density in the mid-latitude ionosphere (Hargreaves, 1992).

However, the time and geographical variation of some ionospheric features depart from the somehow expected behaviour. An example of such anomaly in regular variation is the so-called winter anomaly, which consists in greater day-time maximum electron densities N_mF_2 in winter than in summer. Other anomalies are related to the particular orientation of the EMF in specific Earth's regions, like the equatorial or Appleton's anomaly, for which the ionization does not maximise exactly at the magnetic equator but in the zones at magnetic latitude between 10° and 20°, and –10° and –20°. This arises because of the phenomenon known as fountain effect, which redistributes part of the electrons present in the equatorial lower ionospheric layers to the higher ionospheric layers in those regions.

1.2 Space Weather effects on the ionosphere

Sun-Earth interactions are not only responsible of the formation and sustaining of the Earth's ionosphere through the Sun's regular radiative emission, but are also the origin of strong geomagnetic and ionospheric disturbances. Indeed, the Sun emits energy also as a continuous stream of charged particles, known as solar wind. The solar wind travels at over 500 km/s, carrying parts of the Sun's magnetic field into space and toward Earth, where it is deflected by the EMF. However, both electromagnetic and particles emissions from the Sun suffer strong irregular variations, which can pose a serious threat to space-borne and ground-based technological systems, and can endanger human life or health. These phenomena are those of interest for the Space Weather studies. As summarized in Fig. 1.3, Space Weather effects on Earth include disrupting HF radio transmissions, damaging power grids, threatening satellite transmissions and instruments, affecting avionics in extreme circumstances, and reducing the useful life of satellites in low Earth orbits (LEO). Even long-distance pipelines can be put at risk by reducing the efficiency of anti-

corrosion cathode systems. Thus, as reliance on technology grows, so does the impact of Space Weather events in human life.

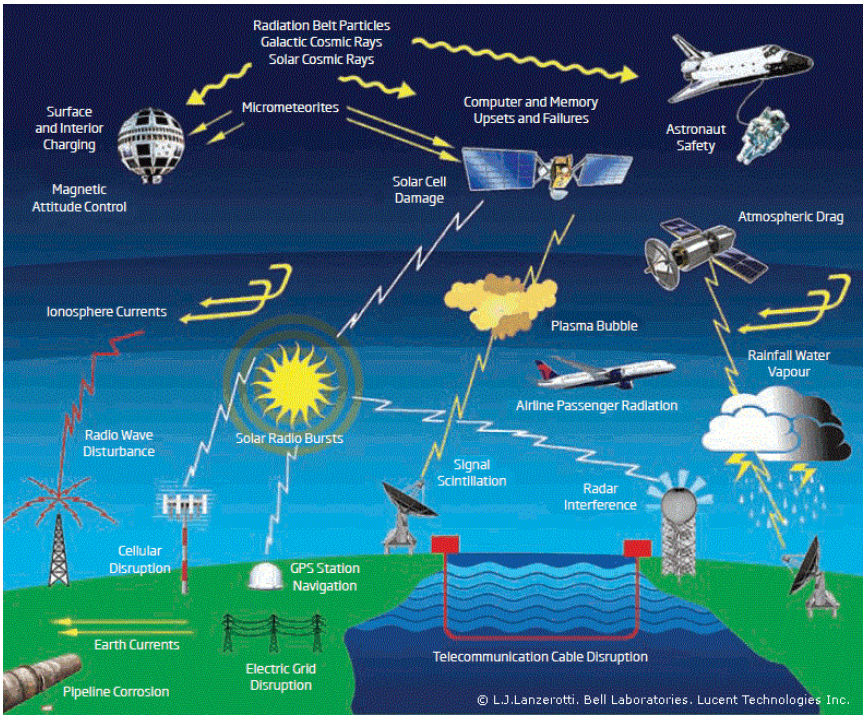

Fig. 1.3. Scheme representing the main Space Weather effects on modern technologies and human activities (https://www.metoffice.gov.uk).

Violent solar events, such as flares and Coronal Mass Ejections (CMEs), are the primary sources of Space Weather effects on Earth. Solar flares consist in intense releases of energy into the outer space as electromagnetic radiation, which travels at the speed of light, and electrically charged particles, which travel slower. They are classified based on X-ray energy, being the classes of highest peak flux in the wavelength range 1 to 8 Å the C-Class (10^{-6}-10^{-5} W/m^2), M-Class (10^{-5}-10^{-4} W/m^2), and X-Class (greater than 10^{-4} W/m^2). The CMEs, instead, are intense solar events characterized by huge bubbles of plasma ejected from the Sun that speed into space. Often associated with solar flares, they occur over large sunspot groups and typically reach Earth in 1 to 5 days after the eruption from the Sun.

As CMEs disrupt the flow of the solar wind, they produce disturbances that can strike the Earth with sometimes catastrophic results. Indeed, sometimes CMEs are expected to trigger geomagnetic storms on Earth, which are associated to the most severe ionospheric disturbances. When a travelling CME reaches the Earth at speeds up to 2500 km/sec, the EMF deflects the billions of tons of plasma carried into its solar wind, protecting the Earth from most of its harmful effects. Then, particles enter in the EMF where field lines reconnect at the geomagnetic tail, and follow field lines towards the Earth. Hence, the interaction between the magnetic fields of the solar wind and the Earth transfers an increased energy into the magnetosphere, causing an increase in movement of plasma and in electric currents in the magnetosphere and ionosphere.

Strong perturbations in the ionospheric plasma can be triggered by energetic solar events. Sudden Ionospheric Disturbances (SID) consist in abnormally high ionization in the D region, caused by UV and X rays released by a flare. Polar Cap Absorptions (PCA), instead, are episodes of increased ionization of the D and E layers at polar latitudes, due to the penetration into the atmosphere of fast protons and α particles from solar flares along the magnetic field lines of the Earth. Finally, negative and positive ionospheric storms associated to slower protons and electrons in a CME can occur at every latitude, with electron density depletion or increase, respectively.

Some common consequences of such events include auroral displays at much lower latitudes than normal, and fading and spreading of the radio signals at low and high latitudes. Sudden increase in radio-wave absorption in MF, HF and VHF bands can also occur, causing interruption or degradation of radio communications. Depending on the density of the electrons, their range of movement, the frequency and amplitude of the radio waves, the effects can range from total absorption of the radio waves to selective reflection and phase delays (Pillet G., 1960; Stauning P.,1998; Sauer et al., 2008). GNSS systems can be strongly affected by changes in the radio signals speed, causing increased range errors, and by scattering effects at low and high latitudes, known as ionospheric scintillations, which can cause loss of tracking. Moreover, the ionosphere also responds to thermospheric winds, which can push the ionosphere along the inclined magnetic field lines to a different altitude. During a geomagnetic storm, the energy input at high latitudes can produce waves and changes in thermospheric wind composition, resulting in significant variations in the ionospheric behaviour.

References

[1] Appleton, E.V. The ionosphere. Nobel Lecture, 1947.

[2] Kirby, S. S., Berkner, L. V. and Stuart, D. M. Studies of the ionosphere and their application to radio transmission. Part of Bureau of Standards Journal of Research, vol. 12, January 1934.

[3] Yeang, C., 2004. Characterizing Radio Channel: The Science and Technology of Propagation and Interference, 1900-1935.

[4] Rawer, K., Meteorological and Astronomical Influences on Radio Wave Propagation, 1963. Academic Press, New York.

[5] Aminaei, A., Honary, F., Kavanagh, A. J., Spanswick, E., Viljanen, A., 2006. Characteristics of night-time absorption spike events, Ann. Geophys. 24, 1887-1904.

[6] Hargreaves, J. K., Birch, M. J., and Bromage, B. J. I., 2007. D- and E-region effects in the auroral zone during a moderately active 24-h period in July 2005, Annales Geophysicae, 25, 1837-1849.

[7] Frank-Kamenetsky, A. and Troshichev, O., 2012. A relationship between the auroral absorption and the magnetic activity in the polar cap, Journal of Atmospheric and Solar-Terrestrial Physics, 77, 4045.

[8] Hargreaves, J.K., Auroral radio absorption: The prediction question, 2010. Adv. Space Res. 45, 10751092.

[9] Hargreaves, J.K., 1992. The solar-terrestrial environment. An introduction to geospacer - the science of the terrestrial upper atmosphere, ionosphere and magnetosphere. Cambridge University Press, Cambridge, Great Britain.

[10] Prölls, G.W., 2004. Physics of the Earth's Space Environment. An Introduction. Springer-Verlag Berlin Heidelberg, Berlin, Germany.

[11] Pillet, G., 1960. Contribution a l'etude de l'absorption ionospherique sur une frequence fixe. Annales des Telecommunications.

[12] Stauning, P., Substorm modeling based on observations of an intense high-latitude absorption surge event, 1998. Journal of Geophisical Research 103 (A11), pages 26,433-26,452.

[13] Sauer, H. H. and Wilkinson, D. C., 2008. Global mapping of ionospheric HF/VHF radio wave absorption due to solar energetic protons. Space Weather 6, S12002, doi:10.1029/2008SW000399.

2. Vertical and oblique ionospheric HF radio-soundings

Ever since the first experimental results verified the existence of ionized layers in the upper atmosphere, the Earth's ionosphere has been observed from ground more and more systematically. Particularly in the years before 1958, the international geophysical year, the number of observatories equipped with HF-band radars able to perform vertical radio-soundings to investigate the bottom-side ionosphere increased. The technique is similar to that first used in 1926 by E.V. Appleton and M.A.F. Barnett, and G. Breit and M.A. Tuve (Appleton, 1947), consisting in the automatic emission of vertical radio signals at increasing frequency in HF band, measuring the time delays of the reflected echoes. Plotting time delays against corresponding signal frequencies gives what is known as a vertical ionogram, when co-located transmitter and receiver are used. Since then, despite the development over time of numerous methods of investigation, making use of both satellite and ground-based instruments, the vertical radio-sounding technique has been remained the most used one. This is thanks to the worldwide network of modern ionosondes, which can provide vertical ionograms in a digital format, and the use of software for their automatic interpretation, or autoscaling.
An oblique ionogram can be obtained, when synchronized instruments are situated in separate locations. Although this kind of measurement is not systematically used, it can provide some interesting advantages, as it permits to obtain information in the region between the transmitter and the receiver. Since reliable software for the autoscaling of oblique ionograms has not been developed yet, directing efforts in this direction could allow also the oblique radio-sounding technique to be used for ionospheric monitoring purposes.

2.1 Vertical ionospheric radio-soundings

The vertical radio-sounding technique is the most widely applied to study the ionospheric vertical structure. It is commonly used to directly obtain the frequencies of vertical reflection by the different layers and the altitude of the layers themselves. Using a bistatic radar called ionosonde, short pulses at increasing frequency typically from 1 to 30 MHz are vertically transmitted upward, and the time delays Δt of the reflected echoes are measured. The signals are reflected at the altitude where their frequencies f satisfy the condition:

$$f = f_p, \tag{2.1}$$

where f_p is the plasma frequency, i.e. the characteristic frequency of the free oscillations of electrons in the ionospheric plasma. f_p varies from point to point accordingly to N, following the relation:

$$f_p = (2\pi)^{-1}(Ne^2/m\varepsilon_0)^{1/2}. \tag{2.2}$$

The virtual height h' of reflection of each signal is then calculated by:

$$h' = c\Delta t/2, \tag{2.3}$$

representing the altitude where the electromagnetic wave would be reflected if its velocity was the speed of light c. The result of these measurements is the vertical ionogram, which is the graph of h' against f.
Fig. 2.1 shows a typical vertical ionogram. As can be seen, two distinct traces are visible, as a result of the bi-refraction phenomena in the ionosphere. Indeed, as described by the so-called magneto-ionic theory (Ratcliffe, J. A., 1959), each radio wave travelling in a uniformly magnetized plasma will split in two characteristic waves with different polarization, called ordinary ray (or o-ray), and extraordinary ray (or x-

ray). This arises because of the anisotropy introduced by the EMF. In Fig. 2.1 the red trace (o-trace) represents ionospheric reflections of the o-ray, while the green trace (x-trace) represents reflections of the x-ray.

In Fig. 2.1 is also shown that vertical ionograms can provide important ionospheric parameters, which can be directly recognized from its traces. Indeed, each layer is represented by a portion of trace bending upward at the beginning of the layer, and ending with a vertical asymptote, or a cusp when a trace representing an overlying layer is present. The frequencies associated to the E and F_1 cusps, and to the F_2 asymptote in the o-trace, are the critical frequencies f_c of the different ionospheric layers, i.e. the maximum values of o-ray frequency that can be vertically reflected from a specific layer. Referring to the E, F_1 and F_2 layers, they are known as f_oE, $f_o F_1$, and $f_o F_2$, respectively, and are related to the maximum electron densities of each layer (N_mE, $N_m F_1$, and $N_m F_2$) through (2.2), being associated to the maximum f_p in the respective layers, in accordance to (2.1). Some other parameters which can be retrieved from a vertical ionogram are the virtual heights associated to each layer h'E, $h'F_1$, and $h'F_2$, the minimum frequency observed f_{min}, linked to the absorption in the D region, and the maximum frequency observed f_xI, often belonging to the x-trace.

Modern ionosondes provide digital ionograms equipped with autoscaling software able to give the ionospheric parameters along with the ionograms themselves in real-time. Well-known autoscaling programs are the Automatic Real-Time Ionogram Scaler with True Height (ARTIST), developed at the University of Lowell, Center for Atmospheric Research (Huang and Reinisch, 1996), and Autoscala, from the Italian Istituto Nazionale di Geofisica e Vulcanologia (INGV) (Pezzopane et al., 2009). The electron density profile $N(h)$ over the ionosonde can be obtained as well, through inversion techniques. An inversion method commonly used is the polynomial method, in which the inversion is performed representing $N(h)$ with polynomials, whose coefficients are determined from the ionogram, making use of semi-empirical models as well. The target function method is an alternative technique which generate a $N(h)$, retrieving the corresponding ionogram to be compared to the measured one, until the best fit is obtained (Scotto et al., 2012). For both the methods, algorithms have been developed for their real-time automatic execution by the autoscaling software. Examples of widely used algorithms of this type are NHPC (Huang and Reinish, 1996; Reinish et al., 2005), based on the Polynomial Analysis method (POLAN) (Titheridge, 1959, 1985, 1988), and the Adaptive Ionospheric Profiler (AIP) (Scotto, 2009). The data produced by these computer programs can be effectively integrated into real-time and short-term forecasting models (Galkin et al. 2012).

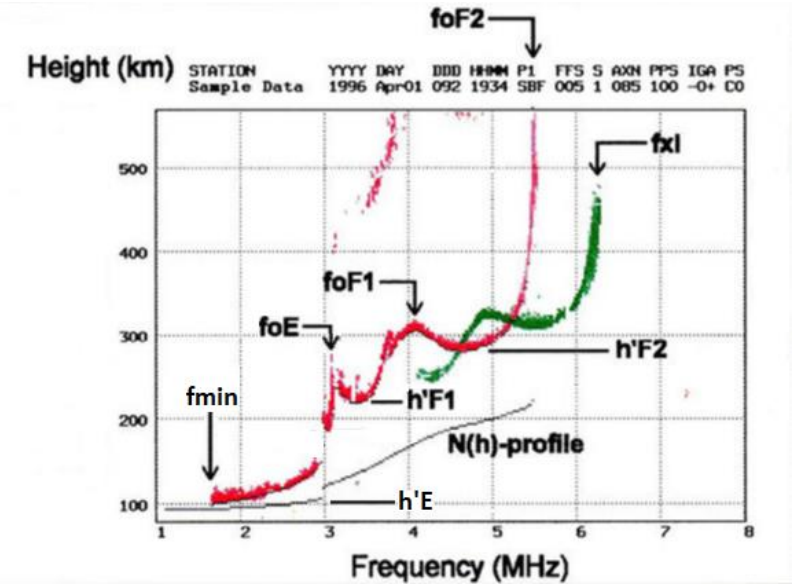

Fig. 2.1. Example of vertical ionogram (Reinisch, B.W., 2003). O-trace (in red), x-trace (in green), critical frequencies and some other ionospheric parameters observable from the ionogram are highlighted.

2.2 Oblique ionospheric radio-soundings

In an oblique radio-sounding, radio signals at increasing frequency up to 30 MHz are obliquely transmitted upward and received hundreds or thousands km apart after one or more reflections by the ionosphere and, in case, by the ground as well. Hence, the use of this technique involves two distinct ionosondes able to study how HF radio signals propagate via the ionosphere under a variety of conditions (Chen et al., 1992). After being transmitted, the sounding radio wave is continuously refracted in his path through the ionosphere because of the variation of the refractive index n in the ionospheric plasma, strictly linked to N. Since n decreases going upward in the bottom-side, in accordance with the corresponding $N(h)$ decrease, the travelling wave is continuously bent, reducing its inclination until it will be curved back toward the ground. Under simplified conditions of discrete stratification of the ionosphere, the ray-path can be deduced from Snell's law applied at each n discontinuity, when total reflection condition occurring at the critical angle of incidence.
Once each signal is detected by the receiver, the travel time Δt is measured, thanks to the accurate synchronization of the transmitting and receiving ionosondes. The group path p' associated to each signal frequency is computed from Δt, following:

$$p' = c\Delta t, \tag{2.4}$$

representing the virtual path followed by the wave as if it traveled at the speed of light c. The oblique ionogram is then produced plotting Δt or p' (usually divided by 2) against f.

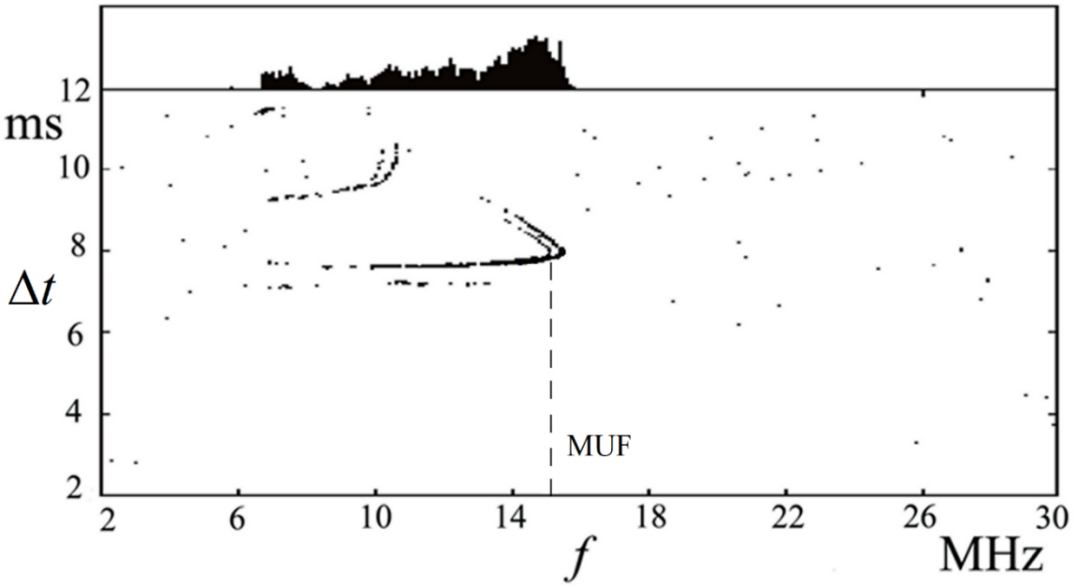

Fig. 2.2. Example of oblique ionogram. O-trace, x-trace, MUF and some other characteristic features of this kind of ionograms can be clearly recognized. (Courtesy of Alessandro Ippolito)

Fig. 2.2 shows an example of oblique ionogram, in which some typical features are present. O-trace and x-trace can be seen in an oblique ionogram as well, as a result of the bi-refraction phenomena in the ionosphere introduced by the EMF. The maximum frequency observed for the o-trace is known as Maximum Usable Frequency (MUF), representing the maximum frequency which can reach the receiver from the transmitter in the specific conditions of the sounding. As can be inferred comparing an oblique ionogram with a vertical one, frequencies far beyond the usual limits for vertical reflection can be received even thousands of km apart.

Different values of time travel can be measured for some frequency values, generating traces associated to distinct propagation modes. This arises because of the transmitters often emit signals in all direction, allowing different paths for the radio waves travelling through the receiver. Particularly for lower frequencies, it is thus possible to see traces associated to paths involving multiple reflections by different layers and the ground, with resulting higher time travels than those obtained for a single ionospheric reflection.

Another characteristic of oblique ionogram traces is the peculiar "nose" shape, for which two distinct values of time travel associated to the same propagation mode can be measured, particularly for frequencies right below the MUF. This arises because of the so-called Pedersen effect, for which signals at the same frequency can always take at least two different paths to travel between two fixed points on ground. These paths correspond to different elevation angles α of the transmitted waves, known as low ray and high ray (or Pedersen ray), associated to the low and the high permitted α, respectively. An example of these paths is shown in Fig. 2.3 for the radio-links between T and R (rays 1 and 5) and between T and Q (rays 2 and 4). The distance T-Z is known as the skip distance, representing the lower limit of the distance attainable for ionospheric propagation with that specific frequency, as signals at the same frequency transmitted with higher α will be reflected farther on ground.

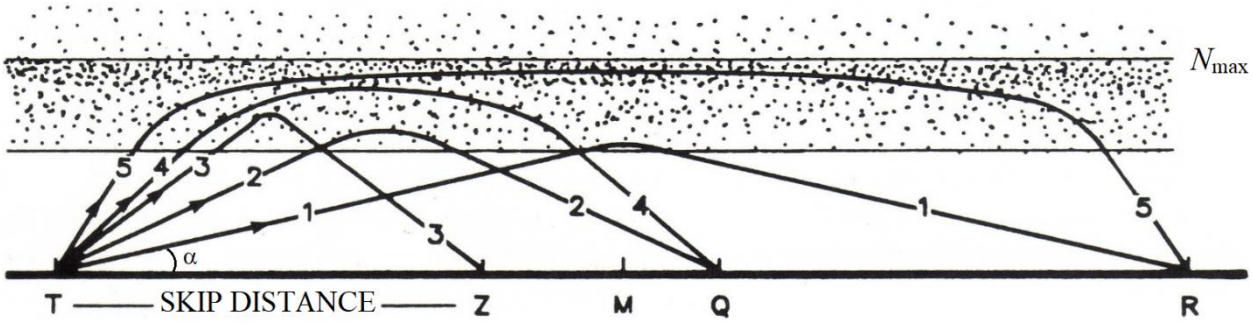

Fig. 2.3. Ray-paths of signal transmitted at fixed frequency and increasing angle of elevation (McNamara, 1991). For distances T-Q and T-R low rays (1 and 2) and high rays (4 and 5) can be discerned. Ray 3 define the skip distance T-Z for the specific radio-link and situation.

Accurately synchronized transmitting and receiving systems, and a high sensitivity of the receivers are needed to perform reliable oblique radio-soundings. Furthermore, the interpretation of oblique ionograms is much more complex than vertical ionograms, so that well-established automatic scaling techniques have not been developed yet. Although these limitations, oblique radio-soundings offer several advantages over vertical soundings for the understanding of radio wave propagation and physical parameters of the ionosphere. Indeed, oblique soundings investigate much wider regions, and can provide information on large areas where vertical soundings cannot be performed, as over oceans and deserts, or over areas inaccessible for political or military reasons. Moreover, they can provide more ionograms with less transmitting and receiving devices, as signals transmission and reception are allowed in all direction at the same time. The way radio communications via ionospheric channels work is reproduced by oblique radio-sounding, so that they can provide available communication bands and any gaps where no links can be established between the transmitter and the receiver. Hence, in the absence of software for automatic interpretation, until now oblique soundings have largely been used to understand the factors affecting propagation which will ultimately limit link reliability due to natural ionospheric variability.

References

[1] Appleton, E.V. The ionosphere. Nobel Lecture, 1947.

[2] Reinisch, B.W., 2003. HF radio sounding of geospacer plasmas, 8th International Congress of the Brazilian Geophysical Society.

[3] Ratcliffe, J.A. The magneto-ionic theory and its applications to the ionosphere. University Press, Cambridge, Great Britain, 1959.

[4] Huang, X., Reinisch, B.W., 1996. Vertical electron density profiles from the digisonde network. Adv. Space Res. 18 (6), 121-129.

[5] Pezzopane, M., Scotto, C., Tomasik, L., Krasheninnikov, I., 2009. Autoscala: an Aid for Different Ionosondes. Acta Geophysica 58, 513-526.

[6] Scotto, C., Pezzopane, M., Zolesi, B., 2012. Estimating the vertical electron density profile from an ionogram: On the passage from true to virtual heights via the target function method. Radio Sci. 47, RS1007.

[7] Huang X., Reinish B.W, 1996. Vertical electron density profiles from the digisonde network. Adv. Space Res. 18, 121-129.

[8] Reinish B.W., Huang X., Galkin I.A., Paznukhov V., Kozlov A., 2005. Recent advances in realtime analysis of ionograms and ionosond drift measurements with digisondes. J. Atmos. Sol.-Terr. Phys. 67, 1054-1062.

[9] Titheridge, J. E., 1959. The calculation of real and virtual heights of reflection in the ionosphere. J. Atmos. Terr. Phys. 17, 96–109.

[10] Titheridge, J. E., 1985. Ionogram analysis with the generalised program POLAN. World Data Center A, National Academy of Sciences, 2101 Constitution Avenue, NW, Washington, D.C. 20418 USA.

[11] Titheridge, J. E., 1988. The real height analysis of ionograms: A generalized formulation. Radio Sci. 23 (5), 831–849.

[12] Scotto, C., 2009. Electron density profile calculation technique for Autoscala ionogram analysis. Adv. Space Res. 44, 756-766.

[13] Galkin, I.A., Reinisch, B.W., Huang, X., Bilitza, D., 2012. Assimilation of GIRO data into a real-time IRI. Radio Sci. 47. http://dx.doi.org/ 10.1029/2011RS004952, RS0L07.

[14] Chen, J., Bennett, J. A., and Dysoni, P. L., 1992. Synthesis of oblique ionograms from vertical ionograms using quasi-parabolic segment models of the ionosphere, Journal of Atmospheric and Terrestrial Physics, Vol. 54. No. 3/4. pp. 323-331.

[15] McNamara, L.F., 1991. The ionosphere: communications, surveillance, and direction finding. Krieger Publishing Company, Malabar, Florida.

3. **The ionospheric modeling**

In order to provide a reliable description of the ionosphere and its evolution in space and time, numerous ionospheric models have been developed over time, for both scientific and practical purposes. Indeed, ionospheric models respond to the need to test our knowledge and improve our understanding of the ionosphere, reproducing the time and space ionospheric variations observed experimentally. Moreover, ionospheric models can be used as alternatives to direct measurements, as numerical experiments are cheaper and convenient to study various processes. On the other hand, they are precious to specify, regionally or globally, the ionospheric conditions required for the new technological systems dependent on radio signal propagation. Indeed, as mentioned in Chapter 2, the characterization of the ionospheric medium is needed as accurately as possible, since radio waves propagating through the ionosphere are affected by the Space Weather, with possible harmful effects on technological systems.

It is important to underline that there are no all-purpose ionospheric models, even though there are some characteristics all the models have in common. Indeed, all of them need some type of input data, while the output is mainly the electron density with the possible addition of other parameters, such as electron and ion temperature, ion composition, drifts, and so on. Furthermore, current ionospheric models are constantly undergoing improvements and validations for which well-established experimental databases are needed.

The models proposed over the years fall into two main categories: empirical models and physics-based models. Empirical models apply long series of data to determine the mathematical functions that describe the spatial and temporal variations. Since they are based on data, they do not rely on the use of physics. However, the analytical description of the ionosphere they provide is only climatological (that is, they are essentially median models), and it is realistic only in the areas sufficiently covered by observations. Typical data sources for empirical models are ionosondes, topside sounders, incoherent scatter radars, rockets and satellites, and being descriptive and easy to use, they are mainly used for assessment and prediction purposes.

Conversely, in physics-based models, conservation equations (continuity, momentum, energy, etc.) are solved numerically for electrons and ions as a function of spatial and time coordinates to calculate plasma densities, temperatures and flow velocities. They require solar, magnetospheric and atmospheric input parameters, and their accuracy depends on the quality and quantity of the input data, in addition to the completeness of the physics and chemistry included in the models. However, they can be powerful tools to understand the physical and chemical processes of the upper atmosphere, and, for this reason, they are mainly used for scientific studies.

In practice, empirical models are usually preferred over theoretical ones because they are available to users in the form of computer programs that require limited computing power, and their relative simplicity makes them easily adaptable to specific problems. However, neither the physics-based nor the empirical approach ignores the other. Indeed, physicists rely on observational data in developing and validating physical models and in estimating key quantities, like initial and boundary conditions. On the other hand, the construction of statistical or empirical models is guided by physics that determines the variables of interest and the data sets to be analyzed.

It should be noted here that ionospheric models suffer from all the limits of geophysical models, such as those related to the impossibility to perform controlled experiments using the Earth, the stochastic nature of the processes involved, and the difficulty to separate one physical process from the others. Moreover, the limited database available, and the errors in data used in model specifications, increase the uncertainty of both empirical and physics-based models. However, the reliability of numerical prediction is increasing, thanks to the rapid growth of the observations and the computing power.

Furthermore, the need to improve prediction capabilities towards a realistic representation of ionospheric conditions, particularly for nowcasting and forecasting applications, has led to the development of new models, which in many cases apply assimilative techniques. These techniques are considered suitable for providing a high-resolution, global picture of ionospheric response to various short-term events observed

during periods of storm activity, or the effects of gravity waves coupling the ionosphere to the lower atmosphere (Galkin et al. 2012). There are various models of this type available for different applications with a wide range of determined accuracy limits depending on the characteristics of each model.
It is also worth noting that data assimilation techniques are currently used in both empirical and physics-based models. The variety of such models includes short-term forecasting and real-time models, which are applied to areas of different sizes, corresponding to local, regional, or global models. Furthermore, the models can be developed for applications in distinct geographical sectors such as the equatorial, middle latitude, or polar regions, where different phenomena occur, giving rise to irregularities of different sizes and characteristic times.

3.1 Empirical models

One of the most established empirical model is the International Reference Ionosphere (IRI) (Bilitza et al., 2014), a joint project of the Committee on Space Research (COSPAR) and the International Union of Radio Science (URSI). Being based on most of the available and reliable observations from the ground and from space, such as from ionosonde, top-sounder, and satellites and rockets in situ measurements (Rawer et al., 1978; Bilitza, 2004), the IRI model is the de facto international standard for the climatological specification of ionospheric parameters. For given location, time and date, IRI describes the ionosphere plasma electron density (N), electron temperature, ion temperature, ion composition, and several additional parameters in the altitude range from 60 km to 2000 km, and the electron content. Moreover, the IRI Plas model, the International Reference Ionosphere extended to the Plasmasphere (Gulyaeva et al.,2002a,b), is recognized as a candidate model for an international standard for the specification for ionosphere and plasmasphere plasma densities and temperatures by the International Standardization Organization (ISO) (Gulyaeva and Bilitza, 2012), providing vertical electron density profiles ($N(h)$) for a desired date, time, and location. Since they use CCIR and URSI f_oF_2 numerical maps to constrain $N(h)$ at the F_2 region peak, IRI and IRI Plas models can be considered as three-dimensional (3D) models. Recently, a particularly promising assimilative approach has been developed for the so called IRI–RTAM (International Reference Ionosphere–Real Time Assimilative Mapping), using data from the Global Ionospheric Radio Observatory (GIRO) (Reinish and Galkin, 2011) to smoothly transform IRI's background empirical maps of ionospheric characteristics to match the observations (Galkin et al., 2012). The new technique, whose robustness to automatic scaling error has been carefully assessed, "updates" the IRI N distribution while preserving the overall integrity of IRI's ionospheric representations.
Another empirical 3D ionospheric electron density model is the NeQuick (Hochegger et al., 2000; Radicella and Leitinger, 2001), subsequently improved as NeQuick2 (Nava et al., 2008), developed at the Aeronomy and Radiopropagation Laboratory of The Abdus Salam International Centre for Theoretical Physics (ICTP), Trieste, Italy, and at the Institute for Geophysics, Astrophysics and Meteorology (IGAM) of the University of Graz, Austria. NeQuick model is based on the DGR profiler proposed by Di Giovanni and Radicella (Di Giovanni and Radicella, 1990), subsequently modified by Radicella and Zhang (1995) and continuously updated (Leitinger et al., 2005; Coïsson et al. 2006). It is a quick-run model particularly tailored for trans-ionospheric applications, allowing calculation of electron concentration at any given location in the ionosphere and thus the total electron content (TEC) along any ground-to-satellite ray-path by means of numerical integration. For this reason, it has also been adopted by the International Telecommunication Union, Radiocommunication Sector (ITU-R) as a suitable method for TEC modeling (ITU, 2003). Furthermore, NeQuick2 is able to ingest ionosonde, Global Navigation Satellite System (GNSS) and Radio Occultation (RO) data, using different data assimilation techniques (Nava et al., 2011; Brunini et al., 2011; Shaikh et al., 2017). Some types of data which can be ingested are vertical TEC maps, f_oF_2 and h_mF_2 data and experimental slant TEC at a given location. Effective parameters are used, and the internal consistency and effectiveness of the adaptation methods have been assessed, using also IRI model in some cases.
Among the 3D assimilative ionospheric models, it is worth mentioning the Electron Density Assimilative Model (EDAM) (Angling and Cannon, 2004; Angling, 2008), developed by QinetiQ, which can ingest

measured slant TEC from a network of ground-based dual-frequency GPS receivers. In particular, these measurements are used to adjust an empirical 3D climatological distribution of *N*, constraining the model results and achieving better ionospheric nowcasting. EDAM was compared to a median model called Parameterised Ionospheric Model (PIM) (Daniell et al., 1995), using independent data measured by oblique and vertical ionosondes (Angling and Khattatov,2006). Results indicated that when tested against vertical ionosondes, EDAM can reduce $RMSf_oF_2$ errors compared to PIM.

Other assimilative models describing the ionosphere over Europe include the Solar Wind driven auto regression model for Ionospheric short-term Forecast (SWIF) (Tsagouri et al., 2009), and the ISP model (Pezzopane et al., 2011). In the recent advances in the implementation and validation of the SWIF model, which is running in the European Digital Upper Atmosphere Server (DIAS) (Belehaki et al., 2005; Belehaki et al., 2006), the forecasts have shown relative improvements over climatology by about 30% in middle-to-low and high latitudes, and 40% in middle-to-high latitudes (Tsagouri and Belehaki, 2015). The ISP model provides a 3D electron density specification of the ionosphere based on a combination of autoscaled data from different reference ionospheric stations, the f_oF_2 and $M(3000)F_2$ regional grids calculated by the Simplified Ionospheric Regional Model UPdated (SIRMUP) (Zolesi et al., 2004; Tsagouri et al., 2005), and the IRI model. Overall, its representation of the ionosphere is better than the climatological picture produced by only the IRI-URSI and the IRI-CCIR models, as shown by Pezzopane et al. (2013).

To improve the climatological performance, it is worth noting that some models are driven by a geomagnetic index to account for storm-time changes in the ionosphere. For example, the STORM model (Araujo-Pradere et al., 2002; Araujo-Pradere and Fuller-Rowell, 2002), which is included in the IRI2000 (Bilitza, 2001) as a correction factor for perturbed conditions, is driven by the a_p index over the previous 33 h, and the output is used to scale the quiet time f_oF_2 to account for increases or decreases in *N* resulting from a storm. The results of the comparison of the *RMS* error with the previous version of IRI indicate that IRI2000 offers almost a 30% improvement over IRI95 during storm days and is able to identify more than 50% of the increase in variability, above quiet times, due to storms (Araujo-Pradere et al., 2003).

Finally, another model that takes into account geomagnetic activity and also ingests real-time data is the EUROMAP model (Mikhailov and Perrone, 2014), which is part of the global SIMP model under development in the Russian Federation to provide global ionospheric monitoring and forecasting. The EUROMAP is based on 3 h a_p indices, effective ionospheric *T* index, and real-time f_oF_2 observations, and provides a method for f_oF_2 short-term forecasting over Europe. The improvement over the STORM model was studied and assessed as 40% in winter, 59% in summer, and 39% during equinox.

3.2 Physics-based models

Some physics-based models worth mentioning are SAMI3 (Huba et al., 2008) and the Global Ionosphere-Thermosphere Model (GITM) (Ridley et al., 2006). SAMI3 is a 3D global ionospheric model based on the 2D model SAMI2 (Huba et al., 2000), which uses a unique, non-orthogonal, nonuniform, fixed grid. It calculates the plasma and chemical evolution of seven ion species (H^+, He^+, N^+, O^+, NO^+, N_2^+ and O_2^+) in the altitude range 85 km to 20,000 km. The ion temperature equation is solved for three ion species (H^+, He^+, and O^+) as well as the electron temperature equation, and ion inertia is included in the ion momentum equation for motion along the geomagnetic field. An offset, tilted dipole geomagnetic field is used, and the plasma is modeled from hemisphere to hemisphere. In addition, high altitude boundary conditions are not needed since a complete ionospheric flux tube is modeled.

GITM, instead, is a 3D spherical code that models the Earth's thermosphere and ionosphere system using a stretched grid in latitude and altitude, while having a fixed resolution in longitude. The number of grid points in each direction can be specified, so the resolution is extremely flexible. Allowing for non-hydrostatic solutions to develop (i.e., the full vertical momentum equation is solved), more realistic dynamics in the auroral zone can be simulated by the model. GITM explicitly solves for the neutral densities of O, O_2, $N(^2D)$, $N(^2P)$, $N(^4S)$, N_2, and NO, and ion species $O^+(^4S)$, $O^+(^2D)$, $O^+(^2P)$, O_2^+, N^+, N_2^+, and NO^+, covering all latitudes and a vertical range from about 90 km to 600 km, with a latitude resolution of 2.5º,

and longitude resolution of 5º. One major difference between GITM and other thermosphere codes is the use of an altitude grid instead of a pressure grid: the vertical grid spacing is less than 3 km in the lower thermosphere, and over 10 km in the upper thermosphere.

Among the physics-based models which use state-of-the-art data assimilation techniques there are the two models developed by the Utah State University (USU) as part of the Global Assimilation of Ionospheric Measurements (GAIM) program (Schunk et al., 2004; Schunk et al., 2005). Both models are capable of assimilating data from a variety of data sources, including in situ N from satellites, bottom-side $N(h)$ from ionosondes, TEC measurements between ground receivers and the GPS satellites, occultation data from satellite constellations, and ultraviolet emissions from the ionosphere measured by satellites.

The first model is the Gauss-Markov Data Assimilation Model, which uses a physics-based model of the ionosphere and a Kalman filter as a basis for assimilating a diverse set of real-time (or near real-time) measurements. It has both regional and global capabilities, and the output is the N 3D distribution at user-specified times. The physics-based model is the Ionosphere Forecast Model (IFM) (Schunk et al., 1997), which is global and covers the E and F regions, and topside from 90 to 1400 km. It takes account of electrons and five ion species (NO^+, O_2^+, N_2^+, O^+, H^+), electron and ion temperatures, and plasma drifts both parallel and perpendicular to the geomagnetic field.

More sophisticated, the Full-Physics Data Assimilation Model is based on a new physics-based model that is composed of an Ionosphere-Plasmasphere Model (IPM) (Shunk, 2002), which covers low and mid-latitudes, and an Ionosphere-Polar Wind Model (IPWM), which covers high latitudes. These new physics-based models cover the altitude range from 90 to 20,000 km, which includes the E and F regions, topside ionosphere, plasmasphere, and polar wind, use the International Geomagnetic Reference Field (IGRF), and include six ion species (NO^+, O_2^+, N_2^+, O^+, He^+, H^+), ion and electron temperatures, and plasma drifts parallel and perpendicular to the geomagnetic field. The different real-time data sources are assimilated via a Kalman filter technique and quality control algorithms are provided as an integral part of the model. The full-physics data assimilation model rigorously evolves the three-dimensional electron density field and its associated errors using the full-physical model. During severe space weather events, this is an advantage over the Gauss-Markov model, where the errors evolve statistically.

Another assimilative physics-based model worth to mention is the IonoNumerics model developed by Fusion Numerics, Inc. (Khattatov et al., 2004), which considers seven ion species and electrons, utilizing a set of time-dependent differential equations describing the conservation of mass, momentum, and energy, for a comprehensive description of chemical transformations and energy exchange between particles and energy inputs due to solar heating. It thus offers forecasting via time integration of the prognostic equations. As EDAM model, described in the previous section, IonoNumerics can utilize measured slant TEC from a network of ground-based dual-frequency GPS receivers to improve its nowcasting capabilities, and its behaviour was compared to those of PIM and EDAM, using independent data measured by oblique and vertical ionosondes (Angling and Khattatov, 2006). The results show that the daytime *RMS* f_oF_2 errors above the Eglin Air Force Base ionosonde are 1.2 MHz for the PIM, 0.7 MHz for EDAM, and 1.0 MHz for IonoNumerics. Thus, when tested against vertical ionosondes, both EDAM and IonoNumerics have shown an improved accuracy over a median model.

It is worth to mention here that PIM provides a climatological description of the ionosphere obtained in a different way than empirical models do. Indeed, a parameterized model is based on orthogonal function fits to data that are output of physics-based models. In this type of models, theoretical model runs are performed for various solar-geophysical conditions and parameterization is usually done in terms of solar activity, geomagnetic activity and season. Parametrized models are computationally fast, still retaining physics of theoretical models, but cannot accurately reproduce specific situations, being then suitable only for well-specified geophysical problems. In particular, PIM is built from combining model output from the Global Theoretical Ionospheric Model (GTIM), developed from the older code LOWLAT (Anderson, 1973), for low and middle latitude, with output from the TDIM model (Schunk, 1988) for high latitudes, and from the empirical model of Gallagher et al. (1988) for plasmaspheric altitudes.

Besides allowing the assimilation of data, another way to improve weather capabilities in models is using a systemic approach. This is the case of the coupled physics-based models, like the Thermosphere-

Ionosphere-Electrodynamics General Circulation Model (TIE-GCM) (Roble et al., 1988; Richmond et al., 1992), developed at the National Center for Atmospheric Research (NCAR). It is a comprehensive, first-principles, three-dimensional, non-linear representation of the coupled thermosphere and ionosphere system that includes a self-consistent solution of the low-latitude electric field. Hydrostatic equilibrium, constant gravity, steady-state ion and electron energy equations, and incompressibility on a constant pressure surface, are assumed. The model solves the three-dimensional momentum, energy and continuity equations for neutral and ion species at each time step, using a semi-implicit, fourth-order, centered finite difference scheme, on each pressure surface in a staggered vertical grid. It has 29 constant-pressure levels in the vertical, extending from approximately 97 km to 500 km in intervals of one-half scale height, and a 5° x 5° latitude-longitude grid, in its base configuration.

Following the systemic approach, the TIE-GCM is included as a self-consistent aeronomic scheme for the coupled Thermosphere/Ionosphere system in a series of numeric simulation models of the Earth's upper atmosphere, including the upper Stratosphere, Mesosphere, and Thermosphere. In particular, TIE-GCM is an extension of the Thermospheric General Circulation Model (TGCM) (Dickinson et al., 1981, 1984), which is a 3D time-dependent model of the Earth's neutral upper atmosphere. It uses a finite differencing technique to obtain a self-consistent solution for the coupled, nonlinear equations of hydrodynamics, thermodynamics, continuity of the neutral gas and for the coupling between the dynamics and the composition. Moreover, recent models in the series include, besides TIE-GCM, an extension of the lower boundary from 97 to 30 km, including the physical and chemical processes appropriate for the Mesosphere and upper Stratosphere, that is the Thermosphere Ionosphere Mesosphere Electrodynamic General Circulation Model (TIME-GCM) (Roble and Ridley, 1994).

References

[1] Galkin, I.A., Reinisch, B.W., Huang, X., Bilitza, D., 2012. Assimilation of GIRO data into a real-time IRI. Radio Sci. 47. http://dx.doi.org/ 10.1029/2011RS004952, RS0L07.

[2] Bilitza, D., Altadill, D., Zhang, Y.L., Mertens, C., Truhlik, V., Richards, P., McKinnell, L.A., Reinisch, B., 2014. The international reference ionosphere 2012-a model of international collaboration. J. Space Weather Space Clim. 4.

[3] Rawer, K., Bilitza, D., Ramakrishnan, S. Goals and Status of the International Reference Ionosphere. Rev. Geophys. Space Phys. 16, 177-181, 1978.

[4] Bilitza, D. Correction for the IRI topside electron density model based on Alouette/ISIS topside sounder data. Adv. Space Res. 33, 838-843, 2004.

[5] Gulyaeva, T.L., Huang, X., Reinisch, B., 2002a. Plasmaspheric extension of topside electron density profiles model software for ISO. Adv. Space Res. 29 (6), 825–831.

[6] Gulyaeva, T.L., Huang, X., Reinisch, B., 2002b. Ionosphere-plasmasphere model software for ISO. Acta Geod. Geophys. Hungarica 37 (2–3), 143–152.

[7] Gulyaeva, T.L., Bilitza, D., 2012. Towards ISO standard earth ionosphere and plasmasphere model. In: Larsen, R.J. (Ed.), New Developments in the Standard Model. Nova, Hauppauge, New York, pp. 1–39.

[8] Reinisch, B.W., Galkin, A. Global Ionospheric Radio Observatory (GIRO). Earth Planets Space 63, 377-381, 2011.

[9] Hochegger, G., Nava, B., Radicella, S.M., Leitinger, R., 2000. A family of ionospheric models for different uses. Phys. Chem. Earth Part C: Solar, Terr. Planet. Sci. 25 (4), 307–310.

[10] Radicella, S.M., Leitinger, R., 2001. The evolution of the DGR approach to model electron density profiles. Adv. Space Res. 27 (1), 35–40.

[11] Nava, B., Coïsson, P., Radicella, S.M., 2008. A new version of the NeQuick ionosphere electron density model. J. Atmos. Sol. Terr. Phys. 70 (15), 1856–1862. http://dx.doi.org/10.1016/j.jastp.2008.01.015.

[12] Di Giovanni, G., Radicella, S.M., 1990. An analytical model of the electron density profile in the ionosphere. Adv. Space Res. 10 (11), 27–31.

[13] Radicella, S.M., Zhang, M.L., 1995. The improved DGR analytical model of electron density height profile and total electron content in the ionosphere. Annali di Geofisica XXXVIII (1), 35–41.

[14] Leitinger, R., Zhang, M.L., Radicella, S.M., 2005. An improved bottomside for the ionospheric electron density model NeQuick. Annals of Geophysics 48 (3), 525–534.

[15] Coïsson, P., Radicella, S.M., Leitinger, R., Nava, B., 2006. Topside electron density in IRI and NeQuick: features and limitations. Adv. Space. Res. 37, 937–942.

[16] ITU. Ionospheric propagation data and prediction methods required for the design of satellite services and systems. Recommendation P. 531–7, Geneva, 2003.

[17] Nava, B., Radicella, S. M., Azpilicueta, F., 2011. Data ingestion into NeQuick 2. Radio Sci. 46. DOI: 10.1029/2010RS004635, 2011.

[18] Brunini, C., Azpilicueta, F., Gende, M., Camilion, E., Aragon-Angel, A., Hernandez-Pajares, M., Juan, M., Sanz, J., Salazar, Dagoberto, 2011. Ground- and space-based GPS data ingestion into the NeQuick model. Journal of Geodesy (12), 931-939, DOI: 10.1007/s00190-011-0452-4.

[19] Shaikh, M. M., Nava, B., Kashcheyev, A., 2017. A model-assisted radio occultation data inversion method based on data ingestion into NeQuick. Adv. Space Res. 59 (1), 326-336, DOI: 10.1016/j.asr.2016.09.006.

[20] Angling, M.J., Cannon, P.S., 2004. Assimilation of radio occultation measurements into background ionospheric models. Radio Sci. 39. http://dx.doi.org/10.1029/2002RS002819.

[21] Angling, M.J., 2008. First assimilations of COSMIC radio occultation data into the Electron Density Assimilative Model (EDAM). Ann. Geophys. 26, 353–359.

[22] Daniell Jr, R.E., Brown, L.D., Anderson, D.N., Fox, M.W., Doherty, P. H., Decker, D.T., Sojka, J.J., Schunk, R.W., 1995. Parameterized ionospheric model: a global ionospheric parameterization based on first principles models. Radio Sci. 30 (5), 1499–1510. http://dx.doi.org/ 10.1029/95RS01826.

[23] Angling, M.J., Khattatov, B., 2006. Comparative study of two assimilative models of the ionosphere. Radio Sci. 41. http://dx.doi.org/10.1029/ 2005RS003372, RS5S20.

[24] Tsagouri, I., Koutroumbas, K., Belehaki, A., 2009. Ionospheric foF2 forecast over Europe based on an autoregressive modeling technique driven by solar wind parameters. Radio Sci. 44. http://dx.doi.org/ 10.1029/2008RS004112, RS0A35.

[25] Pezzopane, M., Pietrella, M., Pignatelli, A., Zolesi, B., Cander, L.R., 2011. Assimilation of autoscaled data and regional and local ionospheric models as input sources for real-time 3-D International Reference Ionosphere modeling. Radio Sci. 46. http://dx.doi.org/10.1029/ 2011RS004697, RS5009.

[26] Belehaki, A., Cander, L., Zolesi, B., Bremer, J., Juren, C., Stanislawska, I., Dialetis, D., Hatzopoulos, M., 2005. DIAS project: the establishment of a European digital upper atmosphere server. J. Atmos. Sol.-Terr. Phy. 67 (12), 1092–1099.

[27] Belehaki, A., Cander, L., Zolesi, B., Bremer, J., Juren, C., Stanislawska, I., Dialetis, D., Hatzopoulos, M. Monitoring and Forecasting the Ionosphere Over Europe: The DIAS Project. Space Weather, 2006SW000270, 2006.

[28] Tsagouri, I., Belehaki, A., 2015. Ionospheric forecasts for the European region for space weather applications. J. Space Weather Space Clim. 5 (A9). http://dx.doi.org/10.1051/swsc/2015010.

[29] Zolesi, B., Belehaki, A., Tsagouri, I., Cander, L.R., 2004. Real-time updating of the Simplified Ionospheric Regional Model for operational applications. Radio Sci. 39. http://dx.doi.org/10.1029/2003RS002936, RS2011.

[30] Tsagouri, I., Zolesi, B., Belehaki, A., Cander, L.R., 2005. Evaluation of the performance of the real-time updated simplified ionospheric regional model for the European area. J. Atmos. Sol.-Terr. Phy. 67, 1137–1146.

[31] Pezzopane, M., Pietrella, M., Pignatelli, A., Zolesi, B., Cander, Lj.R., 2013. Testing the three-dimensional IRI-SIRMUP-P mapping of the ionosphere for disturbed periods. Adv. Space Res. 52, 1726–1736.

[32] Araujo-Pradere, E.A., Fuller-Rowell, T.J., Codrescu, M.V., 2002. STORM: an empirical storm-time ionospheric correction model 1. Model description. Radio Sci. 37, 1070. http://dx.doi.org/10.1029/2001RS002467.

[33] Araujo-Pradere, E.A., Fuller-Rowell, T.J., 2002. STORM: an empirical storm-time ionospheric correction model 2. Validation. Radio Sci. 37 (5), 1070. http://dx.doi.org/10.1029/2002RS002620.

[34] Bilitza, D., 2001. International reference ionosphere 2000. Radio Sci. 36 (2), 261–276.

[35] Araujo-Pradere, E.A., Fuller-Rowell, T.J., Bilitza, D., 2003. Validation of the STORM response in IRI2000. J. Geophys. Res. 108 (A3), 1120. http://dx.doi.org/10.1029/20032002JA009720.

[36] Mikhailov, A.V., Perrone, L., 2014. A method for foF2 short-term (1–24 h) forecast using both historical and real-time foF2 observations over European stations: EUROMAP model. Radio Sci. 49 (4), 253–270. http://dx.doi.org/10.1002/2014RS005373.

[37] Huba, J. D., Joyce, G., Krall, J., 2008. Three-dimensional equatorial spread F modeling, Geophys. Res. Lett., 35, L10102, doi:10.1029/2008GL033509.

[38] Ridley, A. J., Y. Deng, and G. Toth., 2006, The Global Ionosphere- Thermosphere Model. J. Atmos. Solar-Terrestr. Phys. 68, 839- 864.

[39] Huba, J.D., G. Joyce, and J.A. Fedder, Sami2 is Another Model of the Ionosphere (SAMI2): A new low-latitude ionosphere model, J. Geophys. Res., 105, 23,035, 2000

[40] Schunk, R.W., Scherliess, L., Sojka, J.J., Thompson, D. Global Assimilation of Ionospheric Measurements (GAIM). Radio Sci. 39, RS1S02, 2004.

[41] Schunk, R.W., Scherliess, L., Sojka, J.J., Thompson, D.C., Zhu, L. Ionospheric Weather Forecasting on the Horizon - Models of the ionosphere using state-of-the-art data assimilation techniques are nearing operational use. Space Weather 3, 2005.

[42] Schunk, R. W., J. J. Sojka, and J. V. Eccles, 1997. Expanded capabilities for the ionospheric forecast model, Rep. AFRLVS-HA-TR-98–0001, 1–142.

[43] Schunk, R. W., 2002. An ionosphere-plasmasphere model (IPM), Tech. Rep., Space Environ. Corp., Logan, Utah.

[44] Khattatov, B., Murphy, M., Gnedin, M., Cruickshank, B., Adams, J., Yudin, V., Fuller-Rowell, T., 2004. Advanced modeling of the ionosphere and upper atmosphere. Final Sci. Tech. Rep. AFRL-VSHA-TR-2004-1129, Air Force Res. Lab., Hanscom AFB, Mass.

[45] Angling, M.J., Khattatov, B., 2006. Comparative study of two assimilative models of the ionosphere. Radio Sci. 41. http://dx.doi.org/10.1029/ 2005RS003372, RS5S20.

[46] Anderson, D. N., A theoretical study of the ionospheric F-region equatorial anomaly, H, Results in the American and Asian sectors. Planet. Space. Sci., 21,421-442, 1973.

[47] Schunk, R. W., A Mathematical Model of the Middle and High Latitude Ionosphere, Pure Appl. Phys., 127, 255-303, 1988.

[48] Gallagher, D. L., P. D. Craven, R. H. Comfort (1988), An empirical model of the earth's plasmasphere, Adv. Space Res., **8**(8), 15-24.

[49] Roble, R. G., E. C. Ridley, A. D. Richmond and R. E. Dickinson, A coupled thermosphere / ionosphere general circulation model, Geophys. Res. Lett., 15, 1325-1328, 1988.

[50] Richmond, A. D.., E. C. Ridley, and R. G. Roble, A thermosphere/ionosphere general circulation model with coupled electrodynamics, Geophys. Res. Lett., 6, 601-604, 1992.

[51] Dickinson, R. E., E. C. Ridley and R. G. Roble, A three-dimensional general circulation model of the thermosphere, *J. Geophys. Res.*, **86**, 1499-1512, 1981.

[52] Dickinson, R. E., E. C. Ridley and R. G. Roble, Thermospheric general circulation with coupled dynamics and composition, *J. Atmos. Sci.*, **41**, 205-219, 1984.

[53] Roble, R. G., and E. C. Ridley, A thermosphere-ionosphere-mesosphere-electrodynamics general circulation model (TIME-GCM): equinox solar cycle minimum simulations (30-500 km), *Geophys. Res. Lett.*, **21**, 417-420, 1994.

4. The Regional Assimilative Three-dimensional Ionospheric Model (RATIM)

The main purpose of this work is the development of a regional ionospheric 3D model able to ingest vertical and oblique radio-sounding data. The Regional Assimilative Three-dimensional Ionospheric Model (RATIM) (Sabbagh et al., 2016) has been firstly developed to ingest vertical plasma frequency profiles $f_p(h)$ and tested over the Italian area. Next, RATIM has been applied to the Japanese-South Korean region, where both vertical and oblique radio-soundings are systematically performed. As we will see in Chapter 7, the RATIM data ingestion ability has been improved thanks to the introduction of a Maximum Usable Frequencies (MUFs) assimilation procedure.

RATIM has been developed starting from a bottom-side $N(h)$ profiler based on the Adaptive Ionospheric Profiler (AIP), which is the model applied by Autoscala (Scotto and Pezzopane, 2002; Pezzopane and Scotto, 2005) in the more complex process of automatic interpretation of vertical ionograms. During the development of Autoscala, AIP demonstrated sufficient adaptability to constitute a useful tool for real-time specification of $N(h)$ (Scotto, 2009), along with the application of techniques to identify the traces of vertical ionograms. RATIM has the purpose of extending this approach to the volume of the ionosphere. It is constructed based on empirical values for a set of ionospheric parameters $P_{i[base]}$ over the considered region, some of which have an assigned variation ΔP_i. As described in detail in Section 4.4, the ΔP_i values are obtained from a $f_p(h)$ assimilation procedure consisting in minimizing the root-mean-square deviation *RMSD* between the observed and modeled profiles at the locations where observations are available, where observed $f_p(h)$ are obtained from vertical radio-sounding measurements through ionograms inversion techniques. After the assimilation procedure, $P_i = P_{i[base]} + \Delta P_i$ values are used as input for the $N(h)$ profiler to characterize the actual ionosphere in the area where measurements are performed.

RATIM has been tested using data recorded by different ionosondes at a couple of ionospheric stations over Italy and then comparing the results against data from a third Italian station, assumed as a reference. As the interest has been to obtain and verify appropriate capability to adapt to any ionospheric condition, the model has been tested in quiet and disturbed conditions, and during day-time and night-time hours in different seasons, having selected two different periods for this purpose.

The software developed can produce maps of the critical frequencies f_oF_1 and f_oF_2, and of f_p at a fixed altitude, with transverse and longitudinal cross-sections of the bottom-side ionosphere in a color scale, over Italy. Modeled $f_p(h)$ and associated simulated ordinary ionogram traces can easily be produced for any geographic location within the area, and $f_p(\varphi,\lambda,h)$ values within the considered volume can also be provided.

4.1 The adaptive $N(h)$ model used

The $N(h)$ model used in this work is based on AIP, which is able to ingest 12 parameters that can vary across a wide range, describing all ionospheric conditions. The 12 parameters are processed to define anchor points and the shape of the F region. Analytic functions are then applied to appropriately connect the anchor points, determining $N(h)$ from the base of the ionosphere up to the altitude of maximum N in the F_2 region. As shown schematically in Fig. 4.1, AIP can be divided into two sections: the bottom-side of the F region (from point A to C), the E region comprising the valley, and the lower part of the E region (from point C to F).

The bottom-side of the F region is constructed based on the shape formulation of the F layer in IRI $N(h)$ by Reinisch and Huang (2000). It is fully defined by introducing three shape parameters B_0, B_1, D_1 and using the maximum electron densities of the F_1 and F_2 layers, N_mF_1 and N_mF_2, respectively, and the peak height h_mF_2. Conversely, h_mF_1 is numerically computed assuming continuity of $N(h)$ in point B.

The E region is modeled by defining the position of the following four anchor points: (a) the upper valley point (C) with electron density N_mE and height $h_mE+\delta h_vE$; (b) the valley point (D) with electron density $N_mE-\delta N_vE$ and height h_vE; (c) the point (E) with electron density N_mE and height h_mE; (d) the zero point (F) with N set to zero and height h_mE-y_mE.

Point C is joined to point D by a parabola, computed by requiring a vertical slope in D and continuity at points D and C. Point D is joined to point E by a cubical, calculated by requiring continuity and vertical gradients at points D and E. The bottom-side of the E region (from point E to point F) is modeled as a parabolic layer (Bilitza, 1998a).

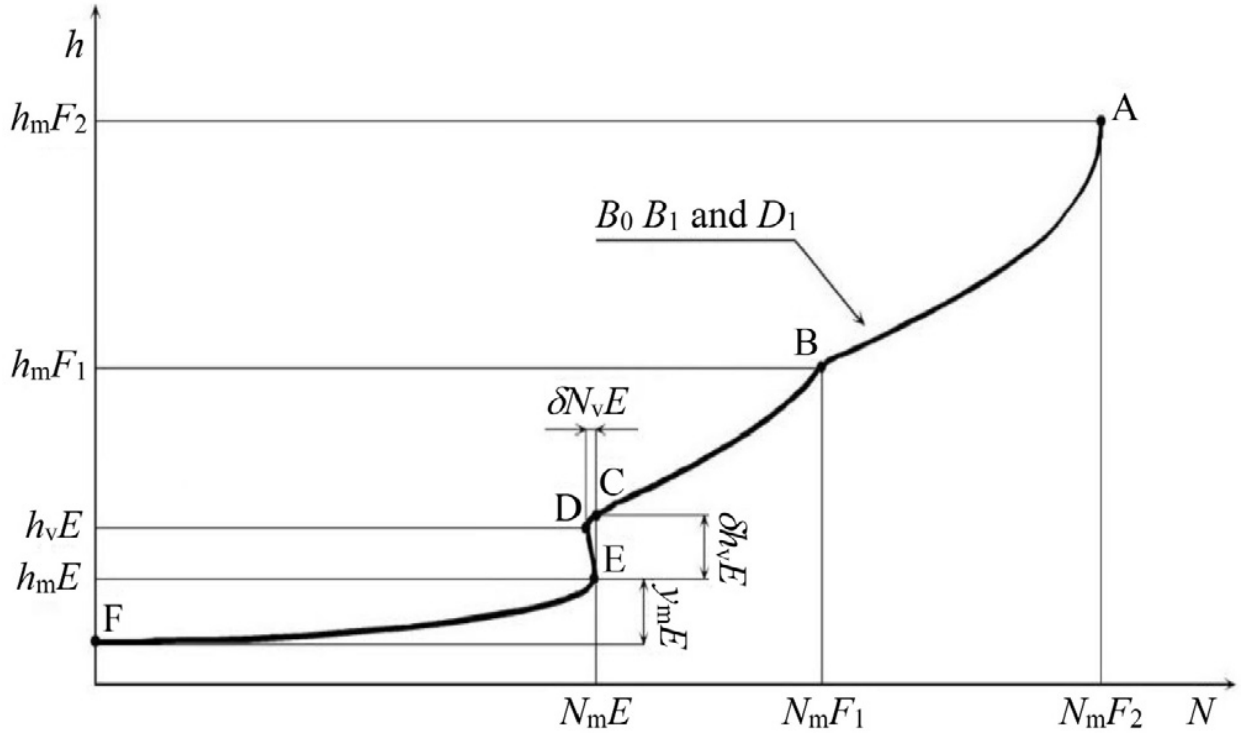

Fig. 4.1. The $N(h)$ model used in this work. It is divided into the following two regions: (1) the bottom-side F_2 profile, through the F_1 layer down to the top of the E valley (from A to C); (2) the E valley, and the E bottom-side (from C to F). (Sabbagh et al., 2016)

The detailed formulas applied to generate $N(h)$ starting from the anchor points are described in the work of Scotto (2009) and references therein. Sufficient for this work is the fact that the above-mentioned formulas for the F_2, F_1, and E regions can be utilized to construct an $N(h)$ model with the 12 free parameters (6 regarding the E region, and 6 the F_2 and F_1 layers) defined as follows.

(1) N_mF_2: maximum electron density of the F_2 layer.
(2) h_mF_2: height of maximum plasma frequency in the F_2 region.
(3) N_mF_1: maximum electron density of the F_1 layer.
(4) B_0: thickness parameter of the F_2 layer.
(5) B_1: shape parameter of the F_2 region.
(6) D_1: shape parameter of the F_1 layer.
(7) N_mE: maximum plasma frequency of the E layer.
(8) h_mE: height of maximum plasma frequency of the E layer.
(9) h_vE: height of the valley of the E region.
(10) δh_vE: width of the valley of the E region.
(11) δN_vE: depth of the valley of the E region.
(12) y_mE: semi width of the E layer, assumed parabolic.

The next section presents the empirical formulations used as input values for the $N(h)$ model parameters.

4.3 3D description of the quiet ionosphere

To provide a three-dimensional description of the ionosphere, most of the P_i (i=1, ...12) parameters described above are introduced into the $N(h)$ model with a functional dependence on time t, latitude λ, and longitude φ, in accordance with established empirical models, based on monthly median values. These P_i values are indicated with the subscript [base].

It is worth noting that the 3D model constructed in this way gives a description of a monthly median ionosphere, but is not suitable for real-time applications, as it cannot describe short-term variations. As described in the next section, the RATIM ability to adapt to actual momentary conditions is achieved by determining a variation ΔP_i of certain P_i, obtained from a $f_p(h)$ assimilation procedure.

The models for the different ionospheric parameters used as input for the AIP are here described. The maximum electron densities of the different layers are derived from the respective critical frequencies, according to the relationship (2.2).

The critical frequency of the E region is modeled with the following relationships (Scotto, 2009):

$$f_oE_{[\text{base}]} = \begin{cases} 0.9\cdot[(180+1.44\cdot R_{12})\cos\chi]^{1/4}, & \text{if } 0^\circ \leqslant \chi < 80^\circ, \quad (4.1a) \\ a_{\text{trans}}(R_{12}) + b_{\text{trans}}(R_{12})\cdot\chi, & \text{if } 80^\circ \leqslant \chi < \chi_{\text{crit}}, \quad (4.1b) \\ a_{\text{night}}(R_{12}) + b_{\text{night}}(R_{12})\cdot\chi, & \text{if } \chi_{\text{crit}} \leqslant \chi \leqslant 180^\circ, \quad (4.1c) \end{cases}$$

where R_{12} is the twelve-month smoothed sunspot number, and χ_{crit} is the solar zenith angle χ associated with solar terminator at the altitude of the E layer h_mE, set to 110 km under all conditions. The precision of this setting is sufficient in this context, although available data shows a dependence of this height on latitude, season, time and solar activity (Bilitza, 1998b).

The expression (4.1a) for f_oE (χ, R_{12}) used for $\chi < 80^o$ is from Davies (1990), while the coefficients a_{trans}, b_{trans}, a_{night} and b_{night} are calculated through the following relations:

$$a_{\text{trans}} = 1.727520\cdot(180 + 1.44\cdot R_{12})^{0.25}, \quad (4.2a)$$
$$b_{\text{trans}} = -0.0143245\cdot(180 + 1.44\cdot R_{12})^{0.25}, \quad (4.2b)$$

and:

$$a_{\text{night}} = f_oE_{\text{crit}} - [(f_oE_{\text{crit}} - f_oE_{\text{midnight}})/(\chi_{\text{crit}} - \chi_{\text{midnight}})]\cdot\chi_{\text{crit}}, \quad (4.3a)$$
$$b_{\text{night}} = (f_oE_{\text{crit}} - f_oE_{\text{midnight}})/(\chi_{\text{crit}} - \chi_{\text{midnight}}). \quad (4.3b)$$

It is also assumed that:

$$f_oE_{\text{midnight}} = [0.51 - 0.08\cdot\sin(1.6\cdot\varphi)]\cdot[1 + 0.06\cdot\sin(D_y/58)], \quad (4.4a)$$
$$f_oE_{\text{crit}} = a_{\text{trans}} + b_{\text{trans}}\cdot\chi_{\text{crit}}, \quad (4.4b)$$

where D_y is the calendar day, and the expression (4.4a) for f_oE_{midnight}, is due to Titheridge (2000).

The parameters h_vE and δh_vE, and $D_{\%}$ are provided by models from incoherent scatter radar measurements (Mahajan et al., 1997), where $D_{\%}$ is the ratio between δN_vE and N_mE. These models provide the following relationships:

$$h_vE_{[\text{base}]} = \begin{cases} 115.8 + 0.02\cdot\chi + 0.00078\cdot\chi^2, & \text{if } 0^\circ \leqslant \chi \leqslant 85^\circ, \quad (4.5a) \\ 130.73 - 0.069172\cdot\theta + 0.1429\cdot\theta^2, & \text{if } 85^\circ < \chi \leqslant 180^\circ, \quad (4.5b) \end{cases}$$

$$\delta h_vE_{[\text{base}]} = \begin{cases} 7.12 - 0.031\cdot\chi + 0.0023\cdot\chi^2, & \text{if } 0^\circ \leqslant \chi \leqslant 85^\circ, \quad (4.6a) \\ -329.4 + 6.04926\cdot\theta - 0.025269\cdot\theta^2 + 0.03005\cdot10^{-3}\cdot\theta^3, & \text{if } 85^\circ < \chi \leqslant 180^\circ, \quad (4.6b) \end{cases}$$

and:

$$D_{\%[\text{base}]} = \begin{cases} 0.96 - 0.00069 \cdot \chi + 0.000034 \cdot \chi^2 - 0.0000006 \cdot \chi^3, & \text{if } 0^\circ \leqslant \chi \leqslant 85^\circ, \quad (4.7a) \\ 8.98814 - 0.198225 \cdot \theta + 0.001597 \cdot \theta^2 & \\ -0.00552 \cdot 10^{-3} \cdot \theta^3 + 0.69537 \cdot 10^{-8} \cdot \theta^4, & \text{if } 85^\circ < \chi \leqslant 180^\circ, \quad (4.7b) \end{cases}$$

when $\theta = \chi$ before midnight and $\theta = 360^\circ - \chi$ after midnight. It follows that for E valley depth: $\delta N_v E_{[\text{base}]} = D_{\%[\text{base}]} \cdot N_m E_{[\text{base}]}$.
The F region is modeled using the parameters $f_oF_{2[\text{base}]}$, $h_mF_{2[\text{base}]}$, $f_oF_{1[\text{base}]}$, $B_{0[\text{base}]}$, $B_{1[\text{base}]}$, and $D_{1[\text{base}]}$. The monthly median values for the critical frequency f_oF_2 are mapped on the Earth's surface according to the summation (Jones and Gallet, 1962; Jones et al., 1969):

$$f_oF_{2[\text{base}]}(\varphi, \lambda, T) = \sum_{k=0}^{75} D_k(T) \cdot G_k(\varphi, \lambda), \quad (4.8)$$

$$D_k(T) = a_0^{(k)} + \sum_{j=1}^{6} [a_j^{(k)} \cos(jT) + b_j^{(k)} \sin(jT)], \quad (4.9)$$

where T = 15·UT–180º, and UT is the decimal Universal Time. The coefficients $a_j^{(k)}$ and $b_j^{(k)}$ are supplied with the IRI model, for periods of high and low solar activity (Bilitza, 1986; Rawer and Bilitza, 1989). The level of solar activity on the relevant day, expressed through R_{12}, is thus used by the model to interpolate coefficients and obtain f_oF_2 values attributable to the ionosphere all over the Earth, according to (4.8) and (4.9). The $G_k(\varphi,\lambda)$ functions also depend on Rawer's modified magnetic inclination x (Rawer, 1963):

$$x = \arctan \frac{I}{\sqrt{\cos \varphi}}, \quad (4.10)$$

where I is the magnetic inclination. This dependence is introduced to take account of the Earth's Magnetic Field (EMF) influence.
The h_mF_2 values are estimated using the formula of Bradley and Dudeney (1973):

$$h_mF_{2[\text{base}]} = \frac{1490}{M(3000)F_2 + \Delta M} - 176, \quad (4.11)$$

when $M(3000)F_2$ is the radio propagation factor, which indicates the ratio of the Maximum Usable Frequency for radio communication at a distance of 3000 km, called MUF(3000)F_2, and f_oF_2, and:

$$\Delta M = \frac{0.18}{f_oF_{2[\text{base}]}/f_oE_{[\text{base}]} - 1.4}. \quad (4.12)$$

The monthly median values for $M(3000)F_2$ are mapped on the Earth's surface by a numerical mapping procedure similar to (5) and (6) (Jones and Gallet, 1962; Jones et al., 1969).
The critical frequency f_oF_1 is calculated according to the DuCharme et al. (1971, 1973):

$$f_oF_{1[\text{base}]} = f_s \cdot (\cos\chi)^\eta, \qquad \text{for } 0^\circ \leq \chi \leq \chi_m. \quad (4.13)$$

In this relationship:

$$\eta = 0.093 + 0.0046 \cdot \lambda_m - 0.000054 \cdot \lambda_m^2 + 0.0003 \cdot R_{12}, \quad (4.14a)$$
$$f_s = f_0 + [(f_{100} - f_0) \cdot (R_{12}/100)], \quad (4.14b)$$

where:

$$f_0 = 4.350 + 0.0058 \cdot \lambda_m - 0.000120 \cdot \lambda_m^2, \quad (4.15a)$$
$$f_{100} = 5.348 + 0.0110 \cdot \lambda_m - 0.000230 \cdot \lambda_m^2, \quad (4.15b)$$

and λ_m is the geomagnetic latitude. The maximum solar zenithal angle χ_m for which F_1 layer is expected is:

$$\chi_m = \chi_0 + [(\chi_{100} - \chi_0) \cdot (R_{12}/100)], \quad (4.16)$$

where:

$$\chi_0 = 0.87 + 0.0061 \cdot \lambda_m, \quad (4.17a)$$
$$\chi_{100} = 0.68 + 0.0089 \cdot \lambda_m, \quad (4.17b)$$

and all the angles are expressed in centesimal degrees.
As regards the shape parameter B_0, which corresponds to the altitude for which $N=N_mF_2/e$:

$$B_{0[\text{base}]} = h_mF_{2[\text{base}]} - h_{[N=N\text{mF2}/e]}, \quad (4.18)$$

as if the F_1 layer was absent (Scotto, 2009). Assuming $B_{0[\text{base}]}$ as if the F_1 layer was absent allows smooth transition between the conditions of presence/absence of the F_1 layer. In (4.18), the parameter $h_{[N=N\text{mF2}/e]}$ can be obtained knowing the E and F_2 regions characteristics:

$$h_{[N=N_mF_2/e]} = h_mE_{[\text{base}]} + \delta h_vE_{[\text{base}]} + \frac{h_mF_{2[\text{base}]} - h_mE_{[\text{base}]} - \delta h_vE_{[\text{base}]}}{N_mF_{2[\text{base}]} - N_mE_{[\text{base}]}} \cdot \left(\frac{N_mF_{2[\text{base}]}}{e} - N_mE_{[\text{base}]} \right). \quad (4.19)$$

For the shape parameter B_1, various numerical experiments have shown that it is sufficient to assume B_1 = 3 (Scotto, 2009). For parameter D_1, related to the shape of the flex in $N(h)$ corresponding to the layer F_1 (Reinisch and Huang, 2000), the following formulation has been used: $D_1 = 1.56 \cdot 10^{-3} \cdot (\chi - \chi_m)^2$ if $\chi < \chi_m$ and otherwise $D_1=10^{-4}$. This is similar to the values used by Scotto (2009). Here a dependence on solar zenith angle was introduced to allow smooth transition between the conditions of presence/absence of the F_1 layer.
As seen above, most of the parameters suitable for modeling the quiet ionosphere are related to the solar activity through R_{12}. Besides, they are all in principle functions of φ and λ, often through the functional dependence on χ. In practice, some parameters are actually dependent on φ and λ, while others are assumed to be constant over the region considered in all conditions. In summary: $f_oF_{2[\text{base}]} = f_oF_{2[\text{base}]}(\varphi,\lambda)$, $h_mF_{2[\text{base}]} = h_mF_{2[\text{base}]}(\varphi,\lambda)$, $f_oF_{1[\text{base}]} = f_oF_{1[\text{base}]}(\varphi,\lambda)$, $B_{0[\text{base}]} = B_{0[\text{base}]}(\varphi,\lambda)$, $B_{1[\text{base}]} = 3$, $D_{1[\text{base}]} = D_{1[\text{base}]}(\varphi,\lambda)$, $f_oE_{[\text{base}]} = f_oE_{[\text{base}]}(\varphi,\lambda)$, $h_mE_{[\text{base}]} = 110$ km, $h_vE_{[\text{base}]} = h_vE_{[\text{base}]}(\varphi,\lambda)$, $\delta h_vE_{[\text{base}]} = \delta h_vE_{[\text{base}]}(\varphi,\lambda)$, $\delta N_vE_{[\text{base}]} = \delta N_vE_{[\text{base}]}(\varphi,\lambda)$, $y_mE_{[\text{base}]} = 15$ km.

4.4 3D description of the real-time ionosphere

As already mentioned, the 3D model for the real-time ionosphere is constructed by allowing variations in some of the input parameters of the $N(h)$ model seen in Section 4.1:

$f_oF_2(\varphi,\lambda) = f_oF_{2[base]}(\varphi,\lambda) + \Delta f_oF_2$, (4.20)
$h_mF_2(\varphi,\lambda) = h_mF_{2[base]}(\varphi,\lambda) + \Delta h_mF_2$, (4.21)
$f_oF_1(\varphi,\lambda) = f_oF_{1[base]}(\varphi,\lambda)$, (4.22)
$B_0(\varphi,\lambda) = B_{0[base]}(\varphi,\lambda)$, (4.23)
$B_1 = B_{1[base]}$, (4.24)
$D_1(\varphi,\lambda) = D_{1[base]}(\varphi,\lambda)$, (4.25)
$f_oE(\varphi,\lambda) = f_oE_{[base]}(\varphi,\lambda)$, (4.26)
$h_mE = h_mE_{[base]}$, (4.27)
$h_vE(\varphi,\lambda) = h_vE_{[base]}(\varphi,\lambda)$, (4.28)
$\delta h_vE(\varphi,\lambda) = \delta h_vE_{[base]}(\varphi,\lambda) + \Delta\delta h_vE$, (4.29)
$\delta N_vE(\varphi,\lambda) = \delta N_vE_{[base]}(\varphi,\lambda)$, (4.30)
$y_mE = y_mE_{[base]}$. (4.31)

Thus, the 3D model can be modified by adapting the values of f_oF_2, h_mF_2, and δh_vE, applying proper variations Δf_oF_2, Δh_mF_2, and $\Delta\delta h_vE$, according to (4.20), (4.21), and (4.29). It is noteworthy that also the value of B_0 is influenced by the variations applied to f_oF_2, h_mF_2, and δh_vE, as their varied values are used in the relations (4.18) and (4.19). Furthermore, when a $f_p(h)$ profile is modeled, the value of B_0 is varied by growing around $B_{0[base]}$ until the algorithm is able to link the profile consistently with the Reinisch and Huang formulation (Reinisch and Huang, 2000). The choice to vary f_oF_2, h_mF_2, δh_vE, and B_0 arises from the experience gained during the development of AIP, in which the reliability of $f_p(h)$ is assessed by comparing the restored and recorded ionogram traces (Scotto, 2009). It was found that in most of cases varying these quantities made it possible to obtain a good fit between such traces. Besides, thanks to the regional character of RATIM, it has been sufficient to assume Δf_oF_2, Δh_mF_2, and $\Delta\delta h_vE$ as independent of φ and λ, in line with the need to reduce computation time.

It is noteworthy that f_oF_1 critical frequencies are model by RATIM according to the DuCharme et al. formulation (4.13)-(4.17), which provides monthly median values. However, it has been demonstrated that electron density at F_1 altitudes can significantly deviate from median expected behaviour, particularly when ionospheric disturbances are ongoing (Buresova, 2005; Kushnarenko et al., 2010; Gordienko et al., 2011). In a preliminary study, marginally related to this work, discrepancies in f_oF_1 values have been verified at high Southern latitudes, from the analysis of ionograms data set recorded over Antarctica in different helio-geophysical conditions. The results highlight that DuCharme et al. formulation provides a general underestimation of f_oF_1 values, particularly during high solar activity and the occurrence of geomagnetic storms, with deviations of the order of 1 MHz.

To adapt the model to actual conditions, Δf_oF_2, Δh_mF_2, and $\Delta\delta h_vE$ are adjusted to minimize the values of the *RMSD*s between the $f_p(h)$ profiles provided by the model and those obtained from the measurement at the chosen stations simultaneously. In the $f_p(h)$ assimilation procedure, f_oF_2 and h_mF_2 are also ingested from the profiles, to be compared to the corresponding values obtained by (4.20) and (4.21). Different values of Δf_oF_2, Δh_mF_2, and $\Delta\delta h_vE$ chosen within proper ranges are then tried iteratively, and those not consistent with F_2 peak parameters measurements are automatically discarded, before comparing the profiles. The total *RMSD*s to be minimized between profiles are computed for each set of realistic Δf_oF_2, Δh_mF_2, and $\Delta\delta h_vE$ values, considering the points where there are f_p values available for both profiles of a couple. Referring to this formula:

$$RMSD = \sqrt{\frac{\sum_{i=1}^{N_{tot}} \left(f^{[i]}_{p[ionos]} - f^{[i]}_{p[model]}\right)^2}{N_{tot}}}, \quad (4.32)$$

$f^{[i]}_{p[ionos]}$ and $f^{[i]}_{p[model]}$ correspond to the i^{ths} f_p values of a couple of profiles respectively observed and modeled at the same instant and location, where the i index corresponds to a specific value of common

altitude. N_{tot} is the total number of couples of values ($f_p^{[i]}{}_{[ionos]}$; $f_p^{[i]}{}_{[model]}$) considering all the stations chosen for the adapting.
Once the parameters are fixed by this procedure, the corresponding variations are applied to the related quantities over the whole geographical region. Such adapting procedure is considered successful only if the minimized *RMSD* is smaller than 1 MHz.
It is worth noting that different inversion methods to obtain the $f_p(h)$ from an ionogram are known. In particular, they differ in the modeling of the ionospheric E region because of the lack of measurements available inside the E valley. Thus, using data from different systems affects the model's performance in terms of output $f_p(h)$ shape. As we will see in the next section, in the RATIM test phase different systems have been used to assess the model's adaptability to such data.
RATIM works with different modules according to the set epoch, as reported below together with the corresponding products provided as outputs.
(1) "ADAPT", in which the adjusting procedure is performed as described above. While f_oF_2 and h_mF_2 are varied within fixed ranges in all conditions, the variation of δh_vE is assumed to be different during day and night.
(2) "TEST", in which the *RMSD* is computed between the profiles provided by the model and those observed at a test station.
(3) "MAPS", in which f_p maps are produced, both as text files and color scale images. This mode has the following sub-modes:

(3a) "foF1", giving as output a map of f_oF_1 in the region defined by the adapting stations.
(3b) "foF2", giving as output a map of f_oF_2 in the region defined by the adapting stations.
(3c) "eldens_h", giving as output a map of f_p at fixed h in the region defined by the adapting stations.
(3d) "eldens_lati", giving as output a cross-sectional map at fixed λ for φ in a proper range in the region defined by the adapting stations and for h from 60 km to h_mF_2 over each considered location.
(3e) "eldens_longi", giving as output a cross-sectional map at fixed φ for λ in a proper range in the region defined by the adapting stations and for h from 60 km to h_mF_2 over each considered location.

(4) "PROFILES", in which $f_p(h)$ are produced, both as text files and graphs.
(5) "IONOGRAMS", in which $f_p(h)$ are produced both as text files and graphs, with the associated simulated ordinary ionogram traces.
(6) "POINTS", in which f_p is provided for particular φ, λ, and h. This mode is suitable for possible future HF ray-tracing applications.
(7) "MATRIX", in which $f_p(\varphi,\lambda,h)$ values are produced as text files in the volume defined by the adapting stations and for h from 60 km to 350 km.

Once the values of Δf_oF_2, Δh_mF_2, and $\Delta\delta h_vE$ are set by the $f_p(h)$ assimilation procedure, the RATIM output products just mentioned are not actually obtained simply using the thus obtained values for the parameters (4.20)-(4.31) as input to the $N(h)$ model described in Section 4.1 all over the considered region. Indeed, each output f_p value is set equal to the mean value among f_p obtained in this way in the selected position and in the 8 adjacent points belonging to a horizontal grid with mesh length equal to 0.25° in φ and λ. The effect of this averaging is obtaining more continuity of all the ionospheric characteristics along the surfaces of equal altitude. As a result, the contour lines drawn in the maps of f_oF_1, f_oF_2 and f_p at fixed h turn out to be smoother than lines drawn in maps where the averaging is not performed.
It is worth noting that the presence of the F_1 layer is an intrinsically discontinuous property, as the F_1 region only forms during day. To handle this situation, the F_1 layer is considered actually present if it is modeled in at least 5 profiles over the 9 the average is performed among. In this case, f_oF_1 value is set equal to the mean value of the f_oF_1 modeled in those profiles.
As an example, some products are reported for the day of March 27, 2015 in Figs. 4.2(a)–(b), 4.3(a)–(c), 4.4, and 4.5 at 12:45 UT and in Fig. 4.6(a)–(b) at 12:45 UT and 22:00 UT, using the data from the Rome (41.8°N, 12.5°E, Italy) and Gibilmanna (37.9°N, 14.0°E, Italy) ionospheric stations as input.

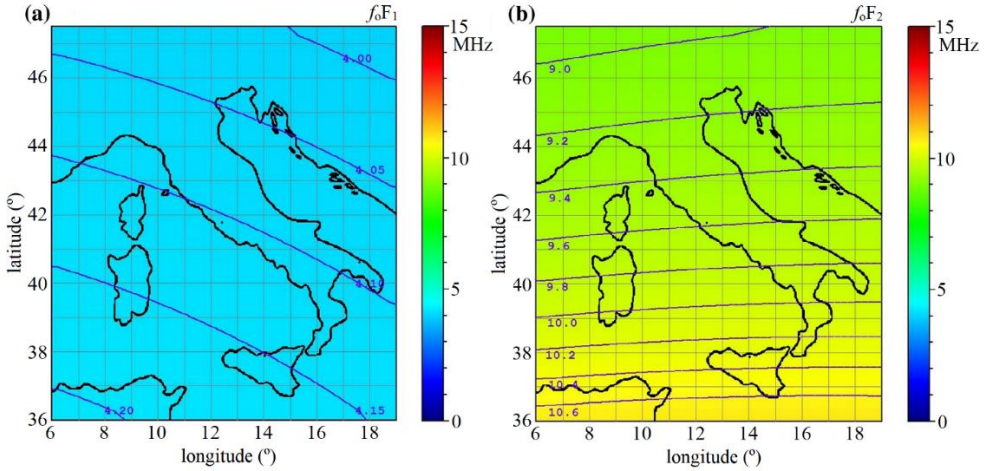

Fig. 4.2. Maps of $f_oF_1(\varphi,\lambda)$ (a) and $f_oF_2(\varphi,\lambda)$ (b) calculated for March 27, 2015 at 12:45 UT, on the basis of the $f_p(h)$ obtained from the ionogram of the DPS-4 ionosonde in Rome (41.8ºN, 12.5ºE), interpreted by ARTIST, and the $f_p(h)$ obtained from the ionogram of the AIS-INGV ionosonde in Gibilmanna (37.9ºN, 14.0ºE), interpreted by Autoscala. (Sabbagh et al., 2016)

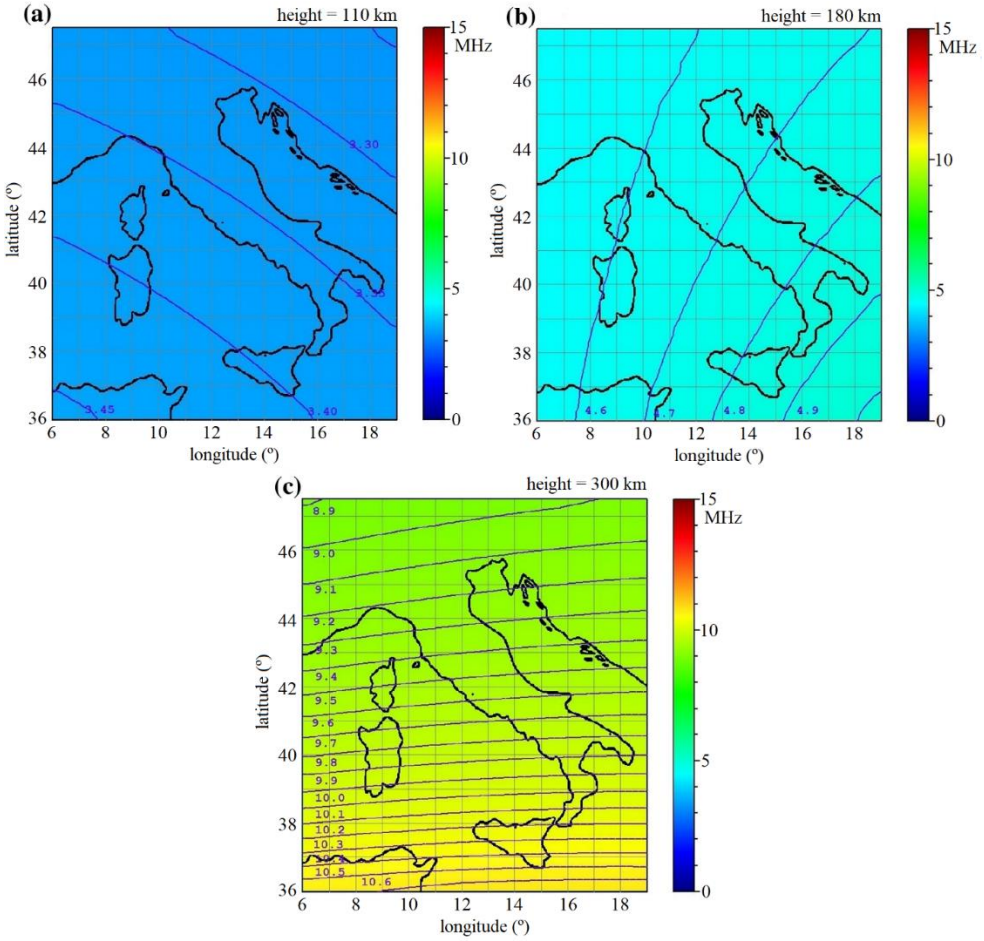

Fig. 4.3. Maps of $f_p(\varphi,\lambda)$ for h=110 km (a), h=180 km (b), and h=300 km (c), calculated for March 27, 2015 at 12:45 UT, on the basis of the $f_p(h)$ obtained from the ionogram of the DPS-4 ionosonde in Rome (41.8ºN, 12.5ºE), interpreted by ARTIST, and the $f_p(h)$ obtained from the ionogram of the AIS-INGV ionosonde in Gibilmanna (37.9ºN, 14.0ºE), interpreted by Autoscala. (Sabbagh et al., 2016)

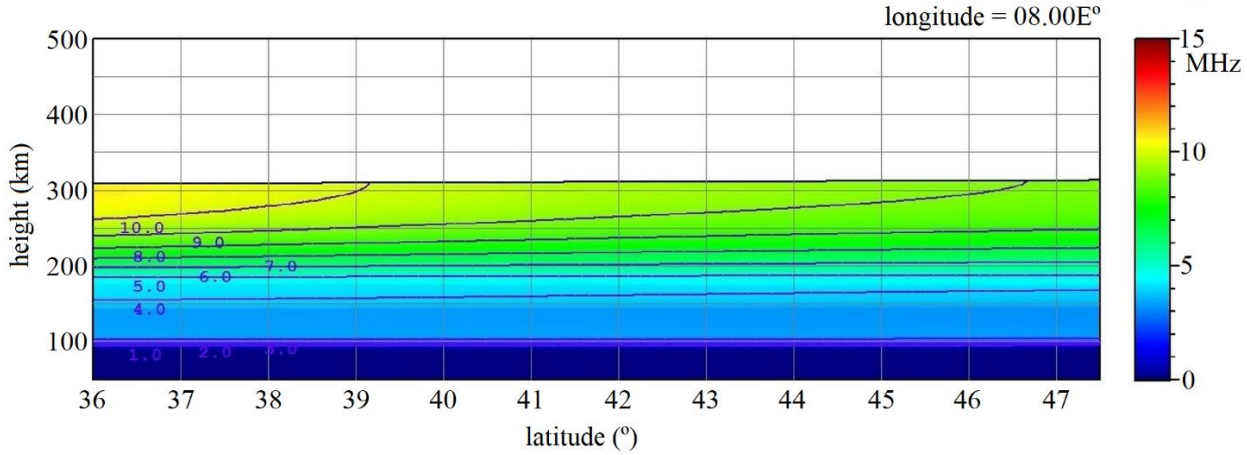

Fig. 4.4. Map of $f_p(h,\lambda)$ for φ=8.0°, calculated for March 27, 2015 at 12:45 UT, on the basis of the $f_p(h)$ obtained from the ionogram of the DPS-4 ionosonde in Rome (41.8°N, 12.5°E), interpreted by ARTIST, and the $f_p(h)$ obtained from the ionogram of the AIS-INGV ionosonde in Gibilmanna (37.9°N, 14.0°E), interpreted by Autoscala. (Sabbagh et al., 2016)

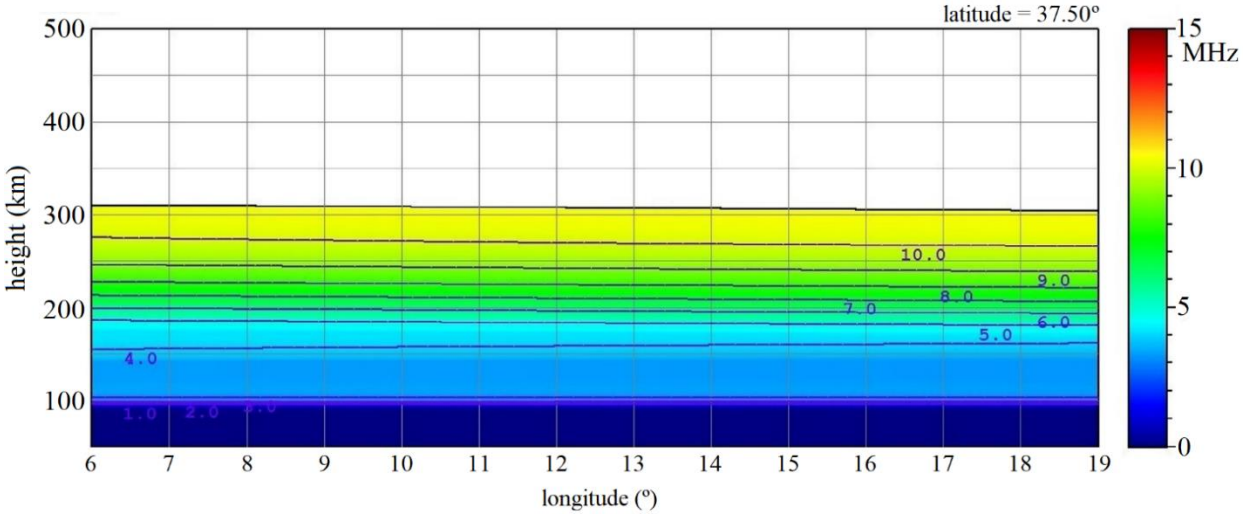

Fig. 4.5. Map of $f_p(h, \varphi)$ for λ=37.5°, calculated for March 27, 2015 at 12:45 UT, on the basis of the $f_p(h)$ obtained from the ionogram of the DPS-4 ionosonde in Rome (41.8°N, 12.5°E), interpreted by ARTIST, and the $f_p(h)$ obtained from the ionogram of the AIS-INGV ionosonde in Gibilmanna (37.9°N, 14.0°E), interpreted by Autoscala. (Sabbagh et al., 2016)

As can be inferred from the contour lines shown in Figs. 4.3(a)–(c), f_p at fixed altitude always increases southward, as expected in the northern hemisphere because of the solar irradiation enhancement approaching the equator. Moreover, the comparison of Fig. 4.3(a), Fig. 4.3(b), Fig. 4.3(c) gives an idea of the f_p trend over this area at different altitudes at the specific set epoch. In particular, in Fig. 4.3(a) it can be recognized that f_p contour lines at h_mE altitude follow the expected χ trend in the afternoon sector, as it increases westward. Instead, the f_p contour lines shown in Fig. 4.3(c) clearly follow a different pattern, and a much higher f_p horizontal gradient is observed. This arises because of the F_2 region does not suffer a strong solar control, being more sensitive to neutral winds dynamic and transport phenomena. Finally, the f_p contour lines pattern shown in Fig. 4.3(b) can be considered as an intermediate condition that arises from the continuity constraints between contiguous layers.

The coherence of the RATIM different products can be seen for instance comparing Fig. 4.4(c) and Fig. 4.5, as the f_p value model at h=300 km, φ=8º and λ=39º, that is 10.0 MHz, can be easily deduced from both maps following the relative contour line.

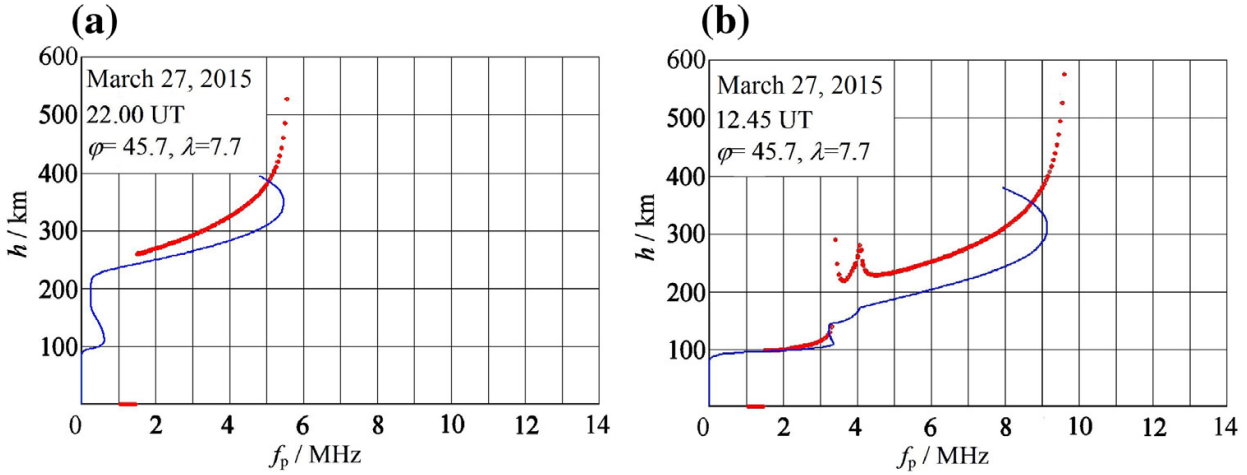

Fig. 4.6. $f_p(h)$ profiles (in blue) and the corresponding retrieved ionograms (in red) over the location with coordinates φ=45.7º and λ=7.7º, calculated for March 27, 2015 at 22:00 UT (a) and 12:45 UT (b), on the basis of the $f_p(h)$ obtained from the ionograms of the DPS-4 ionosonde in Rome (41.8ºN, 12.5ºE), interpreted by ARTIST, and the $f_p(h)$ obtained from the ionograms of the AIS-INGV ionosonde in Gibilmanna (37.9ºN, 14.0ºE), interpreted by Autoscala. (Sabbagh et al., 2016)

4.5 Model validation over Italy

RATIM performance has been tested over Italy using hourly data from the ionospheric stations of Rome (41.8ºN, 12.5ºE, Italy) and Gibilmanna (37.9ºN, 14.0ºE, Italy) for adapting, and independent data at San Vito dei Normanni (40.6ºN, 18.0ºE, Italy) for testing. In particular, the $f_p(h)$ over Rome and San Vito have been obtained from the ionograms of the DPS-4 ionosonde, known as digisonde (Haines, 1994), interpreted by the ARTIST software (Reinisch and Huang, 1983), while the $f_p(h)$ over Gibilmanna have been obtained from ionograms of the AIS-INGV ionosonde (Zuccheretti et al., 2003) interpreted by Autoscala.
The periods considered to test the model have been from June 26, 2013 to July 4, 2013 (period A), and from February 13, 2014 to February 20, 2014 (period B), including both geomagnetically quiet and disturbed days. The geomagnetic disturbance level has been assessed based on values on the planetary geomagnetic index K_p, which is computed every three hours. As highlighted in Fig. 4.7(a),(c), the days considered geomagnetically quiet (K_p < 2 throughout day) are June 26, July 2, July 3, and July 4 for period A, and February 13 and February 14 for period B, while the days considered geomagnetically disturbed (at least a $K_p \geq 2$ value during the day) are June 27, June 28, June 29, June 30, and July 1 for period A, and February 15, February 16, February 17, February 18, February 19, and February 20 for period B. The two most disturbed days in period A were affected by a moderate geomagnetic storm (K_p = 6) which began on June 28 when the Earth passed through a region of southerly aligned magnetism in the solar wind, which was subsiding during June 29, while the two most disturbed days in period B were affected by a moderate geomagnetic storm arising from the impacts of two CMEs with the Earth's magnetic field on February 19 and February 20 (http://spaceweather.com).
Since ionospheric response to storm depends on several factors (e.g., season and local time), the variation in the K_p index does not necessarily reflect the level of ionospheric activity (Araujo-Pradere and Fuller-Rowell, 2002; Araujo-Pradere et al., 2002, 2003; Mikhailov and Perrone, 2014), the latter was also determined through an examination of the ionospheric *AI* index. The *AI* index is derived by comparison of

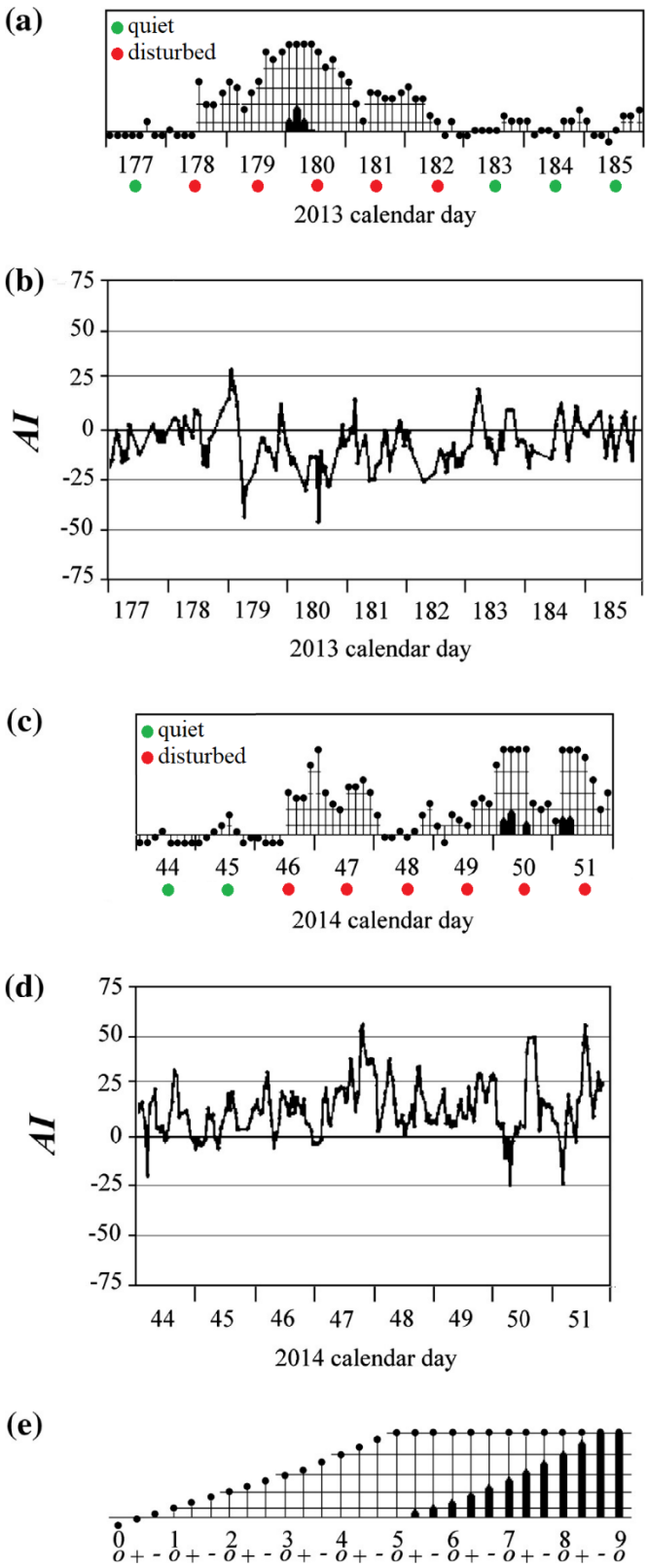

Fig. 4.7. Bartel's musical diagrams and *AI* index plots over Rome during test periods A, from June 26, 2013 to July 4, 2013 (a)-(b), and B, from February 13, 2014 to February 20, 2014 (c)-(d). Bartel's musical diagram key (e) is also reported. (Sabbagh et al., 2016)

the current f_oF_2 value with an undisturbed reference value f_oF_{2ref} (Bremer et al., 2006; Mielich and Bremer, 2010) and it is currently used to evaluate ionospheric activity levels in the DIAS service over several European ionospheric stations. f_oF_{2ref} is the median value for the time of day under consideration over the previous 30 days (Belehaki et al., 2007). Each *AI* index hourly value is considered low if its absolute value is lower than 25, disturbed if between 25 and 50, and extremely disturbed if higher than 50. It is worth noting that if a day was considered quiet when the *AI* index value is low, the daily classification of test periods A and B based on ionospheric activity levels over Rome would be in good agreement with those based on geomagnetic activity levels. The Bartel's musical diagrams from the WDC-Kyoto website (http://wdc.kugi.kyoto-u.ac.jp) and the *AI* index plots from the DIAS website (http://dias.space.noa.gr) during test periods A and B are reported in Fig. 4.7(a)–(e). These *AI* values are computed over Rome, which is the only ionospheric station in the Italian area available for the DIAS service.

The Interplanetary Magnetic Field (IMF) |**B**|, its component B_z in the Geocentric Solar Magnetospheric (GSM) coordinate system, and the solar wind speed v_{SW} recorded on board the satellite Advanced Composition Explorer (ACE) (http://www.srl.caltech.edu/ACE/) are used to characterize the solar wind conditions. Fig. 4.8(a)–(b) shows the variations of |**B**| and $-B_z$ during June 28, 2013 and June 29, 2013, and v_{SW} during February 19, 2014 and February 20, 2014. As shown in the top panel, from June 28, 2013 at about 21:00 UT to June 29, 2013 at about 09:00 UT, the IMF had an almost exclusively southward vertical component, facilitating magnetic reconnection with the Earth's magnetic field and triggering the observed geomagnetic storm. The bottom panel shows a v_{SW} increasing when the two CMEs hit the Earth's magnetic field on February 19, 2014 at about 02:00 UT and on February 20, 2014 at about 02:00 UT (Durgonics et al., 2017). The incoming CMEs were minor, but their combined impacts had a significant effect, as shown by the more relevant v_{SW} increasing (from about 500 km/s to almost 700 km/s) at the time of the second shock.

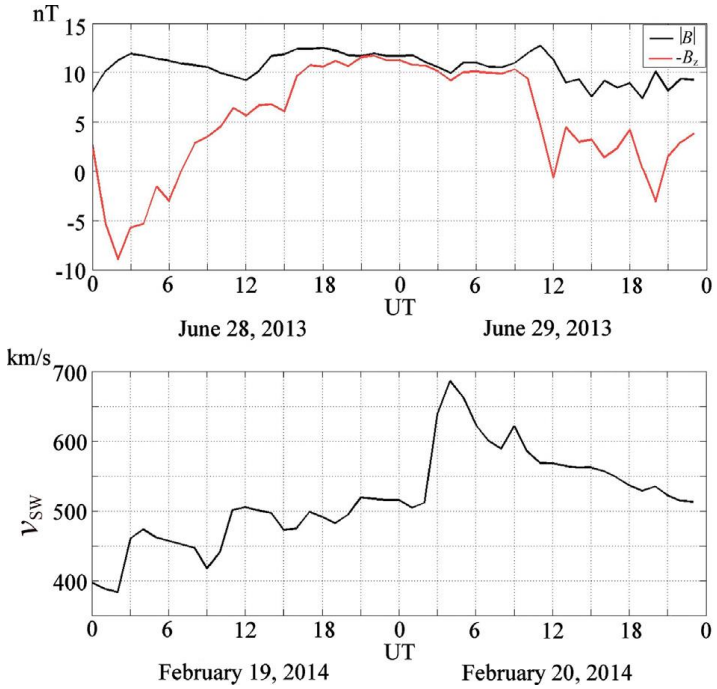

Fig. 4.8. Variations of the interplanetary magnetic field (IMF) |**B**| and its component $-B_z$ in the Geocentric Solar Magnetospheric (GSM) coordinate system during June 28, 2013 and June 29, 2013 (a), and solar wind speed v_{SW} during February 19, 2014 and February 20, 2014 (b), recorded on board the satellite Advanced Composition Explorer (ACE). (Sabbagh et al., 2016)

Fig. 4.9(a)–(b) and Table 4.1 report the results of the test performed in period A, while Fig. 4.10 (a)–(b) and Table 4.2 report the results of the test performed in period B. In particular, the figures show the average

day-time and night-time $f_p(h)$ *RMSD* graphs for Rome and Gibilmanna ($RMSD_{[R\text{-}G]}$) for each day considered. These graphs make it possible to assess the adaptability of the model to the input data, both under day-time and night-time conditions, and under different geomagnetic conditions. Likewise, Tables 4.1 and 4.2 present the percentages of success of the adjustment procedure, referred to each data class separately and for all available data. Figs. 4.9(a)–(b) and 4.10(a)–(b), also show the $RMSD_{[SV]}$ values, which is the *RMSD* for San Vito, where measurements are available. $RMSD_{[SV]}$ measures the difference between the $f_p(h)$ values predicted by the model and the corresponding values actually observed, which is indicative of the accuracy of the algorithm for modeling f_p over the geographical area considered.

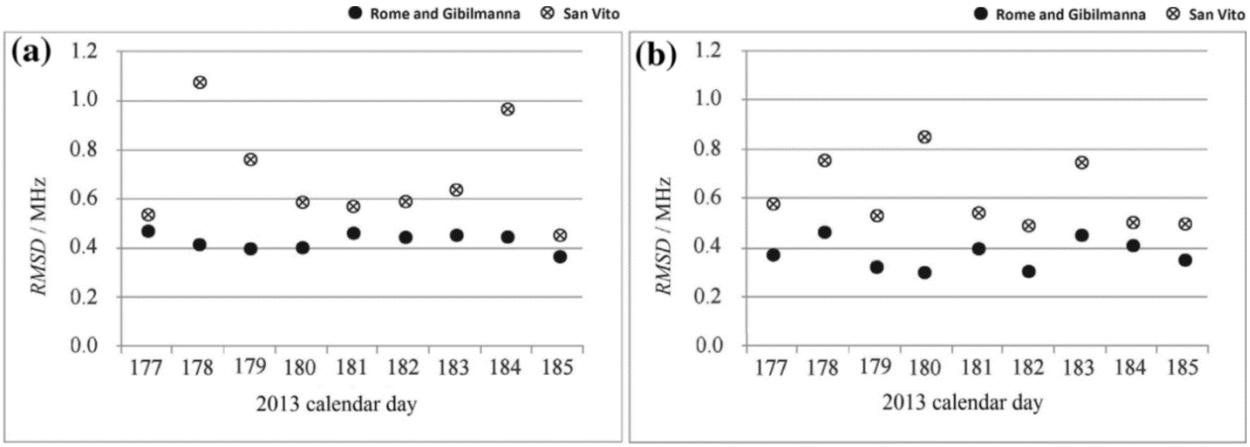

Fig. 4.9. Night-time (a) and day-time (b) averages of $RMSD_{[R\text{-}G]}$ (black circles) and $RMSD_{[SV]}$ (crossed circles) values obtained during test period A, from June 26, 2013 to July 4, 2013, where all available $f_p(h)$ data have been used. (Sabbagh et al., 2016)

	Cases	Adapted	% Adapted	Not adapted	% Not adapted
Quiet	92	88	**95.65**	4	4.35
Disturbed	115	102	**88.70**	13	11.30
Daytime	110	101	**91.82**	9	8.18
Nighttime	97	89	**91.75**	8	8.25
All	207	190	**91.79**	17	8.21

Tab. 4.1. Percentages of success of the adjustment procedure (3rd column, in bold) using all available observed $f_p(h)$ in test period A, referred to each different data class separately (first four rows), and for all available data (last row). The numbers of cases in which $f_p(h)$ are available (1st column), adapted (2nd column), not adapted (4th column), and the percentage of failure of the adjustment procedure are also reported. (Sabbagh et al., 2016)

The accuracy with which f_p is modeled can also be qualitatively assessed by comparing the $f_p(h)$ observed and modeled for the ionospheric station of San Vito. Cases of good and poor accuracy are presented as examples in Fig. 4.11(a)–(h), for different helio-geophysical conditions.
From what shown in Figs. 4.9(a)–(b) and 4.10(a)–(b), and Tables 4.1 and 4.2 it can be seen that RATIM demonstrates a capability to adapt to ionospheric conditions observed at a given moment. In particular, the percentages of success of the adjustment procedure show a slightly higher adaptability in geomagnetically quiet conditions, particularly during period A. Nevertheless, the degree of adaptability can be considered independent of the geomagnetic activity, as can be seen comparing the $RMSD_{[R\text{-}G]}$ values obtained in different days. This degree of adaptability can be assessed as quite good, comparing these values to 0.1 MHz. This value has been assumed as a reference, as it corresponds to the best possible accuracy associated with critical frequency measurements from an ionosonde, according to the International Union of Radio

Science (URSI) standard (Piggott and Rawer, 1972), which assumes manually scaled values by experienced operators.
The $RMSD_{[SV]}$ graphs in the same figures do not show a clear relation between the accuracy with which the algorithm is able to model f_p over the geographical area considered and the geomagnetic activity. Fig. 4.11(a)–(h) shows that cases of poor accuracy can be related to bad modeling of the E valley and/or the F_1 region.
In respect to the model performance during day-time and night-time, the behavior has been different for period A compared to period B. The reason for this difference is unclear and could be clarified by analysis of a wider data set, including several cases of both positive and negative ionospheric storms, in different seasons.

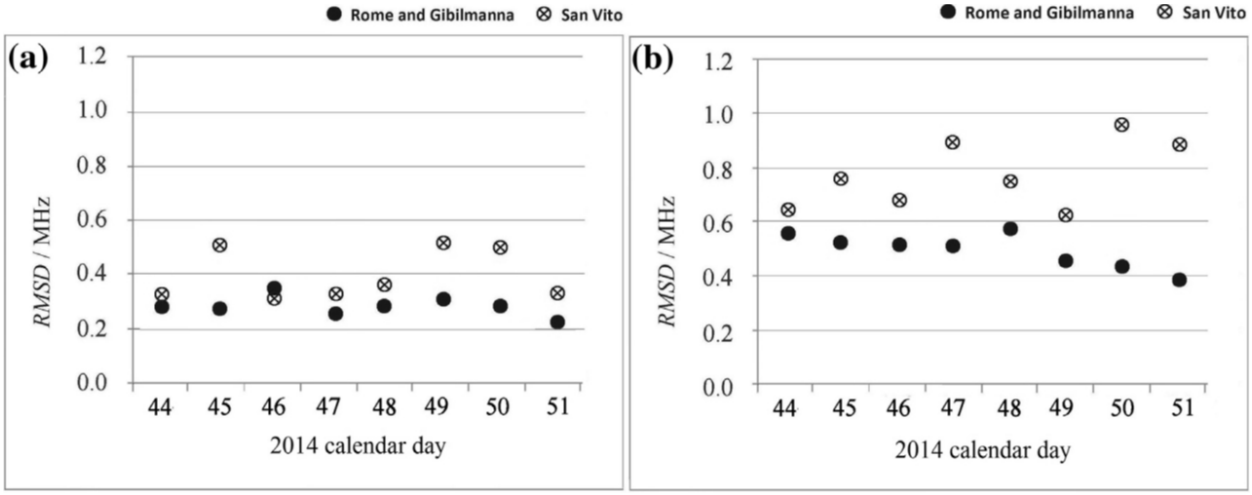

Fig. 4.10. Night-time (a) and day-time (b) averages of $RMSD_{[R-G]}$ (black circles) and $RMSD_{[SV]}$ (crossed circles) values obtained during test period B, from February 13, 2014 to February 20, 2014, where all available $f_p(h)$ data have been used. (Sabbagh et al., 2016)

	Cases	Adapted	% Adapted	Not adapted	% Not adapted
Quiet	48	46	**95.83**	2	4.17
Disturbed	140	132	**94.29**	8	5.71
Daytime	95	85	**89.47**	10	10.53
Nighttime	93	93	**100.00**	0	0.00
All	188	178	**94.68**	10	5.32

Tab. 4.2. Percentages of success of the adjustment procedure (3rd column, in bold) using all available observed $f_p(h)$ in test period B, referred to each different data class separately (first four rows), and for all available data (last row). The numbers of cases in which $f_p(h)$ are available (1st column), adapted (2nd column), not adapted (4th column), and the percentage of failure of the adjustment procedure are also reported. (Sabbagh et al., 2016)

It is worth noting that the reliability of the assimilated $f_p(h)$ is dependent on the automatic ionogram interpretation systems. As mentioned above, these are ARTIST (for the ionospheric station of Rome) and Autoscala (for the ionospheric station of Gibilmanna). To a certain extent, this reliability is also dependent on the quality of the ionograms produced. Although in automatic scaling programs some progress has been made in rejecting bad-quality ionograms and improving the general reliability of the data, some incorrect $f_p(h)$ still slip through (Pezzopane and Scotto, 2005). In this respect, it is interesting to assess the behaviour of an ionospheric model when it is fed some erroneous data. For this purpose, Figs. 4.12(a)–(b), 4.13(a)–(b), Tables 4.3, and 4.4 show corresponding graphs and percentages for those in Figs. 4.9(a)–(b), 4.10 (a)–(b), Tables 4.1, and 4.2 respectively, when only validated $f_p(h)$ were considered. Validation of $f_p(h)$ profiles

has been performed observing the ionograms from which they are restored. $f_p(h)$ considered incorrect have been those associated to ionograms with not enough information (e.g. for blanketing, occultation, absorption or other causes), or in which the F_1 or F_2 critical frequencies have been incorrectly retrieved from the relative ionograms. In these cases, such frequencies can be obtained from the ionograms by an operator, but they are missing in the relative retrieved profiles, or they are incorrectly autoscaled.

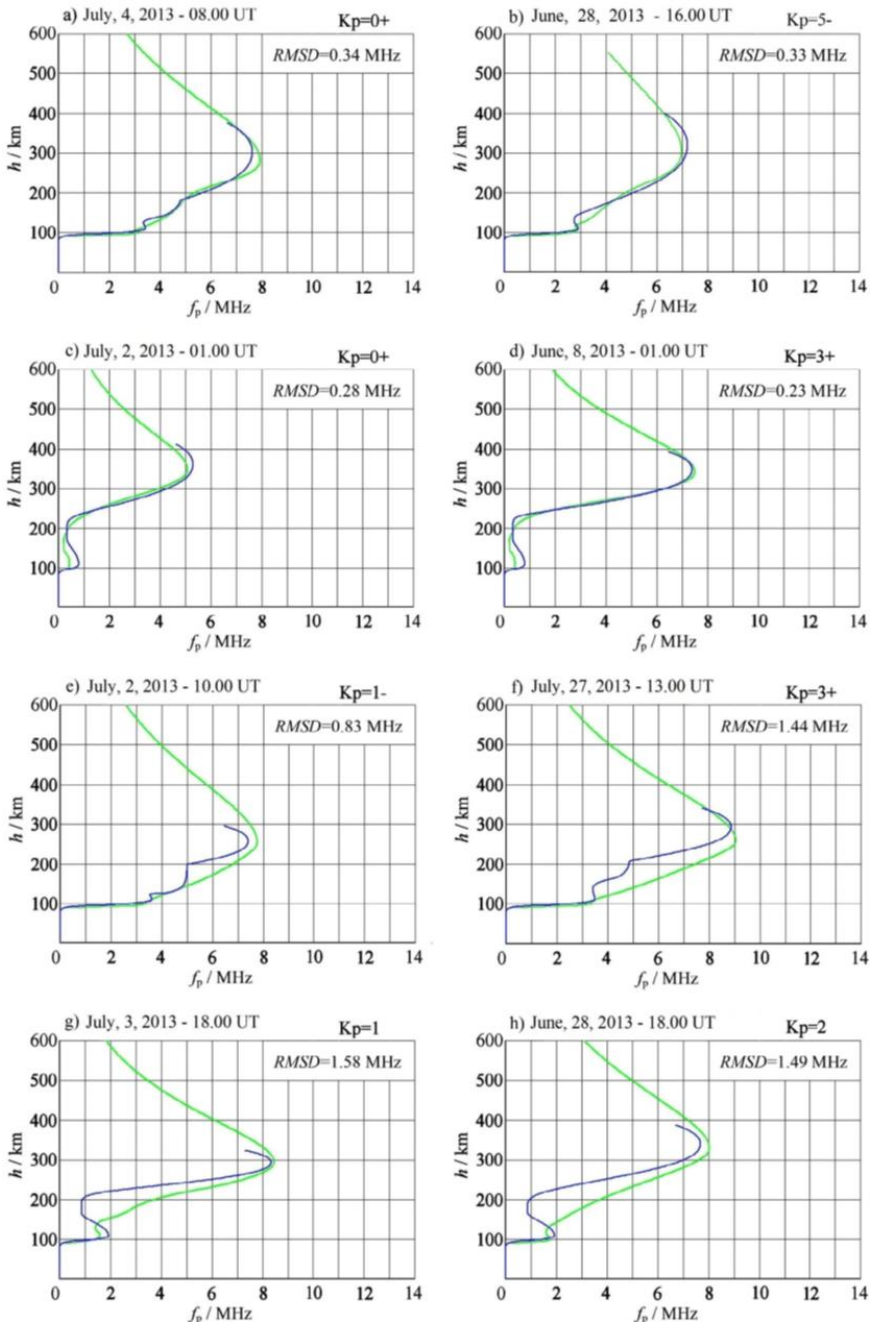

Fig. 4.11. $f_p(h)$ at San Vito dei Normanni (40.6ºN, 18.0ºE), calculated by RATIM (in blue) for geomagnetically quiet days (a), (c), (e), and (g), and geomagnetically disturbed days (b), (d), (f), and (h), in day-time hours (a), (b), (e), and (f), and night-time hours (c), (d), (g), and (h). $f_p(h)$ obtained at the same site from the ionograms of the DPS-4 interpreted by ARTIST (in green) are presented for comparison. From the compared *RMSD* values, cases of quite good accuracy (a)–(d) are shown at the top, and cases of bad accuracy (e)–(h) at the bottom. (Sabbagh et al., 2016)

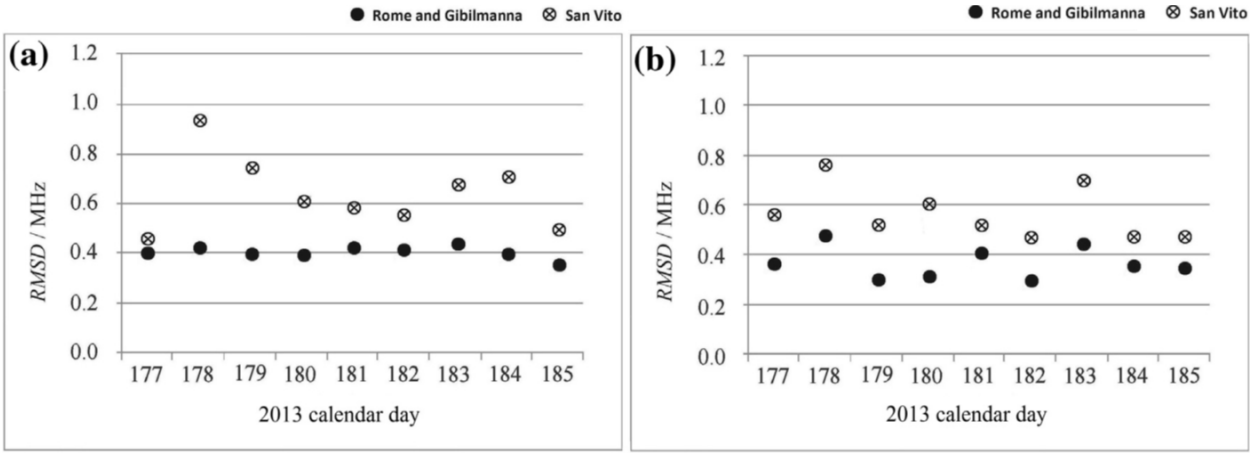

Fig. 4.12. Night-time (a) and day-time (b) averages of $RMSD_{[R\text{-}G]}$ (black circles) and $RMSD_{[SV]}$ (crossed circles) values obtained during test period A, from June 26, 2013 to July 4, 2013, where only validated $f_p(h)$ data have been used. (Sabbagh et al., 2016)

	Cases	Adapted	% Adapted	Not adapted	% Not adapted
Quiet	66	66	**100.00**	0	0.00
Disturbed	86	85	**98.84**	1	1.16
Daytime	75	74	**98.67**	1	1.33
Nighttime	77	77	**100.00**	0	0.00
All	152	151	**99.34**	1	0.66

Tab. 4.3. Percentages of success of the adjustment procedure (3rd column, in bold) using only validated observed $f_p(h)$ in test period A, referred to each different data class separately (first four rows), and for all available data (last row). The numbers of cases in which $f_p(h)$ are available (1st column), adapted (2nd column), not adapted (4th column), and the percentage of failure of the adjustment procedure are also reported. (Sabbagh et al., 2016)

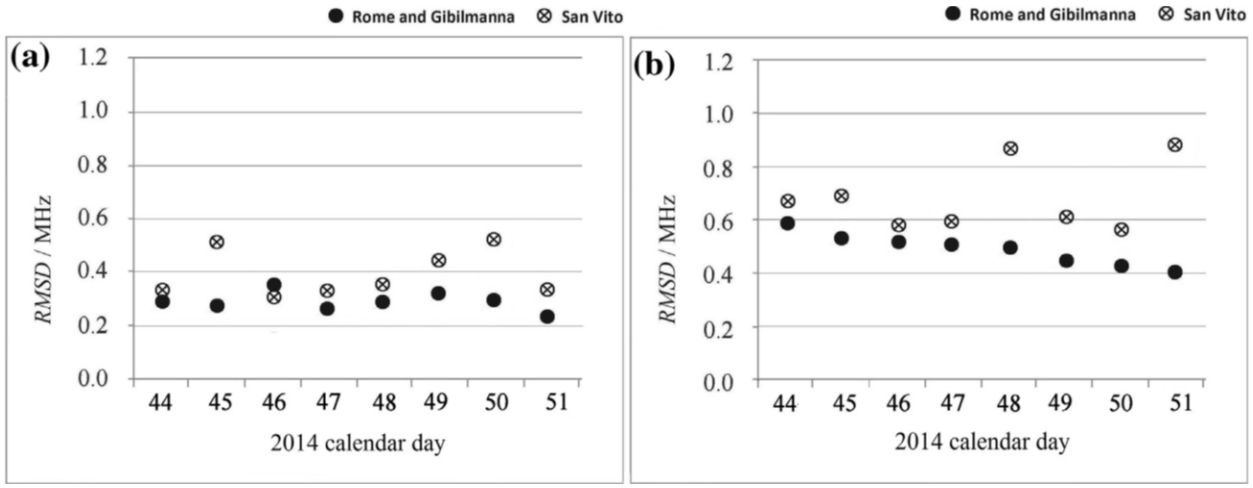

Fig. 4.13. Night-time (a) and day-time (b) averages of $RMSD_{[R\text{-}G]}$ (black circles) and $RMSD_{[SV]}$ (crossed circles) values obtained during test period B, from February 13, 2014 to February 20, 2014, where only validated $f_p(h)$ data have been used. (Sabbagh et al., 2016)

	Cases	Adapted	% Adapted	Not adapted	% Not adapted
Quiet	44	43	**97.73**	1	2.27
Disturbed	116	113	**97.41**	3	2.59
Daytime	68	64	**94.12**	4	5.88
Nighttime	92	92	**100.00**	0	0.00
All	160	156	**97.50**	4	2.50

Tab. 4.4. Percentages of success of the adjustment procedure (3rd column, in bold) using only validated observed $f_p(h)$ in test period B, referred to each different data class separately (first four rows), and for all available data (last row). The numbers of cases in which $f_p(h)$ are available (1st column), adapted (2nd column), not adapted (4th column), and the percentage of failure of the adjustment procedure are also reported. (Sabbagh et al., 2016)

From the results obtained on this selected data set it can be seen that the degree of adaptability is independent of the geomagnetic conditions at the time also when only validated data are considered. Moreover, the discrepancy between the percentages of success of the adjustment procedure obtained during geomagnetically quiet and disturbed days in period A has been significantly reduced.
It is worth noting that the $RMSD_{[SV]}$ values shown in Figs. 4.12(a)–(b) and 4.13(a)–(b) are better than those shown in Figs. 4.9(a)–(b) and 4.10(a)–(b) respectively. This indicates that erroneous input data affects the model's performances in terms of accuracy. On the other hand, the fact that the percentages of success of the adjustment procedure for each different data class shown in Tables 4.3 and 4.4 are higher than the respective values shown in Tables 4.1 and 4.2, indicates that under all conditions the model is able to more frequently fit a correct $f_p(h)$ than an incorrect one. This means that the model exhibits a positive capability of rejecting the low quality $f_p(h)$ that can be produced by automatic scaling systems, even though this capability is still limited. Indeed, the choice of discarding adjustment attempts for which the minimized *RMSD* is greater than 1 MHz permits the model to reject some incorrect $f_p(h)$, even though the percentage of accepted low-quality input data is still high (73.49%). As shown in Chapter 7, the RATIM rejection capability can be improved by the introduction of an assimilation procedure of MUFs values obtained from oblique radio-soundings.
To compare the accuracy achieved during geomagnetic storm conditions to similar efforts, root mean square errors (*RMSE*s) were estimated between observed and modeled f_oF_2 values at San Vito, during geomagnetically disturbed days included in test periods A and B. The results are shown in the first columns of Tables 4.5 and 4.6 for all available observed data and for only validated data, respectively. The second columns of Tables 4.5 and 4.6 report the relative improvements over climatology, computed by the following formula, similar to the formula introduced by Tsagouri and Belehaki (2015) to assess the SWIF model's performance:

$$\%\ \text{improvement} = \frac{RMSE_{\text{median}} - RMSE_{\text{3D model}}}{RMSE_{\text{median}}} \cdot 100, \tag{4.33}$$

where $RMSE_{\text{median}}$ are *RMSE* between f_oF_2 observed values and monthly median values from the climatological IRI2012-CCIR model.
These results have been compared to similar results obtained by Tsagouri and Belehaki (2015) in an assessment of the SWIF model's performance at middle latitudes. For this purpose, Tsagouri and Belehaki (2015) calculated the f_oF_2 *RMSE* and the relative improvement over climatology in Rome during several geomagnetically disturbed periods. The *RMSE* values obtained were from 1.13 MHz and 1.92 MHz, with an average value of 1.49 MHz, while the relative improvement over climatology values were from 16% to 40%, with an average value of 28%. The results obtained from the assessment of RATIM show that the accuracy achieved during geomagnetic storm conditions is better than the SWIF model. The improvement over a climatological description of the ionosphere is also better than SWIFT. Besides, the differences

between the values shown in Table 4.5 and those shown in Table 4.6 can be considered as a further confirmation that erroneous input data for the model affects its performance.

	RMSE (MHz)	% Improvement over climatology
27 June – 1 July 2013	0.52	38
15–20 February 2014	0.53	53
Averages	0.53	45

Tab. 4.5. *RMSE* between observed and modeled f_oF_2 values at San Vito dei Normanni (40.6ºN, 18.0ºE) (1st column), and relative improvement over climatology (2nd column), estimated during geomagnetically disturbed days included in test periods A and B, for all available observed data. (Sabbagh et al., 2016)

	RMSE (MHz)	% Improvement over climatology
27 June – 1 July 2013	0.36	57
15–20 February 2014	0.46	51
Averages	0.41	54

Tab. 4.6. *RMSE* between observed and modeled f_oF_2 values at San Vito dei Normanni (40.6ºN, 18.0ºE) (1st column), and relative improvement over climatology (2nd column), estimated during geomagnetically disturbed days included in test periods A and B, for only validated observed data. (Sabbagh et al., 2016)

Thus, RATIM can be used for real-time estimation of the bottom-side $N(\varphi,\lambda,h)$ over the Italian area, using the ionosonde data assimilation procedure described. As we will see in Chapters 7, it is also suitable for HF ray-tracing applications. Moreover, the degree of adaptability demonstrated can be used to assimilate ionosonde data from oblique radio-soundings with the final aim of estimating N in the sounding region.

References

[1] Sabbagh, D., Scotto, C., Sgrigna, V., 2016. A regional adaptive and assimilative three-dimensional ionospheric model. Adv. Space Res. 57 (5), 1241-1257, doi:10.1016/j.asr.2015.12.038.

[2] Scotto, C., Pezzopane, M., August 2002. A software for automatic scaling of foF2 and MUF(3000)F2 from ionograms. In: Proceeding of URSI XXVIIth General Assembly, Maastricht, Holland, 17–24.

[3] Pezzopane, M., Scotto, C., 2005. The INGV software for the automatic scaling of foF2 and MUF(3000)F2 from ionograms: a performance comparison with ARTIST 4.01 from Rome data. J. Atmos. Solar-Terr. Phys. 67, 1063–1073.

[4] Scotto, C., 2009. Electron density profile calculation technique for Autoscala ionogram analysis. Adv. Space Res. 44, 756–766.

[5] Reinisch, B.W., Huang, X., 2000. Redefining the IRI F1 layer profile. Adv. Space Res. 25, 81–88.

[6] Bilitza, D., Improving the standard IRI B_0 model, Proceedings of the IRI Task Force Activity 1997, Report IC/IR/98/9, pp. 6-14, International Center for Theoretical Physics, Trieste, Italy, 1998a.

[7] Bilitza, D. The E and D region in IRI. Adv. Space Res. 21, 871–878, 1998b.

[8] Davies, K., 1990. Ionospheric Radio. Peter Peregrinus Ltd., London, United Kingdom.

[9] Titheridge, J.E., 2000. Modelling the peak of the ionospheric E-layer. J. Atmos. Solar-Terr. Phys. 62 (2), 93–114.

[10] Mahajan, K.K., Sethi, N.K., Pandey, V.K., 1997. The diurnal variation of E-F valley parameters from incoherent scatter measurement at Arecibo. Adv. Space Res. 20, 1781–1784.

[11] Jones, W.B., Gallet, R.M., 1962. Representation of diurnal and geographic variations of ionospheric data by numerical methods. J. Res. Nat. Bureau Stand. -D. Radio Propag. 66D, 419–438.

[12] Jones, W.B., Graham, R.P., Leftin, M.D, 1969. Advances in ionospheric mapping by numerical methods. ESSA Tech. Rep. ERL 107 – ITS 75, US Government Printing Office, Washington, DC.

[13] Bilitza, D., 1986. International reference ionosphere: Recent developments. Radio Sci. 21 (3), 343–346.

[14] Rawer, K., Bilitza, D., 1989. Electron density profile description in the international reference ionosphere. J. Atmos. Terr. Phys. 51 (9/10), 781–760.

[15] Rawer, K., 1963. Propagation of decameter waves (HF band). Meteorological and Astronomical Influences on Radio Wave Propagation. New York Academic Press, 221-250.

[16] Bradley, P.A., Dudeney, J.R., 1973. Simple model of the vertical distribution of electron concentration in the ionosphere. J. Atmos. Terr. Phys. 35, 2131–2146.

[17] DuCharme, E. D., Petrie, L. E., Eyerig, R., 1971. A method for predicting the Fl layer critical frequency. Radio Sci. 6 (3), 369–378.

[18] DuCharme, E.D., Petrie, L.E., 1973. A method for predicting the F1 layer critical frequency based on the Zurich smoothed sunspot number. Radio Sci. 8, 837–839.

[19] Buresova, D., 2005. Effects of geomagnetic storms on the bottomside ionospheric F region. Adv. in Space Res. 35, 429–439.

[20] Kushnarenko, G.P., Kuznetsova, G.M, Kolpakova, O.E., 2010. Reaction of the Ionospheric F1 Region to Disturbances in October and November 2003 (Analysis from Irkutsk Digisonde Measurements). ISSN 0016-7932, Geomagnetism and Aeronomy 50, No. 8 (Special Issue 2), pp. 1015–1020.

[21] Gordienko, G.I., Vodyannikov, V.V., Yakovets, A.F., 2011. Geomagnetic storm effects in the ionospheric E- and F-regions. Journal of Atmospheric and Solar-Terrestrial Physics 73, 1818–1830.

[22] Haines, D.M., 1994. A Portable Ionosonde Using Coherent Spread Spectrum Waveforms for Remote Sensing of the Ionosphere, UMLCAR.

[23] Reinisch, B.W., Huang, X., 1983. Automatic calculation of electron density profiles from digital ionograms 3. Processing of bottomside ionograms. Radio Sci. 18 (3), 477–492.

[24] Zuccheretti, E., Tutone, G., Sciacca, U., Bianchi, C., Arokiasamy, B. J., 2003. The new AIS-INGV digital ionosonde. Ann. Geophys. 46 (4), 647–659.

[25] Araujo-Pradere, E.A., Fuller-Rowell, T.J., 2002. STORM: an empirical storm-time ionospheric correction model 2. Validation. Radio Sci. 37 (5), 1070. http://dx.doi.org/10.1029/2002RS002620.

[26] Araujo-Pradere, E.A., Fuller-Rowell, T.J., Codrescu, M.V., 2002. STORM: an empirical storm-time ionospheric correction model 1. Model description. Radio Sci. 37, 1070. http://dx.doi.org/10.1029/2001RS002467.

[27] Araujo-Pradere, E.A., Fuller-Rowell, T.J., Bilitza, D., 2003. Validation of the STORM response in IRI2000. J. Geophys. Res. 108 (A3), 1120. http://dx.doi.org/10.1029/20032002JA009720.

[28] Mikhailov, A.V., Perrone, L., 2014. A method for foF2 short-term (1–24 h) forecast using both historical and real-time foF2 observations over European stations: EUROMAP model. Radio Sci. 49 (4), 253–270. http://dx.doi.org/10.1002/2014RS005373.

[29] Bremer, J., Cander, Ly.R., Mielich, J., Stamper, R., 2006. Derivation and test of ionospheric activity indices from real-time ionosonde observations in the European region. J. Atmos. Solar-Terr. Phys. 68, 2075–2090.

[30] Mielich, J., Bremer, J., 2010. A modified index for the description of the ionospheric short- and long-term activity. Ann. Geophys. 28 (12), 2227–2236. http://dx.doi.org/10.5194/angeo-28-2227-2010.

[31] Belehaki, A., Cander, Ly.R., Zolesi, B., Bremer, J., Juren, C., Stanisławska, I., Dialetis, D., Hatzopoulos, M., 2007. Ionospheric specification and forecasting based on observations from European ionosondes participating in DIAS project. Acta Geophys. 55 (3), 398–409.

[32] Durgonics, T., Komjathy, A., Verkhoglyadova, O., Shume, E.B., Benzon, H.-H., Mannucci, A.J., Butala, M.D., Høeg, P., Langley, R.B., 2017. Multiinstrument observations of a geomagnetic storm and its effects on the Arctic ionosphere: A case study of the 19 February 2014 storm. Radio Sci. 52, 146–165. doi:10.1002/2016RS006106.

[33] Piggot, W.R., Rawer, K., 1972. URSI Handbook of Ionogram Interpretation and Reduction, second ed. Elsevier, New York, 325 pp.

[34] Tsagouri, I., Belehaki, A., 2015. Ionospheric forecasts for the European region for space weather applications. J. Space Weather Space Clim. 5 (A9). http://dx.doi.org/10.1051/swsc/2015010.

5. RATIM improvements during solar eclipse periods

During a solar eclipse, it is possible to investigate changes in the ionosphere as a response to the sudden decrease in solar radiation. Since the first half of the twentieth century, it was assumed that an eclipse would affect the ionization of the upper and lower layers of the ionosphere. Therefore, radio-telegraphic investigations were performed during the solar eclipse involving South America and Africa on May 29, 1919 (Eccles, 1919). A reduction in plasma density was observed in some subsequent papers (Gledhill, 1959a; Gledhill, 1959b) and attempts were made to establish the recombination coefficients (Beynon, 1955). Moreover, irregularities, tilts, and sporadic E (E_s) layers were also observed and reported by numerous researchers (McLeish, 1948; Minnis, 1954; Minnis, 1956; Bramley, 1956; Bates and McDowell, 1957; Beynon, 1955).

The achievements reported by different authors for the E, F_1, and F_2 mid-latitude regions are very interesting in this context. A lot of information was obtained by studying the ionospheric responses to the eclipse that occurred on August 11, 1999, with a path of totality passing over central Europe so that it could be measured by an extensive ionosonde network (Stanislawska et at., 2001; Le et al., 2008; Farges et al., 2001; Altadill et al. 2001).

As a result, today it is considered proven that the redistribution of plasma during an eclipse can lead to changes in the form of $N(h)$, observable using ionosondes. It is also considered certain that the relative decrease of ionization is most noticeable in the bottom-side ionosphere, at around 200 km altitude, where the photoionization is high, and recombination is efficient. If dynamic forces are ignored, such as thermospheric winds or electric fields, an increase should be observed in the peak height h_mF_2 as well as an increase of the layer thickness expressible through B_0. In quiet conditions, it is reasonable to ignore dynamic forces like thermospheric winds or electric fields, and diffusive transport processes are expected to dominate. In these circumstances, a delayed response to obscuration should be observed, and the delay should increase with height (Jackowski et al., 2008).

In this work, the effects of the partial solar eclipse of March 20, 2015 on different ionospheric layers have been studied over Italy, with the aim to test RATIM performance during eclipse periods. The study is performed using vertical ionospheric soundings from the ionosondes of Rome (41.8º N, 12.5º E), Gibilmanna (37.9º N, 14.0º E), and San Vito dei Normanni (40.6º N, 18.0º E). In particular, the response of the critical frequencies has been investigated during the solar eclipse, and corrections taking into account the decreased solar irradiance have been proposed for the empirical formulations used for their estimation. The effect of the decreased solar irradiance has been modeled as a Solar Obscuration Factor (*SOF*), and comparisons with experimental values have been performed. The RATIM behaviour has been then tested, assimilating plasma frequency profiles $f_p(h)$ during the solar eclipse. Testing the model in such unusual conditions has thus enabled the introduction of the corrections proposed, improving RATIM performance during solar eclipse events.

5.1 Eclipse characterization with the Solar Obscuration Factor

This work applied a fairly simple approach for modeling the time behaviour of the Solar Obscuration Factor (*SOF*) during the evolution of an eclipse, with *SOF* defined as the fraction of the Sun's area blocked by the Moon. The applied model is similar to that used by Möllmann and Vollmer (2006), with the Sun and Moon assumed to follow a straight and uniform motion, and both to be circular in shape, ignoring any effects of limb darkening. The input parameters include the beginning of the eclipse, its duration, and the value of *SOF* at maximum. Fig. 5.1 shows the time evolution of *SOF* obtained at the ionospheric stations of Rome, Gibilmanna, and San Vito during the March 20, 2015 eclipse. For each curve, the time of the maximum *SOF* value is highlighted with a dashed vertical line to show the temporal shift of *SOF* maximum at different

locations. The relative amplitude of the maximums on the different curves is also clearly shown in the figure.

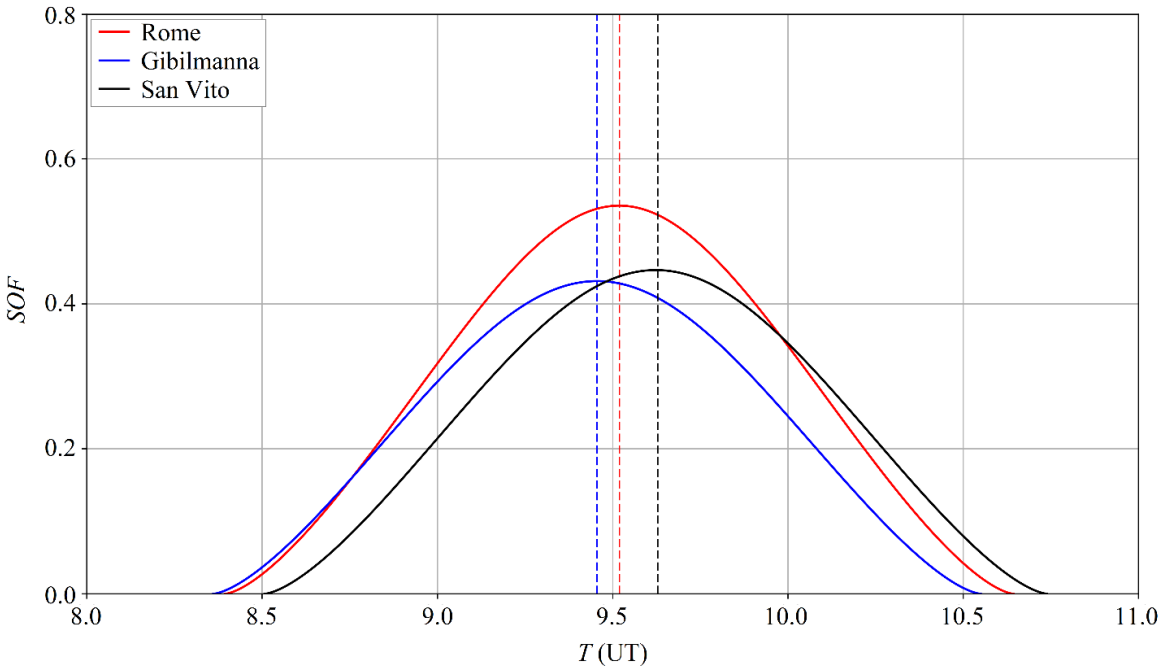

Fig. 5.1. Time evolution of *SOF* obtained at the ionospheric stations of Rome (41.8ºN, 12.5ºE), in red, Gibilmanna (37.9ºN, 14.0ºE), in blue, and San Vito dei Normanni (40.6ºN, 18.0ºE), in black, obtained using a simplified model. For each curve, the time of the maximum *SOF* value is highlighted with a dashed vertical line.

The same procedure has been used to obtain similar *SOF* curves at different locations within Italy. These values have been then used to draw *SOF* maps during the eclipse in the region of latitude from 36.0º N to 47.5º N and longitude from 6.0º E to 19.0º E, by a linear interpolation procedure. The *SOF* maps obtained from 08:30 UT to 10:30 UT every 15 minutes are reported in Fig. 5.2(a)-(i).
To perform the *SOF* linear interpolation, 14 points in the considered region have been taken. In particular, the corner points with coordinates (φ, λ) equal to (6.0º E, 36.0º N), (6.0º E, 47.5º N), (19.0º E, 36.0º N), and (19.0º E, 47.5º N), and 10 other points inside the area in distinct locations have been selected, in order to cover the entire region. From the sequence of the *SOF* maps obtained, the temporal evolution of the obscuration over the considered area can be deduced. At first, the shadow come from SW (Fig. 5.2(a)), moving towards north while approaching the time when maximum obscuration is observed (Fig. 5.2(b)-(e)). Finally, the shadow fades moving towards NE (Fig. 5.2(f)-(i)). The pattern shown is consistent with the path of totality reported in Fig. 5.3, along with the map of the eclipse obscuration over the Earth's surface during the solar eclipse.
Another assumption considered modeling the solar eclipse is that the Sun's disk has homogeneous luminosity, ignoring any variation due to sunspots. Under these hypotheses the reduction in solar radiation due to the eclipse is assumed to be proportional to the *SOF*:

$$I_{\infty[\text{eclipse}]}=(1-SOF)\cdot I_{\infty}, \tag{5.1}$$

where $I_{\infty[\text{eclipse}]}$ and I_{∞} are the intensity of solar radiation at the upper limit of the atmosphere in the presence or absence of the eclipse, respectively. An estimation of the decrease in solar radiation due to the progress of the eclipse is useful in order to study the decrease in ionization in the different ionospheric layers.

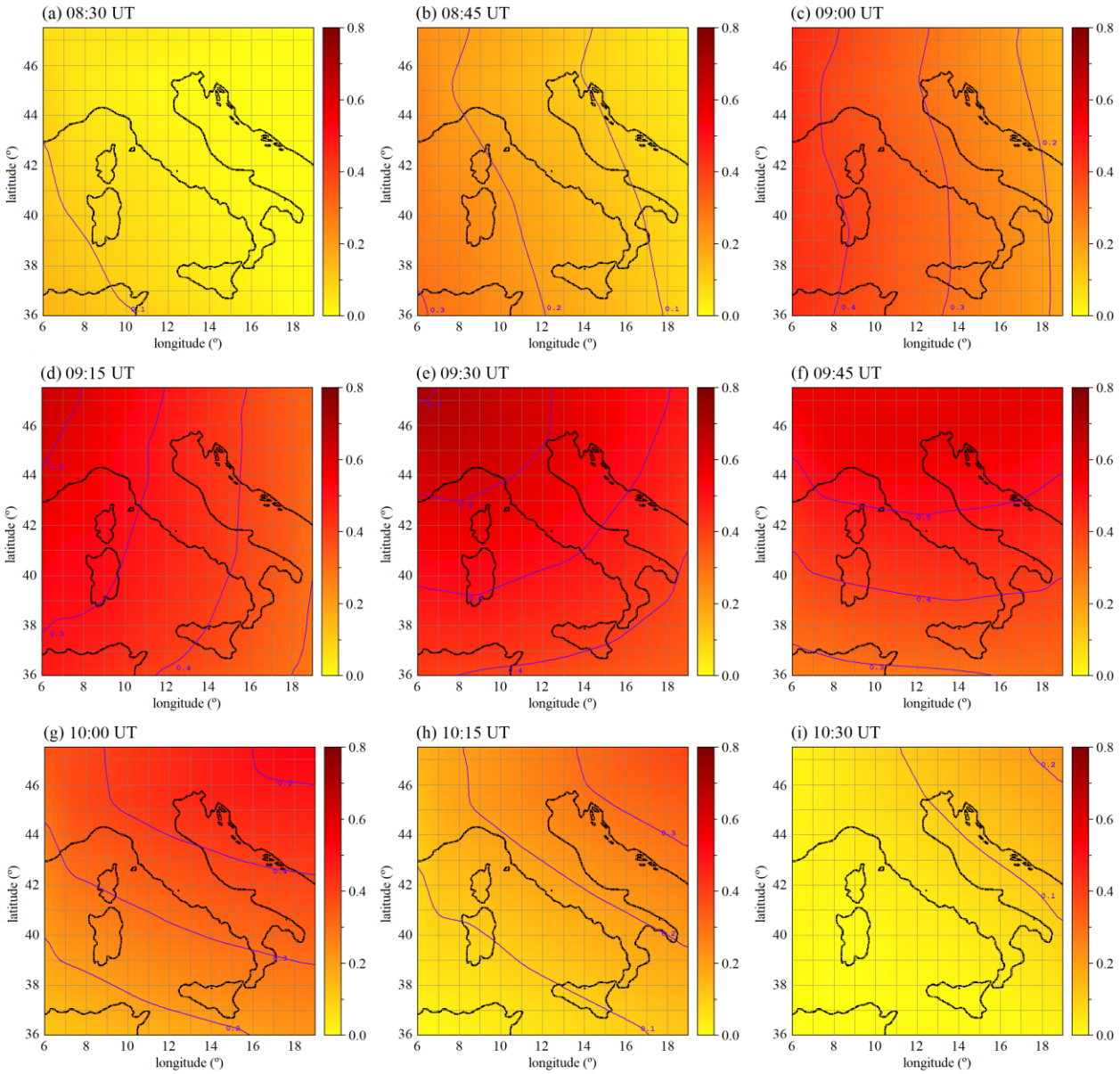

Fig. 5.2. Maps of *SOF* in the region of latitude from 36.0º N to 47.5º N and longitude from 6.0º E to 19.0º E, calculated every 15 minutes from 08:30 UT to 10:30 UT, during the eclipse of March 20, 2015. These maps have been obtained by a linear interpolation in space of the *SOF* values computed at different locations in the area considered.

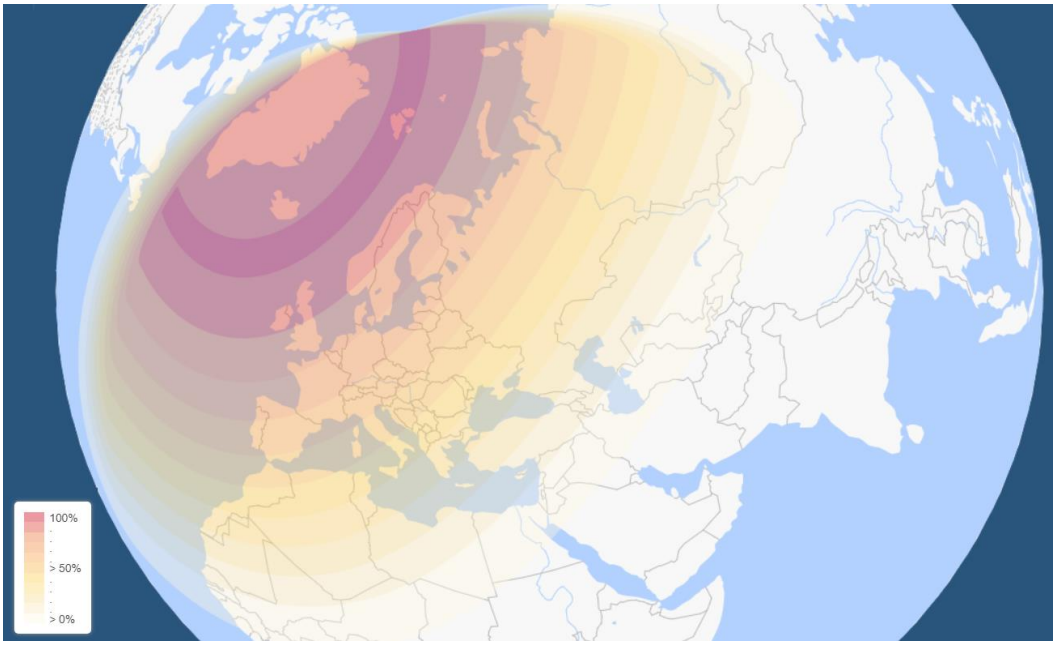

Fig. 5.3. Obscuration caused by the Moon shadow during the March 20, 2015 solar eclipse over the Earth's surface (https://www.timeanddate.com/eclipse/globe/2015-march-20). The path of totality corresponds to the region where the coverage percentage reaches 100%.

5.2 Effects of the eclipse on the E layer

It is well known that the E layer behaves like a Chapman layer, and so its critical frequency can be modeled with a good approximation as:

$$f_oE_{[mod]}=[q(\chi=0,\ h=h_mE)\cdot\cos(\chi)/\alpha]^{1/4}, \tag{5.2}$$

where $q(\chi=0,\ h=h_mE)$ is the maximum production rate, which occurs at the height h_mE and when the Sun is at its zenith (i.e. when the solar zenith angle is $\chi=0$), and α is the recombination coefficient. It should also be noted that in (5.2) it can be assumed:

$$q(\chi=0,\ h=h_m)\propto I_\infty. \tag{5.3}$$

Consequently, the critical frequency $f_oE_{[eclipse]}$, when the intensity of the ionizing radiation is decreased by a factor (1–*SOF*), can be modeled as:

$$f_oE_{[eclipse]}=f_oE_{[mod]}\cdot(1-SOF)^{1/4}, \tag{5.4}$$

where for numerical computational purposes, $f_oE_{[mod]}$ can be modeled following (4.1a), according to the specified functional dependence on χ and R_{12} (Davies, 1990). However, in this work an equivalent R_{12} value has been used, obtained from the empirical formula (Leitinger et al., 2005):

$$R_{12}=[167273+(F10.7-63.7)\cdot1123.6]^{0.5}-408.99, \tag{5.5}$$

where F10.7 is the solar radio flux at 10.7 cm. Relationship (5.5) is derived according to the ITU Recommendation (1999), in which twelve-months smoothed F10.7 values were used. In this work, the daily

F10.7 value for March 20, 2015 has been applied, since the interest is for a solar activity index representative of the specific day of the eclipse.

Fig. 5.4(a)-(c) shows the trends as a function of time of $f_oE_{[mod]}$, as provided by (4.1a), and $f_oE_{[eclipse]}$ provided by (5.4), along with the available experimental values $f_oE_{[obs]}$, manually scaled from the ionograms recorded every 15 minutes at the ionospheric stations of Rome, Gibilmanna, and San Vito. Unfortunately, in many cases the cusp of the E region could not be clearly identified in the available ionograms, as a result of the combined effects of the limited efficiency of the receiving antennas at low frequencies, absorption in the D region, and the E_s layer blanketing effect. As a result, only few data are available at Rome and during the eclipse recovery phase at Gibilmanna, while no data have been retrieved from San Vito ionograms.

To relate the trends of $f_oE_{[obs]}$, $f_oE_{[mod]}$, and $f_oE_{[eclipse]}$ to the evolution in time of the *SOF* at each station, Fig. 5.4(a)-(c) also reports the relative *SOF* curves, with the time of the maximum *SOF* value highlighted with a dashed vertical line. Computing the values of χ at any location for fixed times, $f_oE_{[eclipse]}$ maps have been obtained during the eclipse in the region of latitude from 36.0ºN to 47.5ºN and longitude from 6.0ºE to 19.0ºE. The $f_oE_{[eclipse]}$ maps obtained every 15 minutes from 08:30 UT to 10:30 UT are reported in Fig. 5.5(a)-(i).

Although few experimental data are available for the E layer critical frequency, the trends of the $f_oE_{[obs]}$ values observed during the eclipse window reported in Fig. 5.4(a)-(c) show a clear decrease in the peak electron density, as a consequence of the sudden reduction of the solar irradiance. However, because of the few experimental data, the agreement between $f_oE_{[eclipse]}$ values computed by the corrective formulation (5.4) cannot be assessed conclusively good. In particular, the *RMSD* between $f_oE_{[obs]}$ and $f_oE_{[eclipse]}$ computed over the few data available at Rome, equal to 0.13 MHz, is close to the value obtained considering $f_oE_{[mod]}$, that is 0.17 MHz. Nevertheless, the *RMSD* computed over the Gibilmanna data decreases from 0.33 MHz to 0.08 MHz when the *SOF*-related correction (5.4) is introduced. Indeed, it can be easily seen from Fig. 5.4(b) that the $f_oE_{[obs]}$ values obtained at Gibilmanna during the eclipse window are much closer to the relative $f_oE_{[eclipse]}$ values than to the corresponding $f_oE_{[mod]}$. Moreover, the $f_oE_{[eclipse]}$ curves seem to be reasonable, since they follow the *SOF* curve trends in counter-phase at the relative locations. The capability of formulation (5.4) to follow the eclipse effects can also be inferred from Fig. 5.5(a)-(i), as the isolines shown there match the shape of the *SOF* isolines shown in Fig. 5.2(a)-(i).

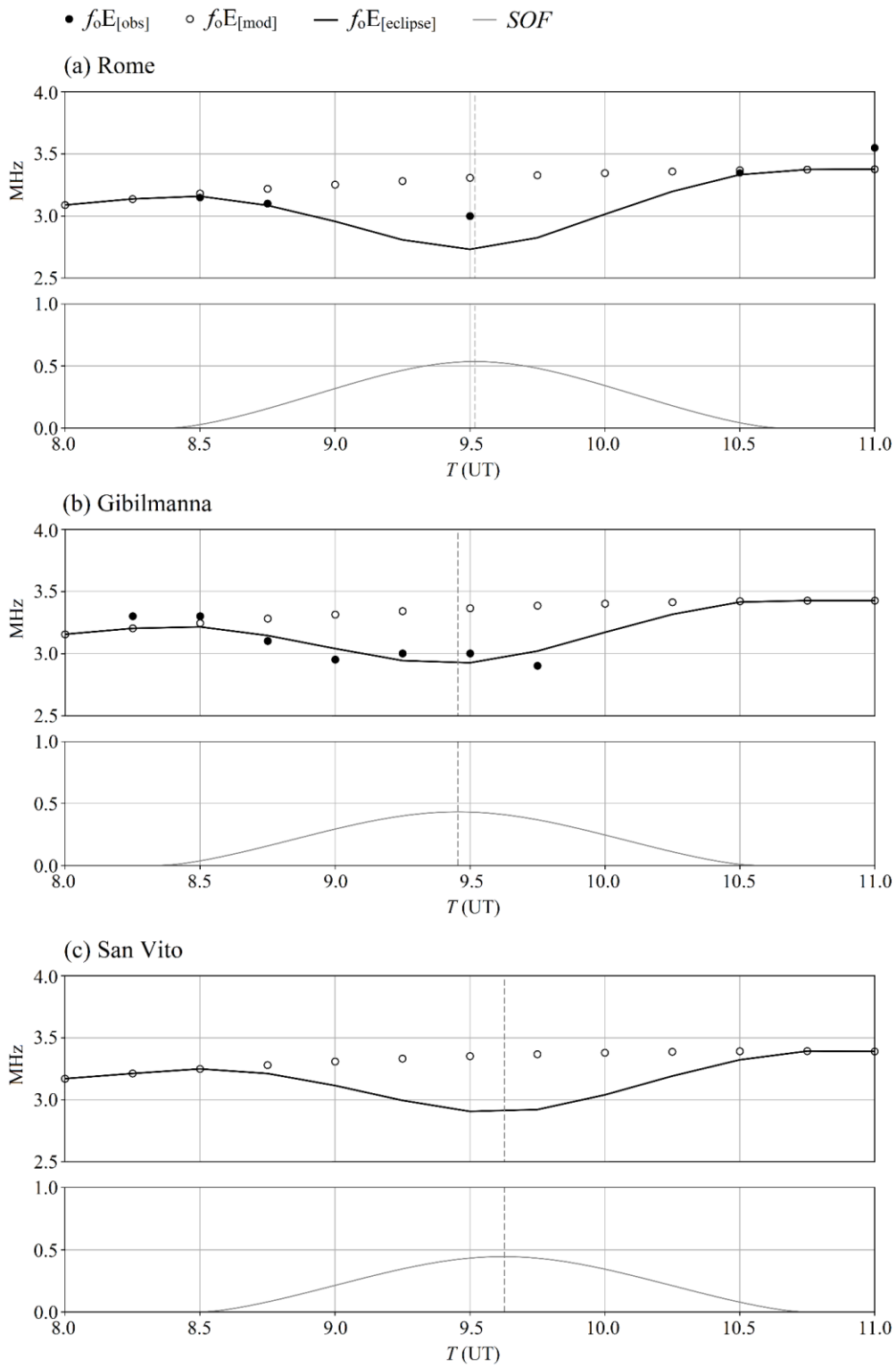

Fig. 5.4. Trends as a function of time from 08:00 UT to 11:00 UT of $f_oE_{[obs]}$, $f_oE_{[mod]}$, and $f_oE_{[eclipse]}$ at the ionospheric stations of Rome (41.8º N, 12.5º E) (a), Gibilmanna (37.9º N, 14.0º E) (b), and San Vito dei Normanni (40.6º N, 18.0º E) (c) during the eclipse of March 20, 2015. The trends are related to the evolution in time of the *SOF* at each station, and the time of the maximum *SOF* value is highlighted with a dashed vertical line. In many cases the cusp of the E region could not be clearly identified from the available ionograms and so only a few $f_oE_{[obs]}$ values are available in some cases.

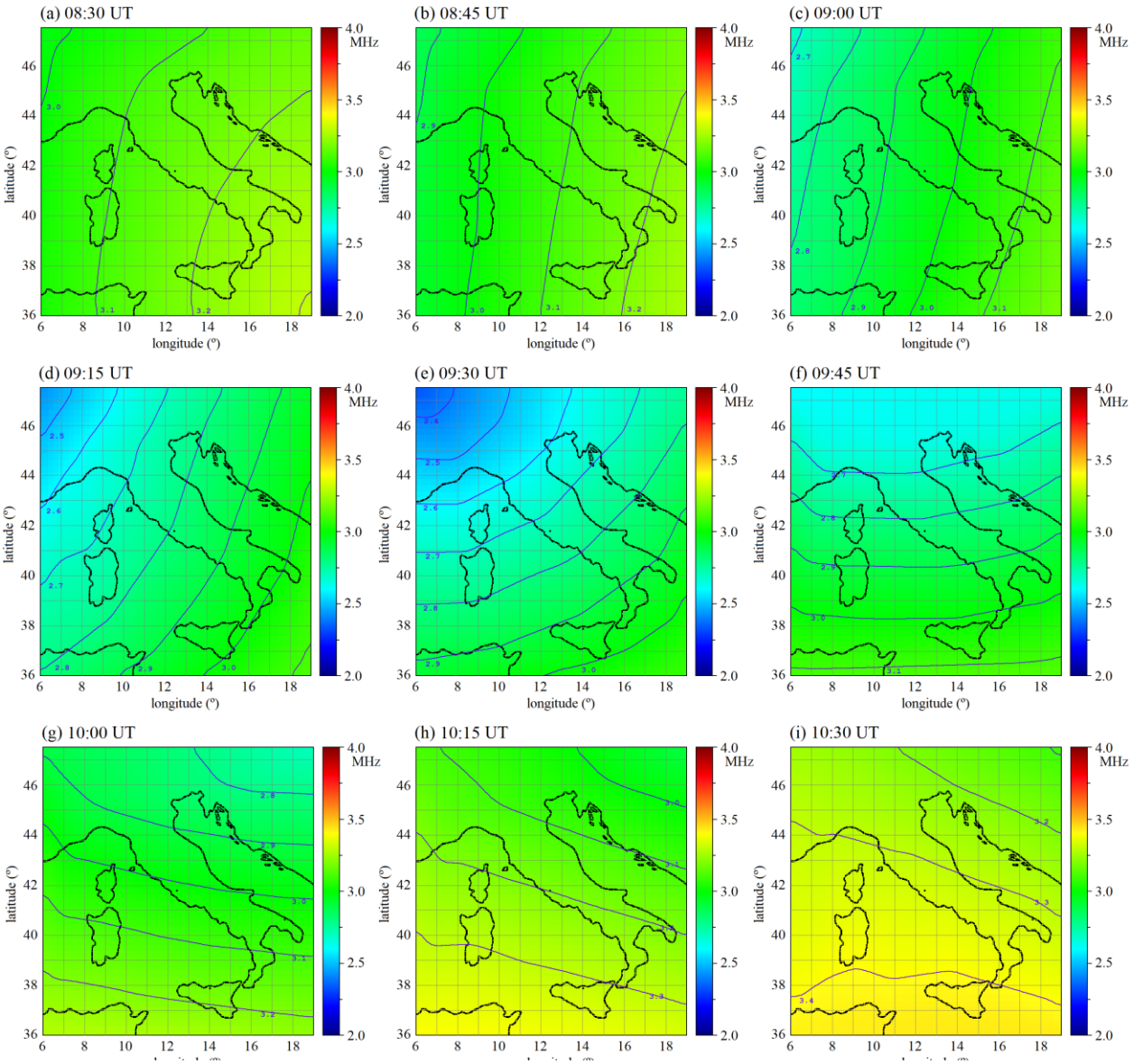

Fig. 5.5. Maps of $f_oE_{[eclipse]}$ in the region of latitude from 36.0º N to 47.5º N and longitude from 6.0º E to 19.0º E, calculated from 08:30 UT to 10:30 UT during the eclipse of March 20, 2015. These maps have been obtained by computing the values of χ every 15 minutes at any location in the area considered.

5.3 Effects of the eclipse on the F_1 layer

As seen in Section 4.2, the semi-empirical DuCharme et al. (1971, 1973) formulation (4.13)-(4.17) is often used to calculate f_oF_1 for a specified geographic position, taking into account the solar activity and geomagnetic coordinates of the site. This formulation assumes limits for the presence of f_oF_1 as a function of χ and the solar activity given by the R_{12} index, which imply that f_oF_1 ionization is never present during winter or during night-time. However, the validity of the DuCharme et al. formula for predicting values of f_oF_1 was confirmed by Scotto et al. (1997) including zenith angles beyond the limits specified in the original paper.

When an extraordinary event, such as a solar eclipse, occurs, this formula is expected not to be able to describe the f_oF_1 variations. In order to describe the decrease in f_oF_1 during such events, the *SOF* was

introduced in the DuCharme et al. formula (4.13) as a correction factor. Hence, the following formula for f_oF_1 estimation during an eclipse has been proposed:

$$f_oF_{1[eclipse]} = f_oF_{1[mod]} \cdot (1 - SOF)^{\eta}, \tag{5.6}$$

in accordance to the law expressed by the DuCharme et al. formulation (4.13). To describe the behaviour of f_oF_1 during the solar eclipse the $f_oF_{1[obs]}$ values manually scaled from the ionograms recorded every 15 minutes at the ionospheric stations of Rome, Gibilmanna, and San Vito have been compared with:

a) the values of f_oF_1 provided by the DuCharme et al. formulation (4.13)-(4.17) which, instead of R_{12}, have been used the equivalent R_{12} values obtained from (5.5), using F10.7 for March 20, 2015;
b) the values of f_oF_1 provided by the DuCharme et al. formula specified in point a), corrected according to (5.6).

The values for this comparison are reported in Fig. 5.6(a)-(c), along with the evolution in time of the *SOF* at each station, where the time of the maximum *SOF* value is highlighted with a dashed vertical line. Fig. 5.7(a)-(i) shows the $f_oF_{1[eclipse]}$ maps obtained every 15 minutes from 08:30 UT to 10:30 UT in the region of latitude from 36.0° N to 47.5° N and longitude from 6.0° E to 19.0° E, with the computation of χ in the area considered for the fixed times.
As shown in Fig. 5.6(a)-(c), $f_oF_{1[eclipse]}$ values computed by the corrective formulation (5.6) provide close agreement with experimental $f_oF_{1[obs]}$ values. Nevertheless, the $f_oF_{1[eclipse]}$ curves do not match perfectly $f_oF_{1[obs]}$ values, particularly in some cases, like quite often at Rome (Fig. 5.6(a)) and during the eclipse recovery phase at San Vito (Fig. 5.6(c)), where few experimental data are available. However, *RMSD* values obtained confirm that $f_oF_{1[eclipse]}$ values are closer to observations than $f_oF_{1[mod]}$ ones. Indeed, the *RMSD*s calculated during the eclipse window decrease from 0.55 MHz to 0.19 MHz at Rome, from 0.39 MHz to 0.11 MHz at Gibilmanna, and from 0.42 MHz to 0.13 MHz at San Vito, when correction (5.6) is introduced. Moreover, even in this case the $f_oF_{1[eclipse]}$ curves follow the *SOF* curve trends in counter-phase at the relative locations, and the capability of formulation (5.6) to follow the eclipse effects can also be inferred from Fig. 5.7(a)-(i), as the isolines shown there match the shape of the *SOF* isolines shown in Fig. 5.2(a)-(i).

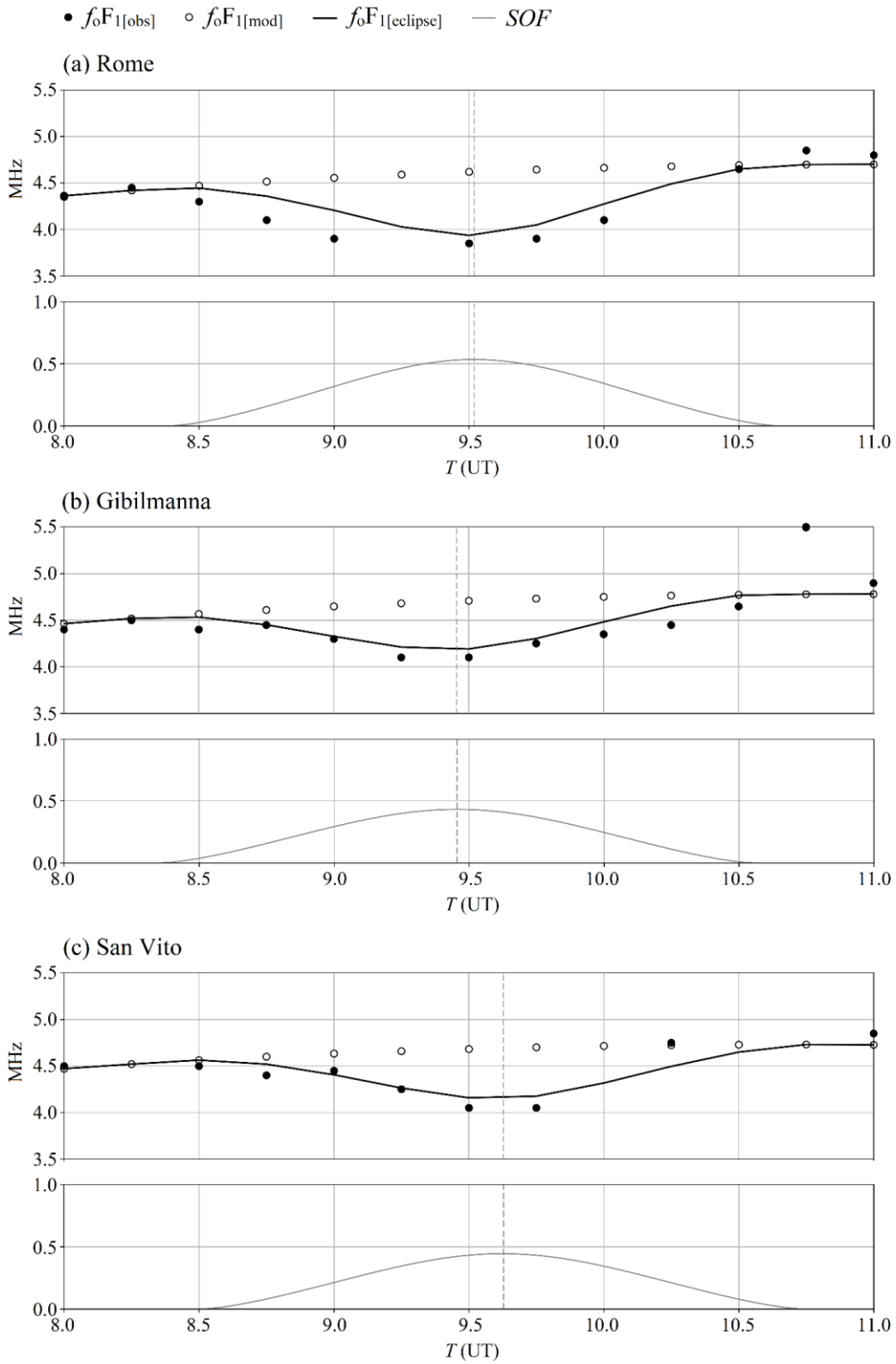

Fig. 5.6. Trends as a function of time from 08:00 UT to 11:00 UT of $f_oF_{1[obs]}$, $f_oF_{1[mod]}$, and $f_oF_{1[eclipse]}$ at the ionospheric stations of Rome (41.8º N, 12.5º E) (a), Gibilmanna (37.9º N, 14.0º E) (b), and San Vito dei Normanni (40.6º N, 18.0º E) (c) during the eclipse of March 20, 2015. The trends are related to the evolution in time of the *SOF* at each station, and the time of the maximum *SOF* value is highlighted with a dashed vertical line.

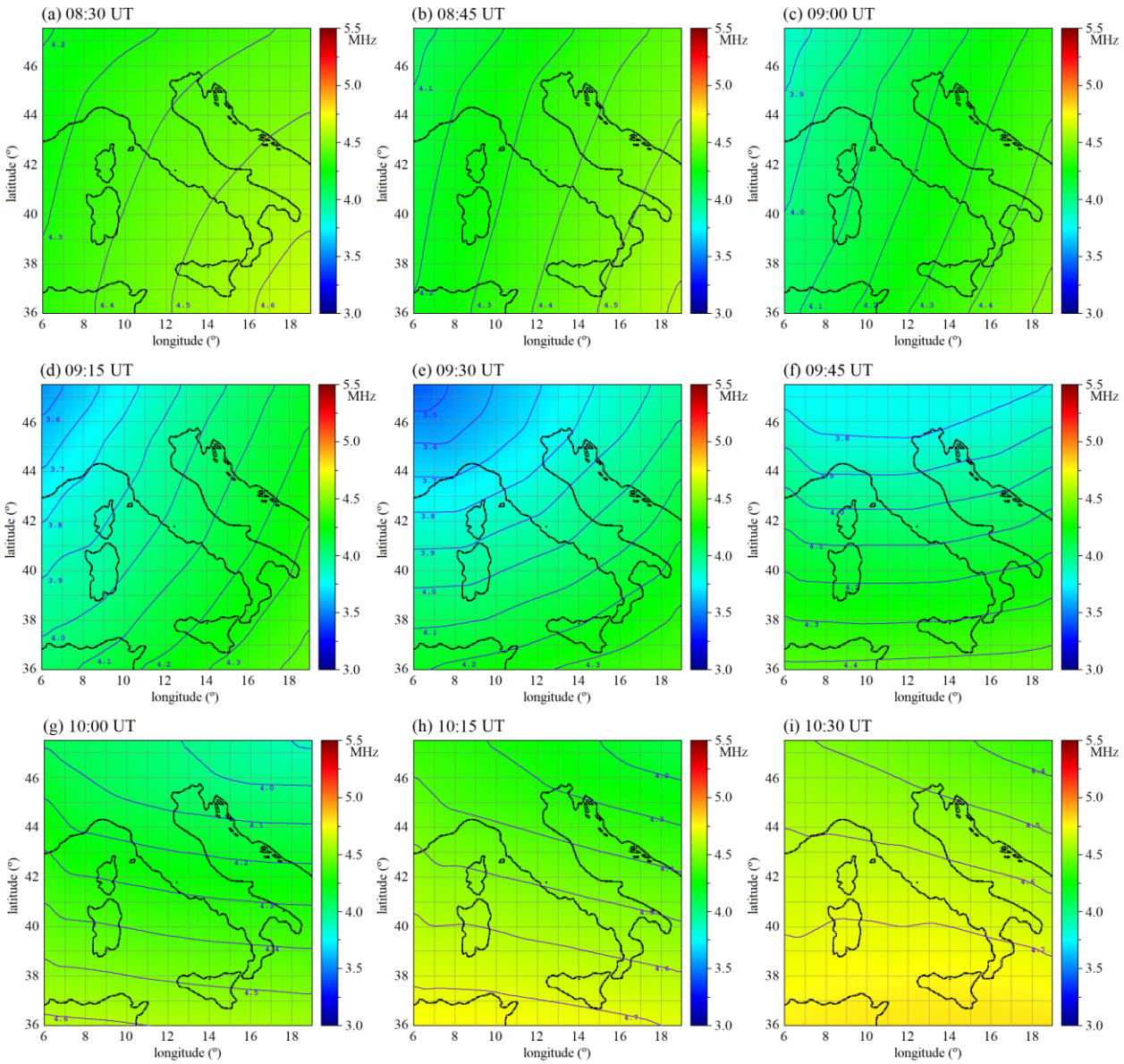

Fig. 5.7. Maps of $f_oF_{1[eclipse]}$ in the region of latitude from 36.0º N to 47.5º N and longitude from 6.0º E to 19.0º E, calculated from 08:30 UT to 10:30 UT during the eclipse of March 20, 2015. These maps have been obtained by computing the values of χ every 15 minutes at any location in the area considered.

5.4 Effects of the eclipse on the F_2 layer

As for E and F_1 layers critical frequencies, the empirical formulation generally used to calculate monthly median f_oF_2 values over the Earth's surface is expected to fail during a solar eclipse event, in which the sudden decrease in solar radiation produces strong changes in the ionospheric dynamics.

As seen in Section 4.2, the commonly used way to model monthly median f_oF_2 values is through the mapping procedure used in the IRI model (Jones and Gallet, 1962; Jones et al., 1969), in accordance to formulas (4.8) and (4.9). The values of the coefficients in these relations are based on observations, being adjusted in order to fit data to mathematical functions with no physical meaning. This is to be ascribed to the different behaviour of the F_2 layer, quite far from that of a Chapman layer, in which the dominant

photochemical processes give rise to a χ control of the critical frequency. Conversely, as electrodynamics and neutral forcing play a significant role as well in its dynamics, the F_2 layer behaviour cannot be modeled by simple functions of χ and solar activity. Hence, in this case an empirical correction derived from the collected data has been proposed, in order to take into account the decreased solar irradiance during the eclipse modeled by the *SOF*. This means that the results obtained are strictly valid for the specific case study, and they cannot be extended to other similar events.

Since the solar eclipse occurred during the recovery phase of the St. Patrick geomagnetic storm, a correction has been applied to the normally expected f_oF_2 monthly median values, in order to take into account the storm effects separately to those produced by the solar eclipse. Indeed, the St. Patrick geomagnetic storm was one of the strongest geomagnetic storm of the current solar cycle, being classified as a G4-class (i.e. severe) event, associated to a maximum K_p index equal to 8. It started at approximately 04:45 UT of March 17, 2015 when a fast-moving CME hit the Earth's Magnetic Field (Cherniak et al., 2015). As can be inferred from the D_{st} index values of the second half of March 2015 shown in Fig. 5.8 (source: http://wdc.kugi.kyoto-u.ac.jp), the maximum intensity of the storm was reached at around 23:00 UT of March 17, 2015, and was characterized by the minimum value of D_{st} index of -223 nT.

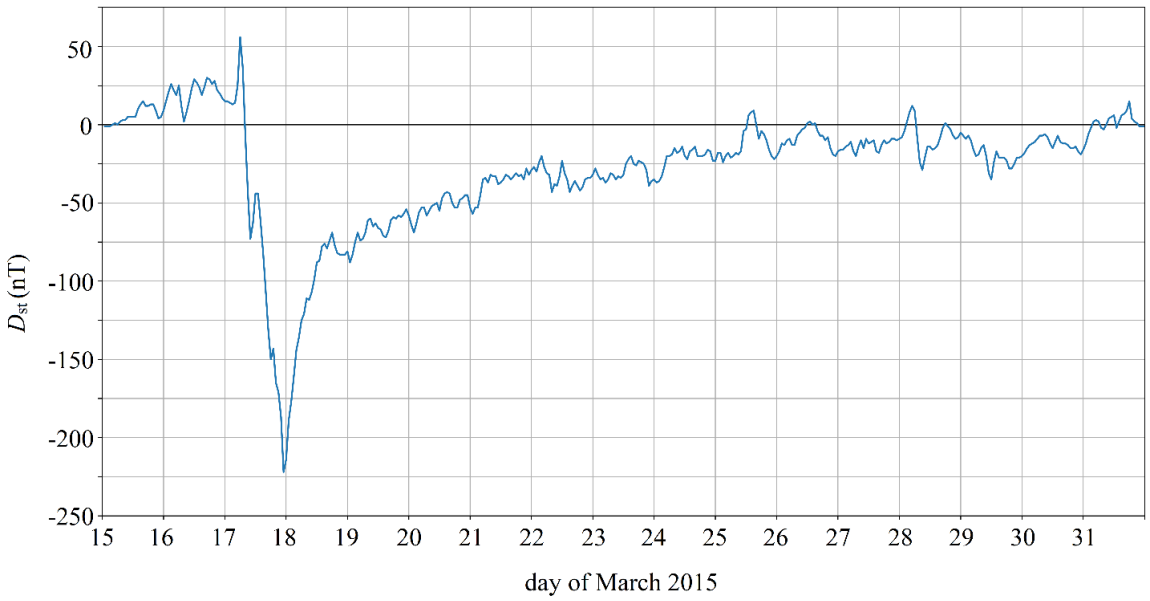

Fig. 5.8. D_{st} index recorded from March 15 to March 31, 2015.

As highlighted by Pietrella et al. (2016), the geomagnetic storm had a strong influence on f_oF_2, resulting in significant deviations of the observed values from the corresponding monthly median ones, considered as representative of a quiet state of the ionosphere. In particular, from about 18:00 UT of March 19 (the day before the solar eclipse), until about 16:00 UT of March 20 (the day of the solar eclipse), a negative phase was highlighted at the ionospheric stations of Rome, Gibilmanna, and San Vito, f_oF_2 measurements lying below the predicted monthly median trend. Thus, the solar eclipse event occurred during this negative phase, when K_p index reached values of 5-, indicating a moderate geomagnetic activity.

In order to reduce the geomagnetic storm effects, reference values of f_oF_2 have been obtained reducing by a constant factor the values given by IRI-CCIR model. The constant factor has been calculated so as to minimize the *RMSD*s between the observed values and those modeled, considering the ionograms recorded before and after the eclipse at Rome, Gibilmanna, and San Vito every 15 minutes from 18:00 UT of March 19, 2015 until 16:00 UT of March 20, 2015. As can be inferred for instance from the *SOF* temporal evolution reported in Fig. 5.1, the data excluded are those recorded from 08.30 UT to 10.30 UT at Rome and Gibilmanna, and from 08.45 UT to 10.30 UT at San Vito. The reduction factor obtained has been equal to 0.79, so that the corresponding reduced f_oF_2 values have been calculated following:

$$f_oF_{2[mod]} = 0.79 \cdot f_oF_{2[IRI\text{-}CCIR]} \quad (5.7)$$

where $f_oF_{2[IRI\text{-}CCIR]}$ are monthly median f_oF_2 values calculated by the IRI-CCIR model in accordance to (4.8) and (4.9).
Once the negative storm effect on f_oF_2 is introduced through the correction (5.7), the differences $d=f_oF_{2[obs]}-f_oF_{2[mod]}$ at the three stations have been evaluated during the eclipse, and are reported in Fig. 5.9 as a function of the *SOF*. Indeed, as discussed below, a clear further negative effect has been observed on f_oF_2 values during the eclipse window. As observed also by other authors studying the same event over Europe (Pietrella et al., 2016; Chukwuma and Adekoya, 2016; Hoque et al., 2016), this effect can be recognized as a clear signature of the solar eclipse-induced variation in the local solar radiation. This means that deviations on f_oF_2 values observed during the eclipse window can be reasonably related to the *SOF*.

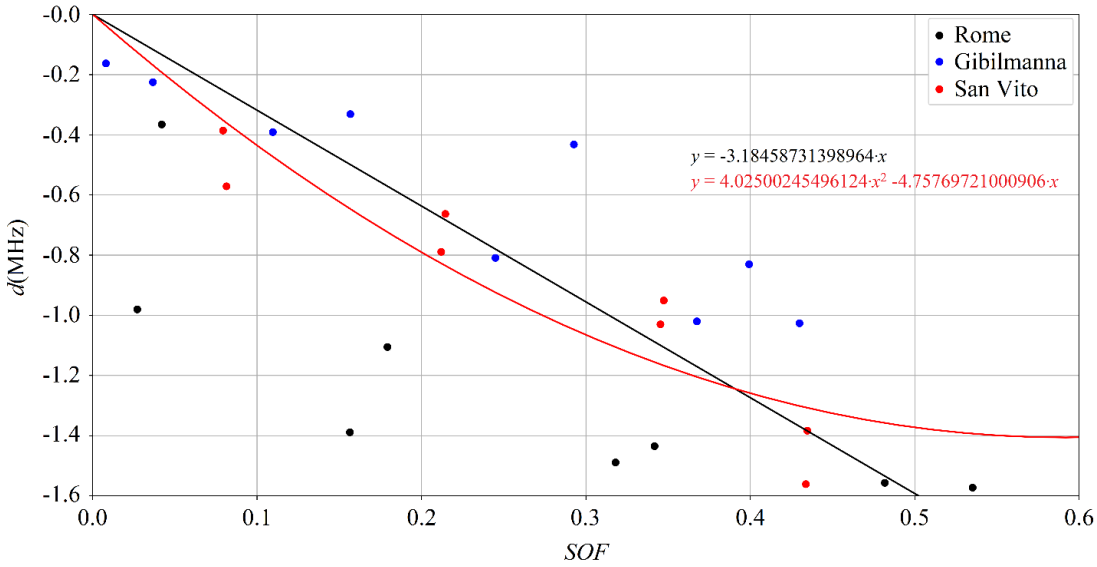

Fig. 5.9. Plot of *d* values computed at the ionospheric stations of Rome (41.8° N, 12.5° E) (black dots), Gibilmanna (37.9° N, 14.0° E) (blue dots), and San Vito dei Normanni (40.6° N, 18.0° E) (red dots), as a function of *SOF* during the eclipse of March 20, 2015. The linear and the quadratic regression of the data are also shown with a black and red lines, respectively.

A data fit has then been applied to obtain $d=d(SOF)$. As will be shown in Section 5.5, in order to introduce the eclipse effects in RATIM for testing its adaptability in such condition, an evaluation of the average effect of the solar eclipse under the considered region is needed. For this reason, all the stations have been taken into account simultaneously, despite the big data spread. Linear and quadratic regressions have been tested, obtaining the analytic functions drawn in Fig. 5.9, associated to *RMSD*s with data equal to 0.35 MHz and 0.33 MHz, respectively. Hence, the best relationship obtained among those tested is:

$$d(SOF) = 4.03 \cdot SOF^2 - 4.76 \cdot SOF, \quad (5.8)$$

where the curve transit for the (0, 0) point has been imposed for physical reasons, as no deviations are expected when the eclipse is absent (i.e. for $SOF=0$). In order to take into account the effect of the eclipse on f_oF_2 estimation, the following formula has been thus proposed:

$$f_oF_{2[eclipse]} = f_oF_{2[mod]} + d(SOF). \quad (5.9)$$

This formulation makes it possible to model f_oF_2 over a region where *SOF* values are available, applying a correction dependent only by the *SOF*, obtained from data over the considered region and hence representing the average effect of the sudden obscuration of the Sun over the same area.
In Fig. 5.10(a)-(c) are shown the same data reported in Fig. 5.9, in terms of *d* versus *SOF* values obtained at the three stations separately. For each reported datum, the time for which the computation has been performed is also shown, in order to highlight different phases associated to the *SOF* trend over each station. Fig. 5.11(a)-(c), instead, shows the trends as a function of time of $f_oF_{2[obs]}$, $f_oF_{2[IRI\text{-}CCIR]}$, $f_oF_{2[mod]}$, and $f_oF_{2[eclipse]}$ at the ionospheric stations of Rome, Gibilmanna, and San Vito, along with the evolution in time of the *SOF* at each station, with the time of the maximum *SOF* value highlighted with a dashed vertical line. Finally, Fig. 5.12(a)-(i) shows the $f_oF_{2[eclipse]}$ maps obtained every 15 minutes from 08:30 UT to 10:30 UT in the region of latitude from 36.0° N to 47.5° N and longitude from 6.0° E to 19.0° E. These maps have been obtained applying the relationship (5.9) to the entire geographical area, using the *SOF* maps calculated in Section 5.2, and the monthly median f_oF_2 values obtained by (4.8) and (4.9).

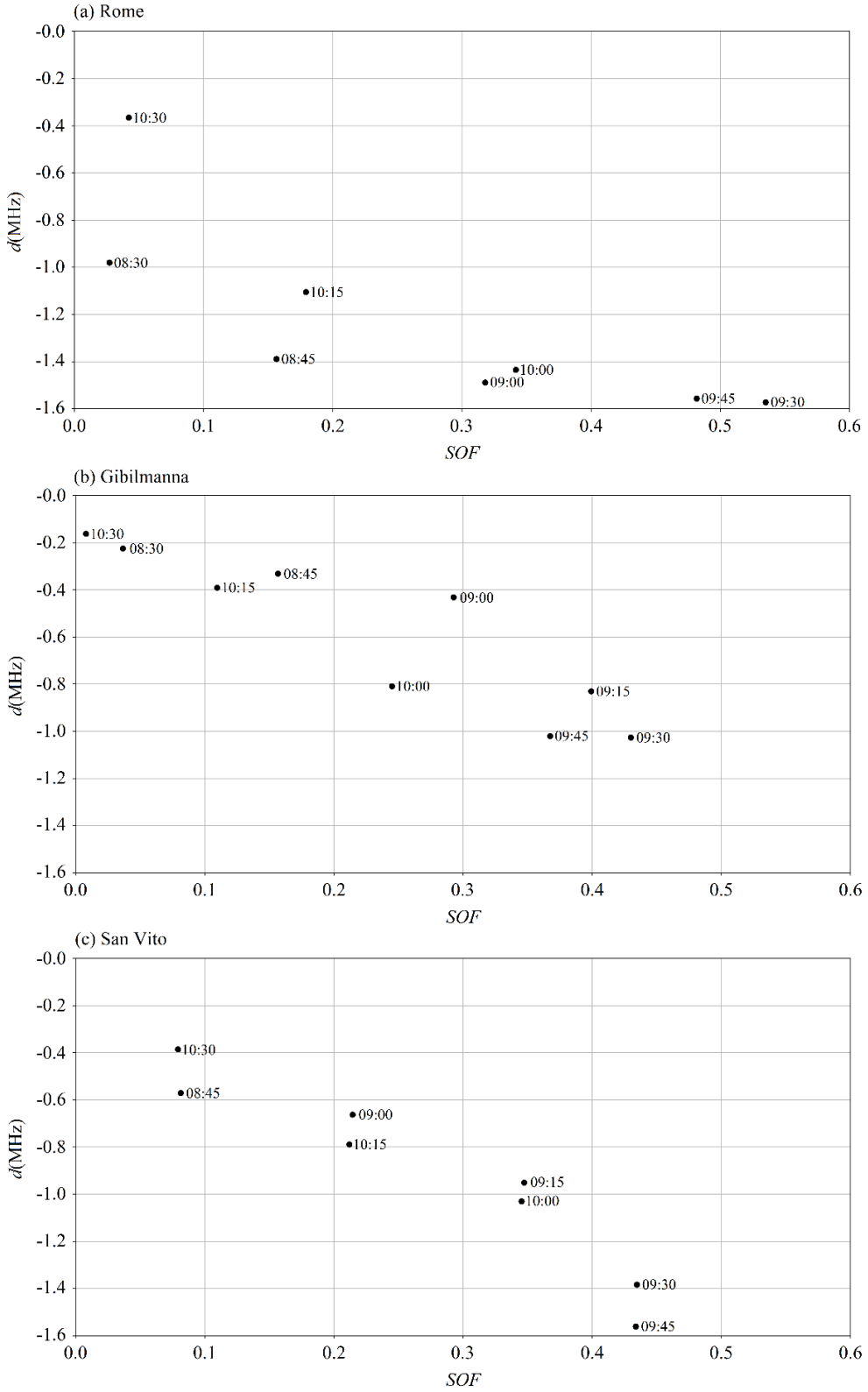

Fig. 5.10. Plot of *d* values computed at the ionospheric stations of Rome (41.8º N, 12.5 º E) (a), Gibilmanna (37.9º N, 14.0º E) (b), and San Vito dei Normanni (40.6º N, 18.0º E) (c) separately, as a function of *SOF* during the eclipse of March 20, 2015. For each reported datum is also shown the time for which the computation has been performed.

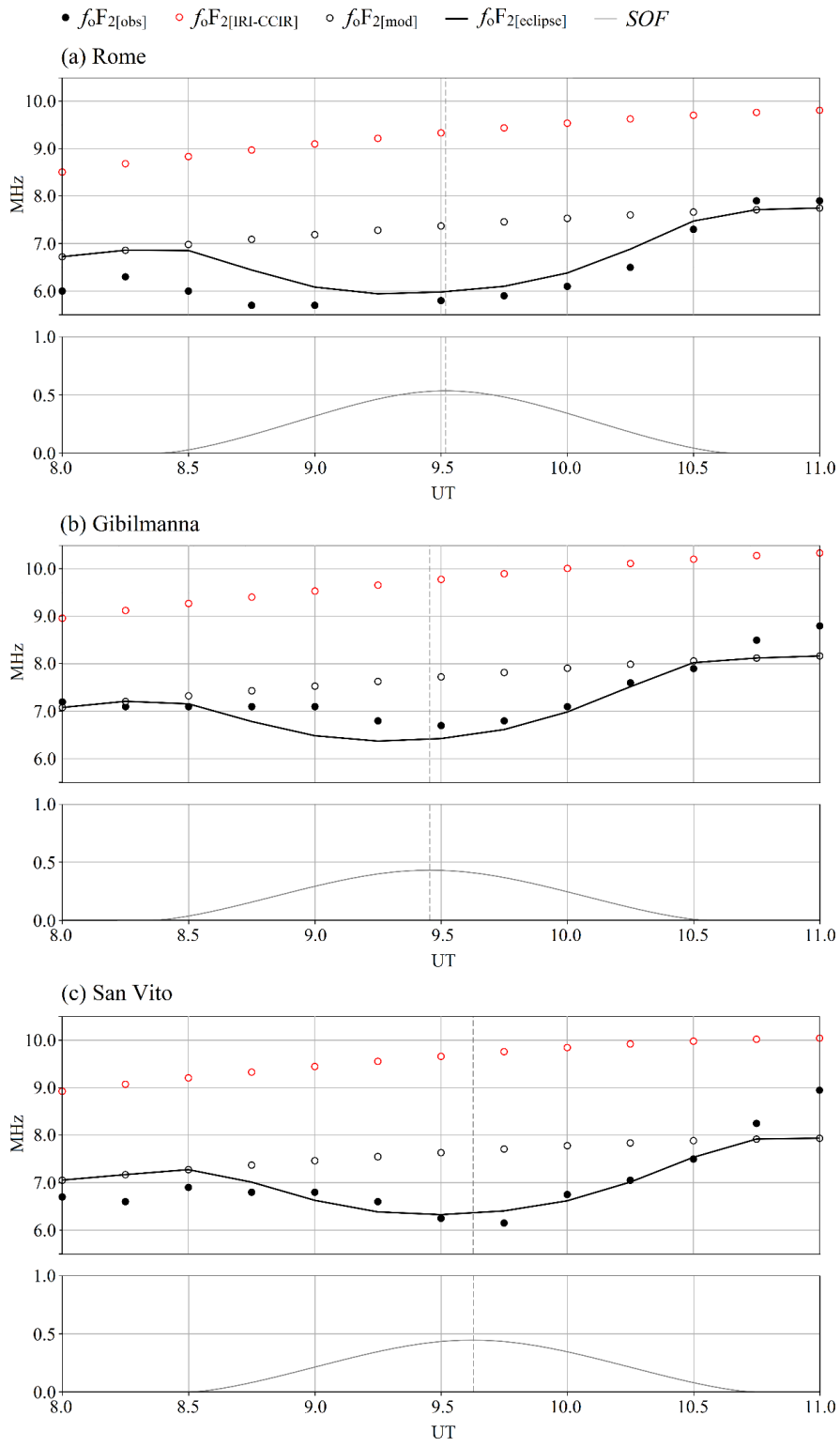

Fig. 5.11. Trends as a function of time from 08:00 UT to 11:00 UT of $f_oF_{2[obs]}$, $f_oF_{2[IRI\text{-}CCIR]}$, $f_oF_{2[mod]}$, and $f_oF_{2[eclipse]}$ at the ionospheric stations of Rome (41.8º N, 12.5º E) (a), Gibilmanna (37.9º N, 14.0º E) (b), and San Vito dei Normanni (40.6º N, 18.0º E) (c) during the eclipse of March 20, 2015. The trends are related to the evolution in time of the *SOF* at each station, and the time of the maximum *SOF* value is highlighted with a dashed vertical line.

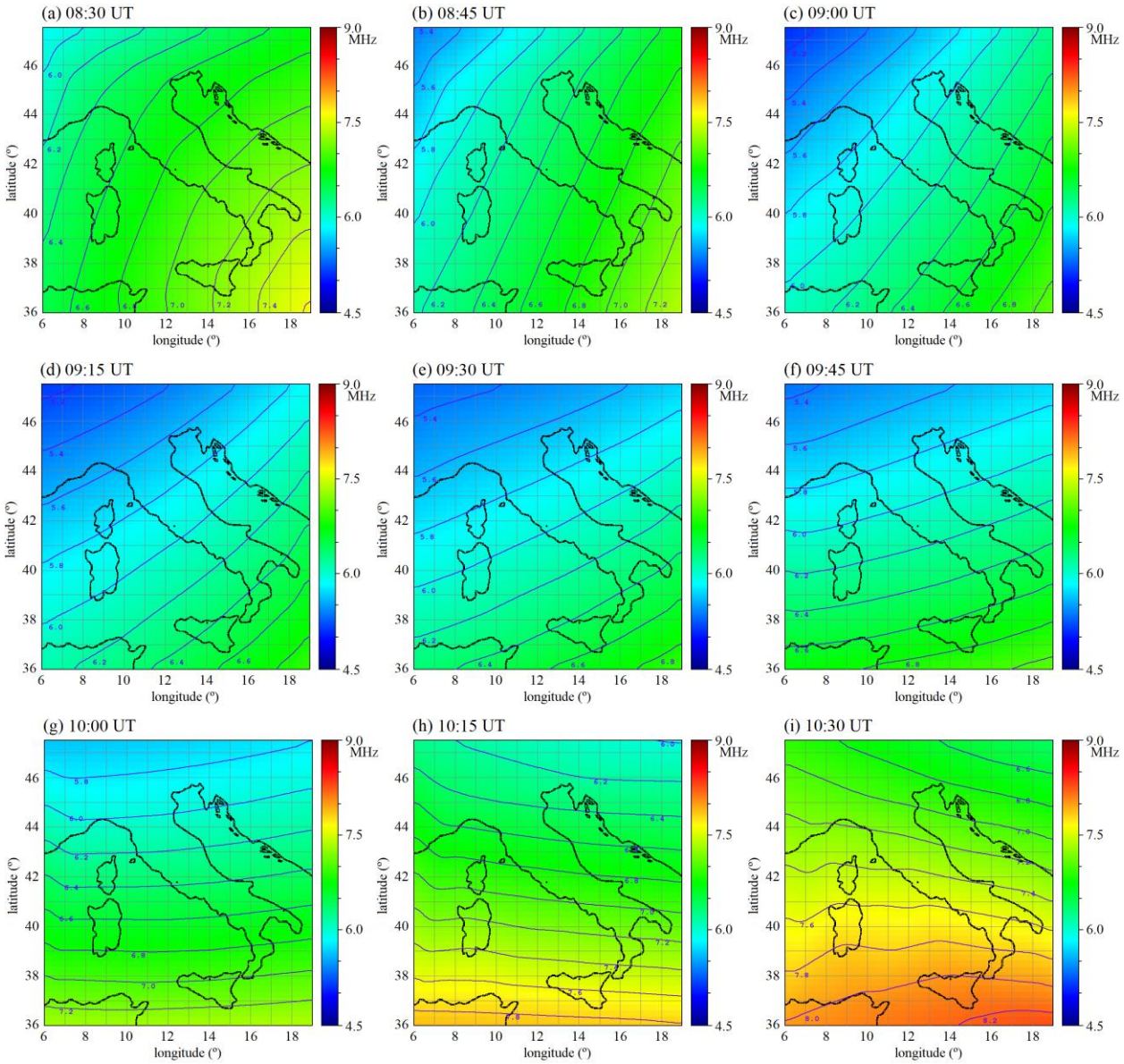

Fig. 5.12. Maps of $f_oF_{2[eclipse]}$ in the region of latitude from 36.0º N to 47.5º N and longitude from 6.0º E to 19.0º E, calculated every 15 minutes from 08:30 UT to 10:30 UT during the eclipse of March 20, 2015. These maps have been obtained using the monthly median f_oF_2 values mapping procedure performed by the IRI model.

The analysis of the Figs. 10(a)-(c) and 11(a)-(c) highlights the more complex behaviour of f_oF_2 than those observed for the critical frequencies of the underlying layers, as a consequence to the higher dynamics of the F_2 region, aggravated by the St. Patrick geomagnetic storm. The $f_oF_{2[mod]}$ trends in Fig. 5.11(a)-(c) represent the values modeled considering the negative effect of the storm. As already mentioned, the $f_oF_{2[obs]}$ trends in the same figure show a further negative effect related to the solar radiation decrease during the sun obscuration.

However, it can be also noticed that $f_oF_{2[obs]}$ trends are not exactly in counter-phase respect to the *SOF* curves at the relative locations, being also much less symmetric. In particular, the minimum value of f_oF_2 turned out to be in advance respect to the *SOF* maximum at Rome (Fig. 5.11(a)), while approximately coincides with the maximum *SOF* at Gibilmanna and San Vito (Fig. 5.11(b)-(c)). Hence, the predicted delay in the response of the F_2 region to the eclipse has been not observed in this study over any ionospheric

station where measurements are available. This may be explained as an effect of the St. Patrick magnetic storm, which generated dynamic forces such as thermospheric winds and electric fields.
The anomalous minimum observed at Rome before the maximum obscuration time is unclear. It could be due to dynamic effects related the transit of a TID over Rome at about 9 UT. Gravity waves (GW) propagation triggered by the strong thermal gradient associated to the solar eclipse have been already observed both at Rome and Gibilmanna between 8 and 9 UT by Pezzopane et al. (2015). Moreover, the analysis of the ionograms recorded at the three ionospheric stations reveals the transit of such disturbance above each of them, resulting in different features in the shape of the ionograms themselves. A better development of the F_1 cusp, which could be considered as a possible TID effect (Yuan et al., 2009), is indeed evident on each series of ionograms. Hence, strong modifications have been induced in the electron density at the F_2 heights from the TID transit. These effects are much more relevant over Rome, as confirmed by the ionogram recorded at 09:00 UT, which results to be heavily stretched, as a consequence of the TID transit, which therefore could be responsible of the anomalous minimum observed at that time.
However, the reason for the different general behaviour of the ionospheric station of Rome remains not fully explained, although the comparison of the $f_oF_{2[mod]}$ values at the three stations shows a stronger effect of the storm at Rome, not related to the eclipse condition. Another difference consists in the inverse hysteresis behaviour shown in Fig. 5.10(a)-(c), whose reason is still unclear. The hysteresis behaviour itself should be further investigated, in order to understand the possible reason of such asymmetry.
Fig. 5.11(a)-(c) shows also the $f_oF_{2[eclipse]}$ trends at the ionospheric stations of Rome, Gibilmanna, and San Vito, computed through (5.9). This is an attempt to model the eclipse effect on f_oF_2 taking into account the variation of the *SOF* over the Italian area. From the results shown, it can be seen that the $f_oF_{2[eclipse]}$ curve trends at the three stations follow the trends of the $f_oF_{2[obs]}$ values, particularly during the eclipse recovery phase, even though the deviations obtained when observations are available, are generally not negligible. The *RMSD*s obtained during the eclipse window confirm a better agreement of the $f_oF_{2[eclipse]}$ values to observations than $f_oF_{2[mod]}$ ones. Indeed, they decrease from 1.29 MHz to 0.47 MHz at Rome, from 0.66 MHz to 0.30 MHz at Gibilmanna, and from 0.99 MHz to 0.16 MHz at San Vito, when correction (5.9) is introduced. Moreover, it can be noticed that even the $f_oF_{2[eclipse]}$ curve trends are not exactly in counter-phase respect to the relative *SOF* curves, but in this case the minimums are always in advance respect to the *SOF* maximums (not only over Rome). It is worth noting also that in this case, the isolines in the $f_oF_{2[eclipse]}$ maps shown in Fig. 5.12(a)-(i) seem to show a lower agreement to the shape of the *SOF* isolines reported in Fig. 5.2(a)-(i). This behaviour is expected, as critical frequency of the F_2 layer does not suffer a strong solar control.

5.5 RATIM behaviour during the solar eclipse

The behavior of RATIM (Sabbagh et al., 2016) has been then tested during the solar eclipse, when the *SOF* corrections (5.4), (5.6), and (5.9) for the critical frequencies evaluation have been introduced. As described in the previous chapter, RATIM ingests ionosonde data by minimizing the *RMSD*s between the observed and modeled values of $f_p(h)$ profiles obtained at the points where the observations are available. This minimization procedure is used to set the values of some free parameters that characterize the model, which are then applied over the specified area. In this study, the model has been applied over the region of latitude from 36.0° N to 47.5° N and longitude from 6.0° E to 19.0° E, using data from the ionospheric stations of Rome and Gibilmanna for adapting, and independent data at San Vito dei Normanni for testing.
The model input $f_p(h)$ profiles at Rome and Gibilmanna have been obtained from Autoscala (Scotto and Pezzopane, 2002; Pezzopane and Scotto, 2005) using AIP (Scotto, 2009) as part of the vertical ionogram automatic interpretation process. The Rome and Gibilmanna ionograms have been recorded by the AIS-INGV ionosonde (Zuccheretti et al., 2003). The formulations (5.4) and (5.6) have been introduced into Autoscala in order to model f_oE values and set the f_oF_1 search procedure in the ionograms, while f_oF_2 values are autoscaled using an image recognition technique. This allows Autoscala to generate the profiles as realistic as possible in eclipse conditions. The San Vito ionograms have been recorded by the digisonde

(Haines, 1994) and inverted by POLAN (Titheridge, 1959, 1985, 1988), using manually scaled f_oF_1 and f_oF_2 values. f_oE POLAN input values have been modeled by (5.4), as it has not been possible to clearly identify the cusp of the E region in the ionograms, as already mentioned in Section 5.2. It is worth noting that in this study they have been used data from the AIS-Autoscala system at Rome, instead of data from the digisonde-ARTIST system, as done in the first RATIM test described in Section 4.4. Indeed, the INGV ionospheric station of Rome manages both systems simultaneously. Hence, in this study it has been decided to adapt the model to data from the same system (i.e. AIS-Autoscala system at Rome and Gibilmanna), performing the test using data from a different one (i.e. digisonde-POLAN system at San Vito). This permits to assess the RATIM performance in different situations, as regard the sources of its input data.
The *SOF* corrections (5.4), (5.6), and (5.9) for the critical frequency evaluations have been introduced into the model in order to let it better follow the eclipse effects. Indeed, despite being able to fit the profiles obtained from measurements even during the solar eclipse, the RATIM original version is unable to describe the small-scale eclipse effects. This is because RATIM adapts to profiles obtained over distances of the order to hundreds of kilometers, so that features over shorter distances cannot be adequately described. This is clear from the comparison between Fig. 5.13(a)-(c) and Fig 5.14(a)-(c), showing f_p maps at the fixed heights of 110 km, 180 km, and 250 km obtained at 09:45 UT by RATIM, respectively introducing or not the corrective formulations (5.4), (5.6), and (5.9). As can be seen, f_p maps in Fig. 5.13(a)-(c) follow the eclipse effect as described by the *SOF* map in Fig. 5.2(f), while the maps in Fig. 5.13(a)-(c) do not show a clear influence of the solar eclipse.

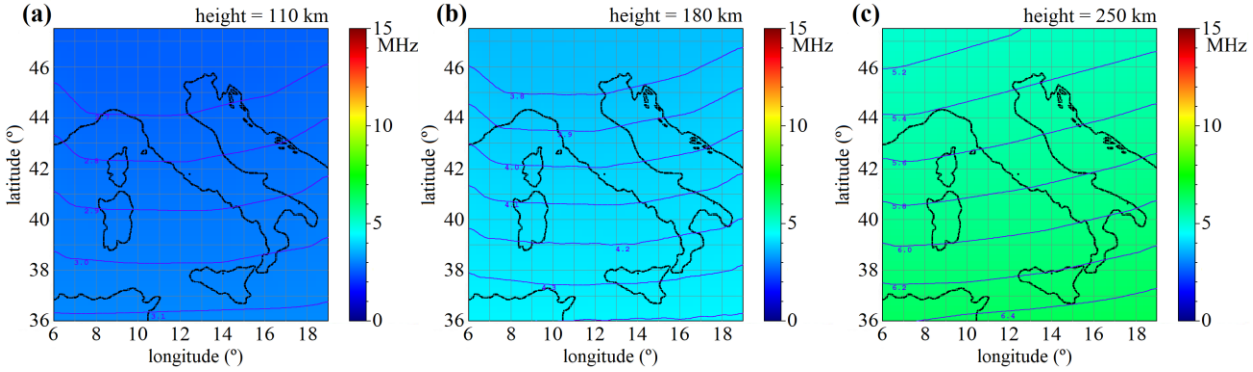

Fig. 5.13. Maps of $f_p(\varphi,\lambda)$ for h=110 km (a), h=180 km (b), and h=250 km (c), in the region of latitude from 36.0° N to 47.5° N and longitude from 6.0° E to 19.0° E, generated for March 20, 2015 at 09:45 UT. These maps have been obtained by RATIM, when corrective formulations for critical frequencies evaluation during the solar eclipse have been introduced.

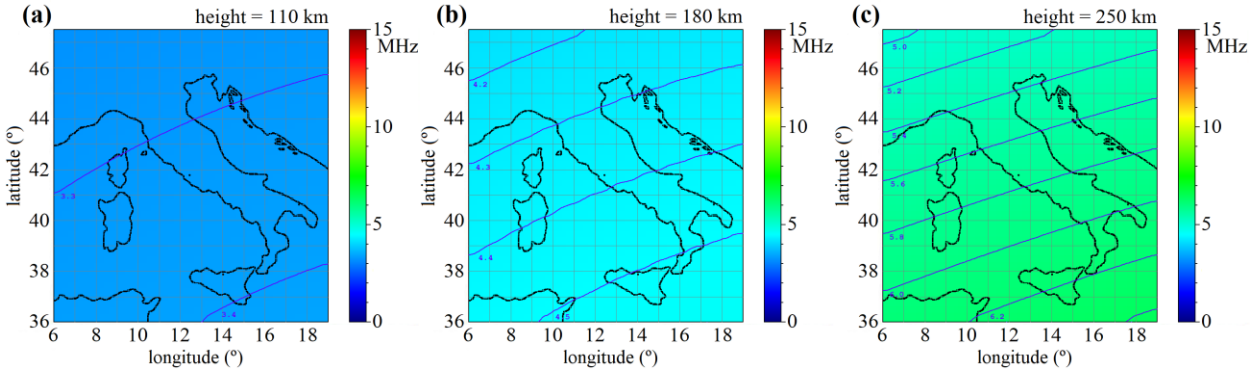

Fig. 5.14. Maps of $f_p(\varphi,\lambda)$ for h=110 km (a), h=180 km (b), and h=250 km (c), in the region of latitude from 36.0° N to 47.5° N and longitude from 6.0° E to 19.0° E, generated for March 20, 2015 at 09:45 UT. These maps have been obtained by RATIM, without the introduction of the corrective formulations for critical frequencies evaluation during the solar eclipse.

Fig. 5.15(a)-(i) shows the f_oF_2 maps obtained every 15 minutes for the specified region using the procedure described above. It is noteworthy that the shapes of the f_oF_2 isolines in Fig. 5.15(a)-(i) are the same as the corresponding isolines in Fig. 5.12(a)-(i), since the f_oF_2 values in the two cases are only shifted by a constant factor. Panels (c) and (g) in Fig. 15 show cases in which the model has adapted with $\Delta f_oF_2=0$.

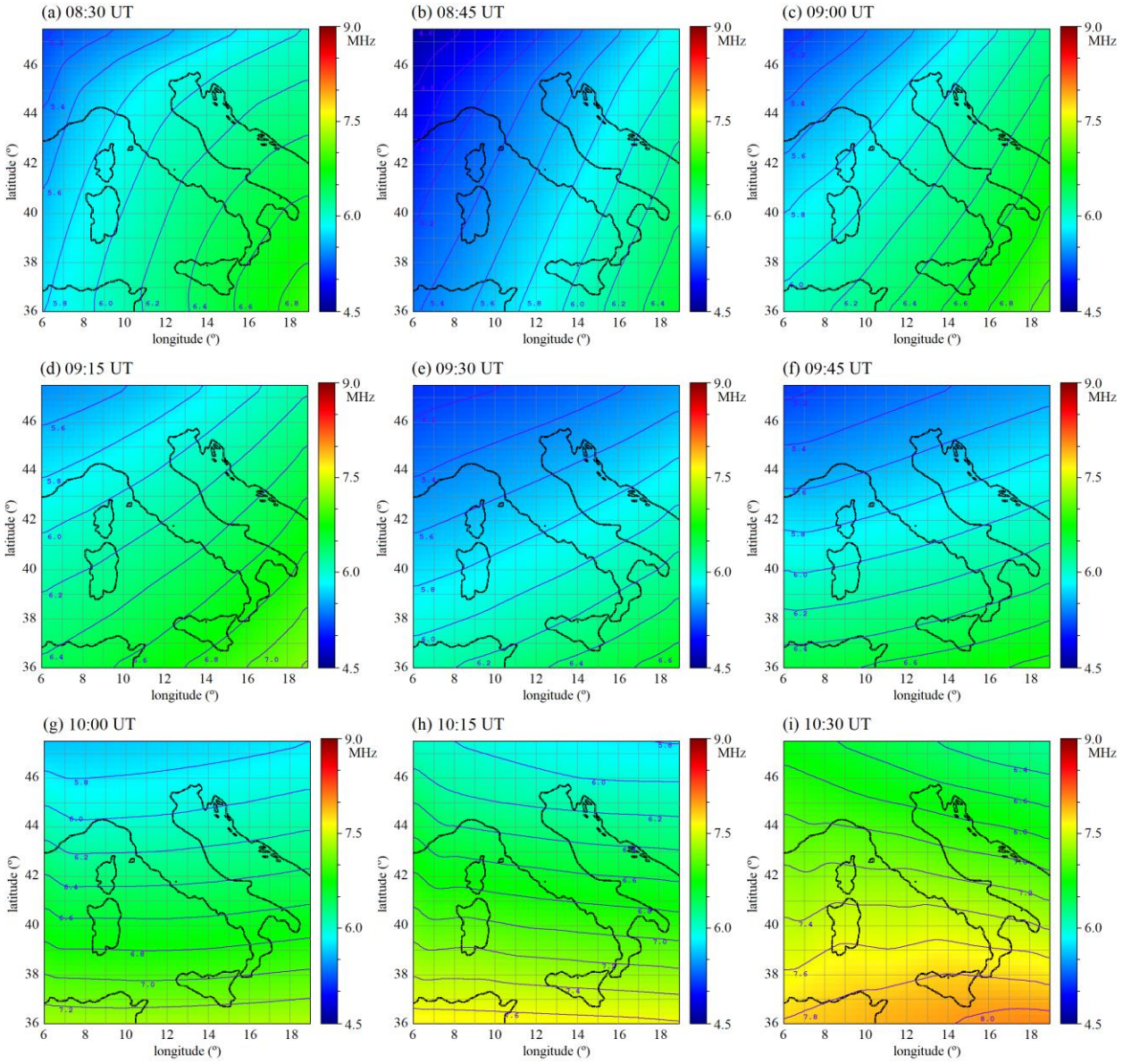

Fig. 5.15. Maps of f_oF_2 in the region of latitude from 36.0° N to 47.5° N and longitude from 6.0° E to 19.0° E, calculated every 15 minutes from 08:30 UT to 10:30 UT during the eclipse of March 20, 2015. These maps have been obtained by RATIM, when corrective formulations for critical frequencies evaluation during the solar eclipse have been introduced.

RATIM performance in terms of adaptability and accuracy have been evaluated following the method described in Section 4.4. The results obtained both when all available $f_p(h)$ and where only validated data are used, are reported in Tab. 5.1. For comparison, the same results obtained when the corrective formulations (5.4), (5.6), and (5.9) have not been introduced in the model, are reported in Tab. 5.2.

	# cases	# adapted	% adapted	adapting ⟨*RMSD*⟩ (MHz)	test ⟨*RMSD*⟩ (MHz)
All available data	9	9	100	0.30	0.36
Only validated data	4	4	100	0.32	0.31

Tab. 5.1. Percentages of success of the adjustment procedure (3rd column), adapting mean *RMSD*s (4h coloumn), and test mean *RMSD*s (5th coloumn), obtained by RATIM, when corrective formulations for critical frequencies evaluation during the solar eclipse have been introduced. The total number of the considered cases (1st column), and the number of cases in which the adjustment procedure has been effective (2rd column) are also reported.

	# cases	# adapted	% adapted	adapting ⟨*RMSD*⟩ (MHz)	test ⟨*RMSD*⟩ (MHz)
All available data	9	9	100	0.32	0.35
Only validated data	4	4	100	0.34	0.30

Tab. 5.2. Percentages of success of the adjustment procedure (3rd column), adapting mean *RMSD*s (4h coloumn), and test mean *RMSD*s (5th coloumn), obtained by RATIM, without the introduction of the corrective formulations for critical frequencies evaluation during the solar eclipse. The total number of the considered cases (1st column), and the number of cases in which the adjustment procedure has been effective (2rd column) are also reported.

As can be clearly seen, RATIM confirms his high adaptability even during the solar eclipse, since it has been able to adapt to actual conditions in all cases. Moreover, the adapting and the test *RMSD*s values obtained in such conditions are in close agreement with those reported in Section 4.4, being in some cases even lower, proving the good degree of adaptability and the good accuracy already shown. Furthermore, the fact that the test *RMSD* values decrease when erroneous input data are discarded, can be considered as a further confirmation that they affect the model's performances in terms of accuracy.
Referring to the results reported in Tabs. 5.1 and 5.2, it seems that RATIM performance is not influenced by the introduction of the corrective formulations (5.4), (5.6), and (5.9). As regards the accuracy, it could seem an unexpected result, as the new formulation for the critical frequencies evaluation during the solar eclipse are expected to work better than monthly median models. Indeed, although the f_oF_2 values are adjusted applying adapting Δf_oF_2, they usually result in better agreement to observations in the case (5.9) is applied. This is confirmed by the *RMSD* obtained between f_oF_2 values modeled by RATIM and manual scaled at the test station, as it decreases from 0.36 MHz to 0.27 MHz when the new formulation is introduced in RATIM.
Nevertheless, it should be noted that the shape discrepancies between different $f_p(h)$ are affected also by other factors, whose weight can even be higher when critical frequencies are in better agreement. These factors include differences in the peak heights of the different layers, and in the way POLAN and RATIM model the E valley. Indeed, as radio waves transmitted upward cannot be reflected in the valley region, its shape must always be modeled, even in $f_p(h)$ obtained by the ionogram inversion.
It should be noted here that the POLAN $f_p(h)$ at the test station have been generated using a simplified version of the software, with a "no-valley" option. This is quite consistent to the corresponding $f_p(h)$ modeled by ARTIST, which show very small E valleys. Conversely, the $f_p(h)$ modeled by RATIM usually show quite wide valleys, in the way Autoscala does. This is particularly true when RATIM adapts to $f_p(h)$ generated by Autoscala, as in the case of this study. This results in significant discrepancies between POLAN and RATIM modeled E regions.

It should be highlighted here that the most meaningful result obtained from this study is the high adaptability RATIM has shown even during solar eclipse condition, as the main concern is to obtain the ability to adapt to any ionospheric condition. Moreover, the introduction of the corrections (5.4), (5.6), and (5.9) for the critical frequencies modeling during the solar eclipse enables RATIM to follow its small-scale effects on the ionosphere, giving a more realistic representation of the ionosphere on regional scale. As shown in Chapter 7, an oblique ionospheric radio-sounding data assimilation procedure is proposed to furtherly improve RATIM performance. A preliminary study is thus presented, in order to assess RATIM behaviour when autoscaled MUF values are ingested, making use of a simplified ionospheric ray-tracing algorithm.

References

[1] Eccles W., 1919. Radio-Telegraphic Investigations in Connection with the solar Eclipse of May 29. Nature, 126–127.

[2] Gledhill, J.A., 1959a. The effects of a solar on a stratified ionosphere. J. Atmos. Terr. Phys. 16 (3-4), 360-366.

[3] Gledhill, J.A., 1959b. The behaviour of the ionosphere over Cape-Town and Johannesburg during the annular solar eclipse of 25 December 1954. J. Atmos. Terr. Phys. 16 (3-4), 367–375.

[4] Beynon, W. J.G., 1955. Solar eclipses and the ionosphere. Nature 176 (4490), 947–948.

[5] McLeish, C. W., 1948. Solar Eclipse observations of the ionosphere. Can. J. Res., 26 a(3): 137–144, http://dx.doi.org/10.1139/cjr48a-014.

[6] Minnis, C. M., 1954. The ionosphere during the solar eclipse of February 25, 1952. Nature 174 (4442), 1137-1138.

[7] Minnis, C. M., 1956. The response of the ionosphere to the solar eclipse of 30 June 1954 in Great-Britain. J. Atmos. Terr. Phys. 9 (4), 201–209.

[8] Bramley, E. N., 1956. Tilts in the ionosphere during the solar eclipse of 30 June 1954. J. Atmos. Terr.Phys. 8 (1-2), 98–104.

[9] Bates, D.R., McDowell, M. R. C., 1957. Recombination in the ionosphere during an eclipse. J. Atmos. Terr. Phys. 10 (2), 96–102.

[10] Stanislawska, I., Gulyaeva, T.L., Altadil, D., Bencze, P., Juchnikowski, G., Korenkov, Y.N., Sole, G., Zbyszynski, Z., 2001. Instantaneous mapping of ionospheric characteristics using 5-minute measurements for the day of the total solar eclipse of 11 August 1999. Phys. Chem. Earth Pt C 26 (5), 335–339, http://dx.doi.org/10.1016/S1464-1917(01)00009-5.

[11] Le, H., Liu, L., Yue, X., Wan, W., 2008. The ionospheric responses to the 11 August 1999 solar eclipse: observations and modeling. Ann. Geophys. 26 (1), 107–116.

[12] Farges, T., Jodogne, J.C., Bamford, R., Le Roux, Y., Gauthier, F., Vila, P.M., Altadill, D., Sole, J.G., Miro, G., 2001. Disturbances of the western European ionosphere during the total solar eclipse of 11 August 1999 measured by a wide ionosonde and radar network. J. Atmos. Sol.-Terr. Phys. 63 (9), 915–924, http://dx.doi.org/10.1016/S1364-6826(00)00195-4.

[13] Altadill, D., Gauthier, F., Vila, P., Sole, J.G., Miro, G., Berranger, R., 2001. The 11.08.1999 solar eclipse and the ionosphere: a search for the distant bow-wave. J. Atmos. Sol.-Terr. Phys. 63 (9), 925–930.

[14] Jakowski, N., Stankov, S.M., Wilken, V., Borries, C., Altadill, D., Chum, J., Buresova, D., Boska, J., Sauli, P., Hruska, F., Cander, Lj.R, 2008. Ionospheric behavior over Europe during the solar eclipse of 3 October 2005. J. Atmos. Sol.-Terr. Phys. 70, 836–853.

[15] Möllmann, K. P., Vollmer, M.. 2006. Measurements and predictions of the illuminance during a solar eclipse. Eur. J. Phys. 27, 1299–1314. http://dx.doi.org/10.1088/0143-0807/27/6/004.

[16] Davies, K., 1990. Ionospheric Radio. Peter Peregrinus Ltd., London, United Kingdom.

[17] Leitinger. R., Zhang, M.L., Radicella, S.M., 2005. An improved bottomside for the ionospheric electron density model NeQuick. Ann. Geophys. 48 (3), 525–534.

[18] Choice of indices for long-term ionospheric prediction, 1999. Rec. ITU-R P.371-8.

[19] DuCharme, E. D., Petrie, L. E., Eyerig, R., 1971. A method for predicting the Fl layer critical frequency. Radio Sci. 6 (3), 369–378.

[20] DuCharme, E. D., Petrie, L. E., Eyerig, R., 1973. A method for predicting the F1 layer critical frequency based on the Zurich smoothed sunspot number. Radio Sci. 8 (10), 837–839.

[21] Scotto, C., Mosert de González, M., Radicella, S.M., Zolesi, B., 1997. On the prediction of F1ledge occurrence and critical frequency. Adv. Space Res. 20 (9), 1773-1775.

[22] Jones, W.B., Gallet, R.M., 1962. Representation of diurnal and geographic variations of ionospheric data by numerical methods. J. Res. Nat. Bureau Stand. -D. Radio Propag. 66D, 419–438.

[23] Jones, W.B., Graham, R.P., Leftin, M.D, 1969. Advances in ionospheric mapping by numerical methods. ESSA Tech. Rep. ERL 107 – ITS 75, US Government Printing Office, Washington, DC.

[24] Cherniak, I., Zakharenkova, I., Redmon, R.J., 2015. Dynamics of the high-latitude ionospheric irregularities during the 17 March 2015 St. Patrick's Day storm: Ground-based GPS measurements. Space Weather 13, 585–597, doi:10.1002/2015SW001237.

[25] Pietrella, M., Pezzopane, M., Settimi, A., 2016. Ionospheric response under the influence of the solar eclipse occurred on 20 March 2015: Importance of autoscaled data and their assimilation for obtaining a reliable modeling of the ionosphere. J. Atmos. Solar-Terrestr. Phys. 146, 49-57. http://dx.doi.org/10.1016/j.jastp.2016.05.006.

[26] Chukwuma, V.U., Adekoya, B.J., 2016. The effects of March 20 2015 solar eclipse on the F2 layer in the mid-latitude. Adv. Space Res. 58 (9), 1720-1731, https://doi.org/10.1016/j.asr.2016.06.038.

[27] Hoque, M.M., Wenzel, D., Jakowski, N., Gerzen, T., Berdermann, J., Wilken, V., Kriegel, M., Sato, H., Borries, C., Minkwitz, D., 2016. Ionospheric response over Europe during the solar eclipse of March 20, 2015. J. Space Weather Space Clim., 6, A36, DOI: 10.1051/swsc/2016032.

[28] Pezzopane, M., Pietrella, M., Pignalberi, A., Tozzi, R., 2015. 20 March 2015 solar eclipse influence on sporadic E layer. Adv. Space Res. 56 (10), 2064-2072, https://doi.org/10.1016/j.asr.2015.08.001.

[29] Yuan, Z., Ning B., Deng, X., 2009. Effects of TADs on the F region of the mid-latitude ionosphere during an intense geomagnetic storm. Adv. Space Res. 44, 1013-1018.

[30] Sabbagh, D., Scotto, C., Sgrigna, V., 2016. A regional adaptive and assimilative three-dimensional ionospheric model. Adv. Space Res. 57 (5), 1241–1257.

[31] Scotto, C., Pezzopane, M., 2002. A software for automatic scaling of foF2 and MUF (3000) F2 from ionograms. URSI XXVIIth General Assembly.

[32] Pezzopane, M., Scotto, C., 2005. The INGV software for the automatic scaling of foF2 and MUF (3000) F2 from ionograms: A performance comparison with ARTIST 4.01 from Rome data. J. Atmos. Sol.-Terr. Phys. 67 (12), 1063–1073.

[33] Scotto C., 2009. Electron density profile calculation technique for Autoscala ionogram analysis. Adv. Space Res. 44 (6), 756–766.

[34] Zuccheretti, E., Tutone, G., Sciacca, U., Bianchi, C., Arokiasamy, B. J., 2003. The new AIS-INGV digital ionosonde. Ann. Geophys. 46 (4), 647–659.

[35] Haines, D.M., 1994. A Portable Ionosonde Using Coherent Spread Spectrum Waveforms for Remote Sensing of the Ionosphere, UMLCAR.

[36] Titheridge, J. E., 1959. The calculation of real and virtual heights of reflection in the ionosphere. J. Atmos. Terr. Phys. 17, 96–109.

[37] Titheridge, J. E., 1985. Ionogram analysis with the generalised program POLAN. World Data Center A, National Academy of Sciences, 2101 Constitution Avenue, NW, Washington, D.C. 20418 USA.

[38] Titheridge, J. E., 1988. The real height analysis of ionograms: A generalized formulation. Radio Sci. 23 (5), 831–849.

6. Improvements of the Oblique Ionogram Automatic Scaling Algorithm (OIASA) performance

As already mentioned in Chapters 2 and 3, real-time ionospheric data are required for their assimilation into both physical and empirical models. Networks of ionosondes are currently routinely used to measure the characteristics of the ionosphere with global coverage, and well-established techniques make it possible to obtain them in real-time from vertical ionograms (Scotto and Pezzopane, 2008). Conversely, the interpretation of oblique ionograms is significantly more complex, and there are no well-established automatic techniques.

The main reason of such complexity is related to the paths taken by radio signals from transmitters to reach the receivers. As the obliquely propagating radio waves are continuously refracted and not just reflected, they are much more affected by horizontal gradients and variations in the ionosphere, posing significant problems for ray-tracing (Norman and Cannon, 1999). Moreover, a variety of different paths can be taken by the signals from the transmitter to the receiver, adding possible sources of signal distortion and loss. A further complication is due to the strong absorption phenomena affecting oblique soundings (Lastovicka, J., 1978; Penndorf, R., 1962; Tsunoda, R. T., 2008) especially during solar flares and PCA events at polar latitudes (MacDougall et al., 1997; Herman J. R., 1966; King G. A. M., 1970). In many cases the typical oblique ionogram traces can completely disappear during these phenomena (Frank-Kamenetsky and Troshichev, 2012; Scotto and Pezzopane, 2011).

Another reason for the lack of automatic interpretation techniques is the relatively rare use of this type of sounding, at least in a systematic way, with the consequence of less effort being dedicated to them. However, several attempts have been made in order to derive the midpoint electron density profile from oblique soundings. Gething and Maliphant(1967), for instance, suggested a double-step method in which an oblique ionogram is converted into a vertical and analyzed by means of inversion techniques developed for vertical ionograms. A further approach is to obtain the electron density profile directly from the oblique ionogram, as has been proposed by Phanivong et al. (1995). This method takes into account the presence of the EMF and is based on the inversion technique developed by Reilly and Kolesar (1989), which considers the curvature of the ionosphere and handles the ambiguity related to the presence of the valley in the electron density profile. Other attempts worth mentioning in order to obtain midpoint electron density profiles are those of Huang et al. (1996), who develop a computationally efficient technique for the inversion of oblique ionograms, following an iterative approach in a variational process.

Recently, an algorithm for the identification of trace characteristics of oblique ionograms allowing determination of the Maximum Usable Frequency (MUF) for communication between the transmitter and receiver, has been developed by Ippolito et al. (2015). Making use of an image recognition technique based on the maximum contrast method, the Oblique Ionogram Automatic Scaling Algorithm (OIASA) is also able to automatically detect and reject poor-quality ionograms. Indeed, a set of couples of empirical curves representing the typical shape of the ordinary and extraordinary oblique traces resulting from a single reflection in the F_2 region are defined, and their local correlation C with the ionogram recorded is calculated, making allowance for both the number of matched points and their amplitude. The pair of curves with the maximum C value obtained is then selected, and the MUF resulting from the specified oblique sounding can then be inferred from the vertex coordinates of the parabola modeling the ordinary trace. Only if C_{max} is larger than a fixed threshold C_t, the resulting curves are considered representative of the ionogram traces. Otherwise, the ionogram is considered to lack sufficient information and is discarded, with no MUF value provided as output.

A quality factor for the MUF values provided by OIASA has been proposed, in order to achieve improvements on their reliability (Ippolito et al., 2016). A procedure made by the combined use of OAISA and Autoscala has been used to define the quality factor Q, after performing an oblique to vertical equivalent ionogram conversion. A filtering technique based on Q values has been consequently introduced, in order to discard cases of erroneous interpretation and decrease the number of wrong MUF estimates. The

procedure has been tested in different situations, evaluating its behaviour when applied to both high-quality and poor-quality ionograms data set. When applied to high-quality data sets, the *Q*-based filtering technique can be applied with the aim to discard autoscaled MUF values out of a proper range from the corresponding manual scaled values. When applied to poor-quality data sets, instead, the procedure can be successfully used to discard further ionograms with insufficient information.

6.1 Oblique to vertical equivalent ionogram conversion

The procedure to convert an oblique ionogram into a vertical equivalent one begins with the storage of the oblique ionogram in matrix form. The number of rows m and columns n of the matrix A are defined by the following formulas:

$$m = \text{int}[(t_f - t_0)/\Delta t], \quad (6.1a)$$
$$n = \text{int}[(f_f - f_0)/\Delta f], \quad (6.1b)$$

where int stands for integer, while f_f, f_0, Δf, t_f, t_0, and Δt are, respectively, the final frequency, the initial frequency, the frequency step, the final time delay, the initial time delay, and the time delay resolution of the oblique sounding. The values t_0, t_f and Δt are fixed and depend on the design of the ionosonde. The values f_0, f_f, and Δf, are usually set in accordance with the programmed measurement campaign. Depending on the method used to the ionogram data storage in the matrix A, the element a_{ij} (with i=1, …, m and j=1, …, n) can be the actual power amplitude of the received echoes, measured in dB, or an integer ranging from 0 to 255, proportional to the latter. These values are obtained directly from the data file recorded by the instrument. Once the ionogram is stored in matrix form, different filter techniques are applied based on the level of radio frequency noise which affect the ionogram. This is peculiar to each specific data set, depending on the receiver ionosonde used, and the HF band electromagnetic noise at its location, whose origin is both natural and anthropic, the latter also due to the presence of broadcast stations nearby. The filters applied to the data used in this study are described is Section 6.3 and 6.4. Then, after the proper filter procedure has been applied, each element a_{ij} of the matrix A is converted in 0 or 1, with 1 values associated to signals considered actual ionospheric echoes.
Applying the secant law and the Martyn's equivalent path theorem (Martyn, 1935) to each frequency-virtual ray-path pair, the equivalent vertical ionogram over the ray-path midpoint is obtained. According to the geometry shown schematically in Fig. 6.1, the curvature of the Earth is also considered.

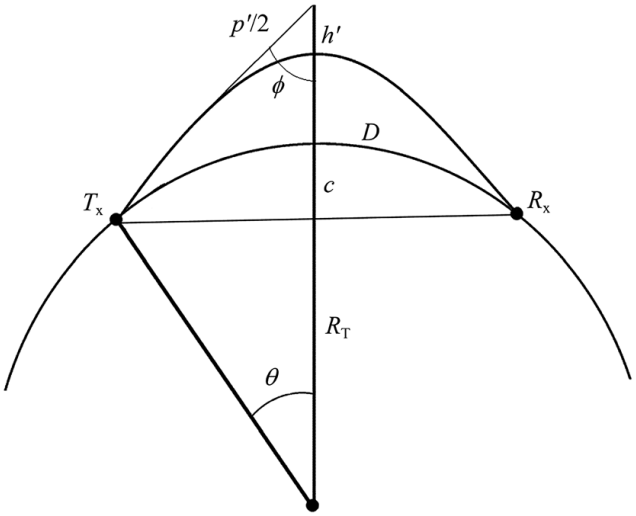

Fig.6.1. A scheme of the considered geometry for an oblique ray-path, where T_x and R_x represent the transmitter and the receiver locations, respectively. The Earth's curvature is also taken into account (Ippolito et al., 2016).

Assuming an isotropic, horizontally homogeneous, and flat ionosphere, and representing f_o and f_v as the frequencies of the radio waves reflected obliquely and vertically respectively, at the same real altitude, from the secant law we have:

$$f_v = f_o/\sec\phi, \tag{6.2}$$

where ϕ is the incidence angle of the oblique radio signal. According to the Martyn's equivalent path theorem, the virtual height h' at which f_v is reflected from the ionosphere is given by (Gething, 1969; Kol'tsov, 1969):

$$h'(f_v) = p'(f_o)/(2\sec\phi) - c, \tag{6.3}$$

where c is the h' correction for the curvature of the Earth, and, and p' is the group path of the oblique signal. Through geometric considerations we also have:

$$c = R_T \cdot (1 - \cos\theta), \tag{6.4}$$

and:

$$\sin\phi = (2R_T \cdot \sin\theta)/p'(f_o)\,, \tag{6.5}$$

where R_T is the Earth radius, and $\theta = D/(2R_T)$ is the angle at the center of the Earth between the transmitter and the midpoint locations, being D the ground range associated to the oblique radio-link. Combining the equations from (6.2) to (6.5), each oblique ionogram (f_o, $p'(f_o)$) pair can then be mapped to a new (f_v, $h'(f_v)$) pair of values, representing the points of the vertical equivalent ionogram over the ray-path midpoint.

6.2 Definition of the quality factor *Q*

A procedure for the OIASA performance improvement has been developed (Ippolito et al., 2016), making use of the definition of a quality factor for the autoscaled MUF values. As shown in Section 6.3 and 6.4, the application of this procedure to different data sets has shown good results, in terms of reduction of wrong MUF estimates, in different conditions.

The procedure combines the use of OAISA and Autoscala programs, thanks to the oblique to vertical ionogram conversion described in the previous section. The equivalent vertical ionogram resulting from the conversion of the original oblique one is stored in an RDF (Raw Data Format) file format and analyzed by Autoscala. This operation enables deriving all the ionospheric parameters over the midpoint of the oblique ray-path. Then, the critical frequency f_oF_2 given by Autoscala ($f_oF_{2[Autoscala]}$) is compared with $f_oF_{2[OIASA]}$ derived by the application of the secant law to the OIASA autoscaled MUF($MUF_{[OIASA]}$):

$$f_oF_{2[OIASA]} = MUF_{[OIASA]}/\sec\phi, \tag{6.6}$$

where $\sec\phi$ associated to each $MUF_{[OIASA]}$ value is computed making use of (6.5), with $f_o = MUF_{[OIASA]}$. It is worth noting that ϕ calculation involves $p'(MUF_{[OIASA]})$, which is scaled by OIASA along with the MUF, being both inferred from the vertex coordinates of the parabola modeling the ordinary trace.

Hence, the quality factor $Q = \Delta f_oF_2 = |f_oF_{2[Autoscala]} - f_oF_{2[OIASA]}|$ is calculated for each autoscaled MUF value. A proper filtering technique based on Q values is then applied, in order to discard cases of erroneous interpretation.

It is noteworthy that an electron density profile $N(h)$ at the midpoint of the considered radio-link can also be estimated through the described technique by Autoscala, using AIP (Scotto, 2009). Fig. 6.2(a)-(b) shows an example of high-quality oblique ionogram converted into vertical, after being properly filtered from the background noise. The results of the application of AIP are also reported.

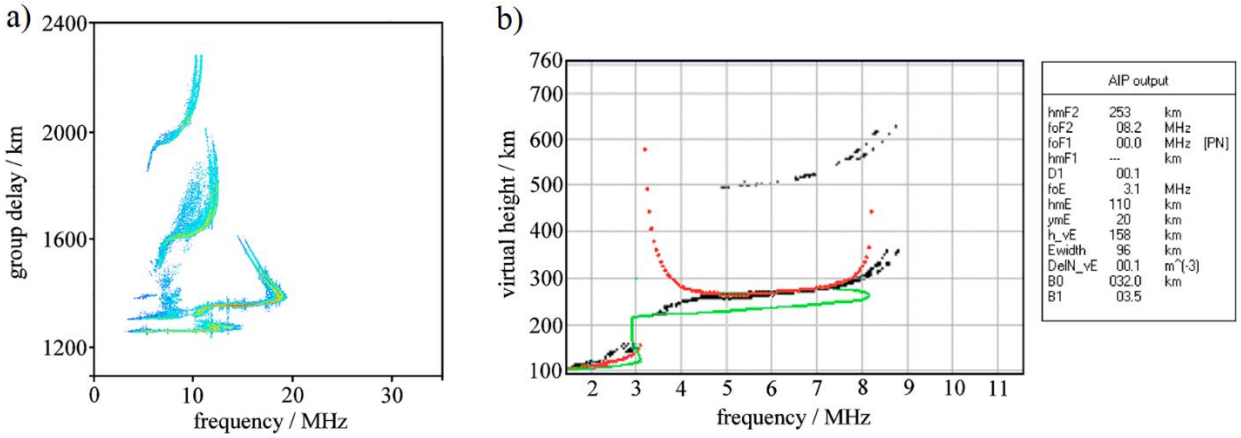

Fig.6.2. Example of a high-quality oblique ionogram (a) recorded on the 1218 km path between CUR, Australia (17.60°S; 123.82°E) and MTE, Australia (23.52°S; 133.68°E), and converted into vertical (b), after the application of a proper filtering technique to reduce the radio frequency background noise. The results of the application of Autoscala program and the Adaptive Ionospheric Profiler (AIP) are also reported in (b) (Ippolito et al., 2016).

6.3 Results on high-quality SWS ionograms recorded in Australia

The performance of the procedure described in Sections 6.1 and 6.2 has been firstly tested using a set of 384 high-quality oblique ionograms from the Australian Bureau of Meteorology's Space Weather Services (SWS) campaign of oblique soundings, performed on the 1218 km path between the ionosondes of CUR, Australia (17.60° S; 123.82° E) and MTE, Australia (23.52° S; 133.68° E), shown in Fig. 6.3.
The ionograms in the data set represent the records of April 15, and April 16, 2013. Being the quality of the oblique soundings very high (Gardiner- Garden et al., 2008), for all of them an experienced operator has been able to scale a MUF value, which has been assumed as reference. Based on the manually scaled values, the MUF values scaled by OIASA have been classified as "Accurate" if they are in the range of 0.5 MHz from the manual scaled MUF, and "Acceptable" if in the range of 1.5 MHz, in accordance with the International Union of Radio Science (URSI) standard (Piggott and Rawer, 1972). Finally, out of the range of 1.5 MHz they are considered incorrectly autoscaled.
As described in Section 6.1, each ionogram in the data set has been stored in matrix form, whose matrices elements values are integers ranging from 0 to 255, proportional to the amplitude of the received echoes. To reduce the radio frequency noise affecting the ionograms, a simple filter algorithm analyzingeach element a_{ij} of the matrices storing the ionogram information, has been applied. Since image background noise is often presented as dense sets of pixels, a defined number of pixels around the considered element a_{ij} is analyzed, and their numerical values are summed up. When this sum is greater than a fixed threshold, the element a_{ij} is assumed to be part of the noise and then deleted.
The SWS oblique ionograms have been recorded using a Digital Oblique Receiving System (DORS) on loan from the Australian Defence Science and Technology group (DST), and are available on PNG image format. The receiving echoes information is then directly extracted from the ionogram images.

Fig. 6.3. The 1218 km radio-link between the Australian SWS ionospheric stations of CUR (17.60° S; 123.82° E) and MTE (23.52° S; 133.68° E) (red line) (courtesy of Alessandro Ippolito).

The same filtering procedure has been applied to the ionograms before performing the MUF autoscaling by OIASA. An example of the results obtained can be seen in Fig. 6.4(a)-(b), in which is shown the same ionogram before and after applying such a filter algorithm, and OIASA.

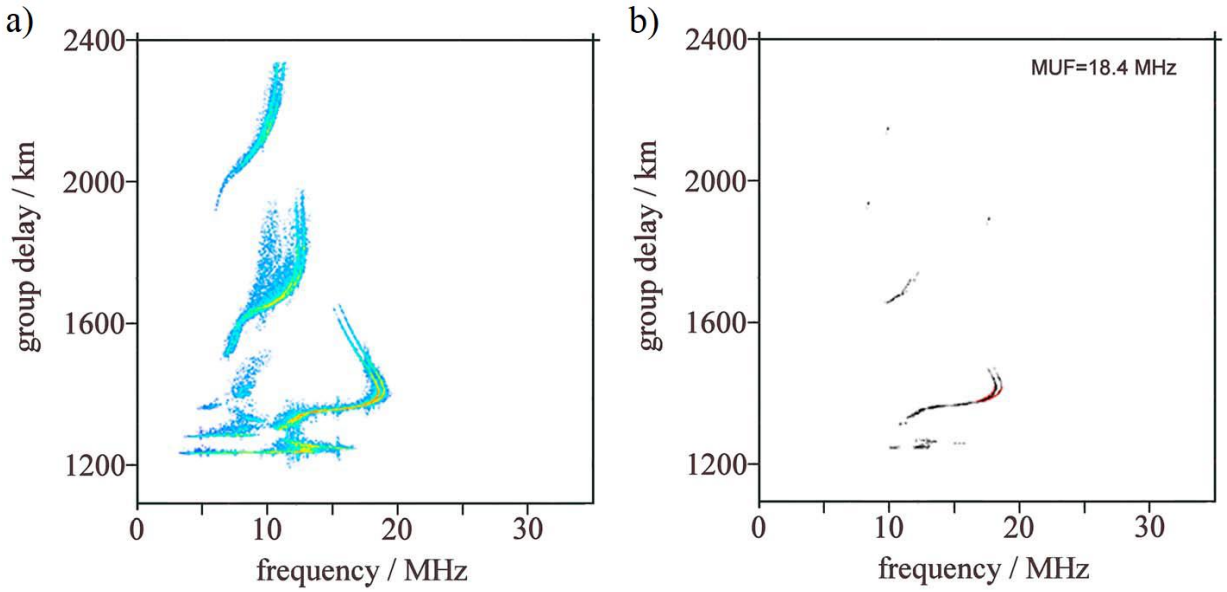

Fig.6.4. Example of an SWS ionogram in the data set before (a) and after (b) the application of the noise filter. OIASA outputs are also reported in (b), being the red curves the empirical parabola branches representing the ordinary and extraordinary oblique traces resulting from a single reflection in the F_2 region. (Ippolito et al., 2016)

The contrast threshold C_t applied by OIASA to automatically detect and reject poor-quality ionograms, has been set equal to 60, in accordance to the value chosen in Ippolito et al., 2015. In that work, the same data set using in this study was analyzed using C_t=60, after having chosen and tested this value on a different data set. As reported in Tab. 6.1(a), both an experienced operator and OIASA have been able to scale the MUF from the high-quality ionograms in the data set. Cases of accurate and acceptable autoscaled MUF values are reported in Tab. 6.1(b),

based on the comparison with the corresponding manually scaled values.

a)

	Scaled by the Software		Discarded by the Software	
	No. of Cases	(%)	No. of Cases	(%)
The operator did not scale the MUF	0	0	0	0
The operator scaled the MUF	384	100	0	0
Total	384		0	

b)

	Scaled by the Software and the Operator	
	No. of Cases	(%)
Accurate	345	89.84
Acceptable	373	97.14
Total	384	

Tab. 6.1. Scaled and discarded ionograms by both an experienced operator and OIASA, when applied to the data set of 384 high-quality oblique ionograms recorded on the Australian CUR-MTE radio-link (a). Accurate and acceptable values for OIASA application on the same data set (b). (Ippolito et al., 2016)

After being processed by OIASA and converted in vertical equivalent ionograms, the $f_oF_{2[Autoscala]}$ and $f_oF_{2[OIASA]}$ values corresponding to each ionogram in the data set, have been identified. As Autoscala has not provided an f_oF_2 value for 18 vertical ionograms no value of Q has been associated to them. Consequently, for these ionograms it has not been possible to apply the automatic rejection procedure, based on Q. Conversely, for each ionogram whose MUF autoscaled value has a corresponding Q value, a proper filtering technique has been then applied, in order to discard cases of erroneous interpretation.

As the method has been applied to a high-quality ionograms data set, the rejection procedure has been designed to discard cases of $MUF_{[OIASA]}$ out of the range of 1.5 MHz from the corresponding manual scaled MUF, considered incorrectly autoscaled. Different Q_t values have been tested, applying the receiver operating characteristic (ROC) curve method (Brown and Davis, 2006) to this binary classifier system, in order to evaluate the appropriate threshold Q_t. Once it is selected, all the procedure is automated. For each tested value of Q_t, a different fraction of the autoscaled MUF values is discarded ($Q>Q_t$) by the filter, while the remaining values are classified as positives ($Q<Q_t$). In the graphical plot in Fig. 6.5 is shown, by varying the Q_t threshold, the number of values correctly considered positives, being actually well scaled (True Positive events), against the number of values which are considered positives incorrectly (False Positive events), expressed as percentages over the number of well scaled ionograms (P) and bad scaled ones (N), respectively. The point associated to the best Q_t, highlighted in the figure, is the one which approaches more the upper left corner of the plot. Following this approach, the Q_t threshold value has been set to 1.7 MHz.

In Tab. 6.2 is presented the comparison between the OIASA behaviour without using the filtering procedure and applying it with a Q_t value set to 1.7 MHz. In case of applying the filter, it can be seen that 4 of the 11 wrong MUF estimates have been successfully discarded. As a consequence, the percentage of wrong MUF estimates decreases from 2.86% to 1.82%, without affecting the percentage of good MUF estimates, i.e. the percentage of autoscaled MUF assessed as at least "Acceptable".

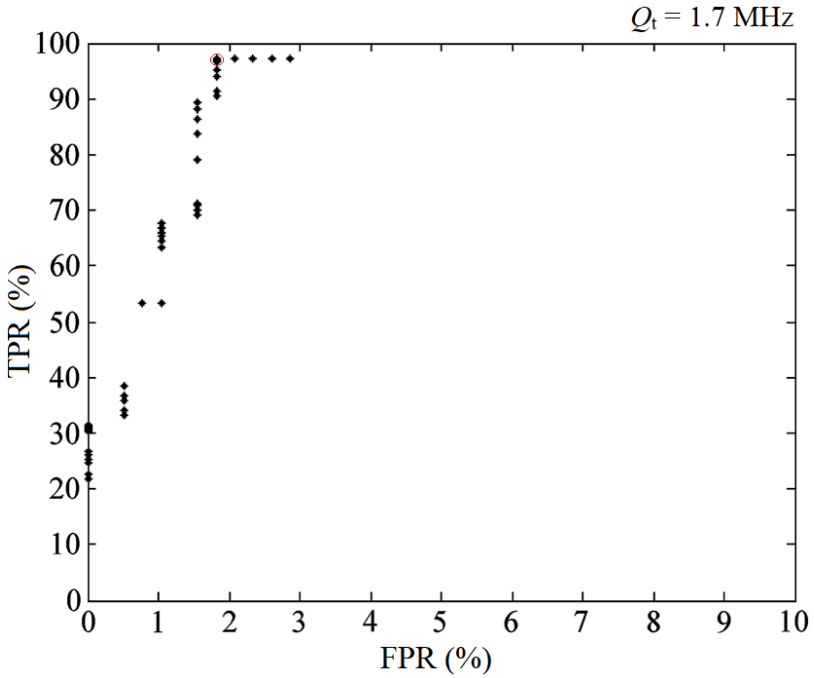

Fig. 6.5. The ROC curve for the binary classifier described in this study, where TPR (True Positive Rate) and FPR (False Positive Rate) are, respectively, TP/P and FP/N fractions expressed as percentages (Ippolito et al. 2016).

	Results Without *Q* Filter		Results With *Q* Filter	
	No. of Cases	(%)	No. of Cases	(%)
Well scaled (ΔMUF < 1.5 MHz)	373	97.14	373	97.14
Bad scaled (ΔMUF > 1.5 MHz)	11	2.86	7	1.82
Discarded	0	0	4	1.04
Total	384		384	

Tab. 2. Comparison between the behavior of OIASA without applying the *Q*-based filtering procedure and applying the filter with Q_t =1.7 MHz. (Ippolito et al., 2016)

6.4 Results on poor-quality test-mode NCEI ionograms recorded in South Korea

After the first test of the *Q*-based filtering procedure on SWS ionograms over Australia, OIASA and the procedure for its performance improvement have been applied to a new data set of oblique ionograms from the National Centers for Environmental Information (NCEI) division of the National Oceanic and Atmospheric Administration (NOAA), U.S.A. These ionograms are the result of the real-time oblique radio-soundings performed every 15 minutes since September 12, 2016 on the 1079 km radio-link between the Japanese National Institute of Information and Communications Technology (NICT) ionospheric station of Kokubunji (35.7° N, 139.5° E) and the Korean Space Weather Center (KSWC) station of Icheon (37.1° N, 127.5° E), shown in Fig. 6.6.
The NCEI oblique ionograms have been recorded using a Vertical Incidence Pulsed Ionospheric Radar (Grubb et at. 2008) Version 2 (VIPIR2) ionosonde, and are available on PNG images and NGI (NetCDF) data format. In this case, the actual power amplitude of the receiving echoes has been directly extracted from the NGI files, which contain also information about a statistically obtained noise calculated by the instrument. Thus, each ionogram in the data set has been stored in a matrix with elements values equals to the difference between the total received power and the noise stored in the corresponding NetCDF file.

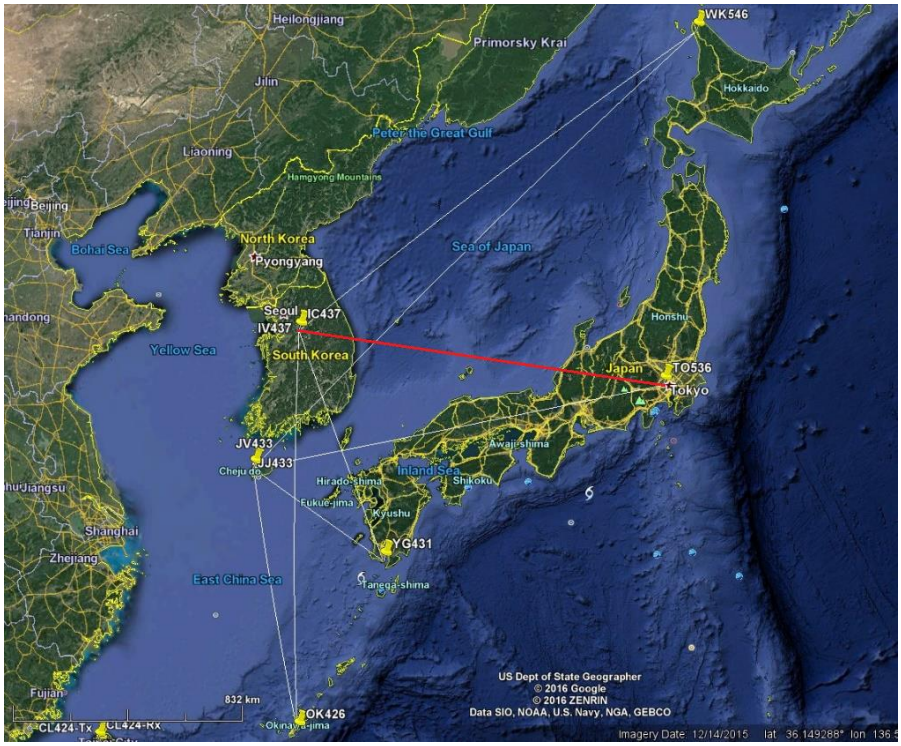

Fig. 6.6. The radio-links of the real-time oblique radio-soundings performed between Japan and South Korea. The 1079 km radio-link between Kokubunji (35.7° N, 139.5° E), Japan, and Icheon (37.1° N, 127.5° E), South Korea, is highlighted with a red line (courtesy of Terence Bullett).

A set of 288 poor-quality test-mode oblique ionograms recorded during October 5, November 3, and November 19, 2016 has been selected for this study. As shown in Fig. 6.7(a)-(b), the data quality is still poor, despite the reduction of the noise performed by the instrument. Indeed, more than 40% of the ionograms analyzed have no or little information (Fig. 6.7(a)), while in many other cases they suffered a lack of information for some frequency intervals (Fig. 6.7(b)), which contribute to a difficult distinction of the ordinary and the extraordinary traces, and MUF recognition as well.

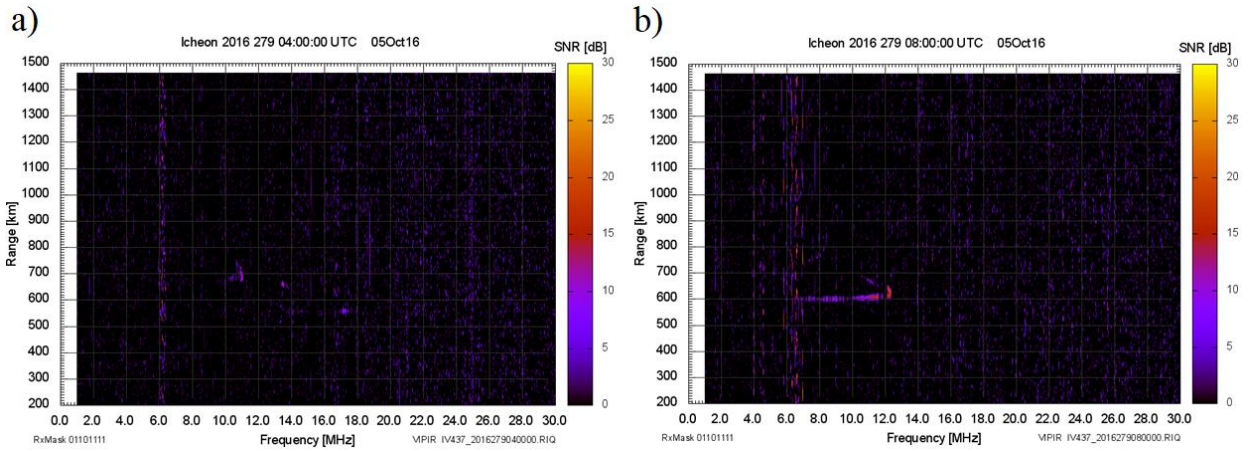

Fig. 6.7. Examples of NCEI ionograms in the data set with no or little information (a), or suffered a lack of information for some frequency intervals (b).

As the ionograms are affected to significant noise, two different filters have been applied before processing the data

in order to retrieve ionospheric information. In particular, a first filter has been applied to cut signals with power amplitude below a fixed threshold T_1. The conversion in matrices with only 0-1 values, corresponding to absence or presence of the information, respectively, has been performed after this first step. Since in these ionograms image background noise is often presented as vertical lines of pixels, a second filter has been applied to delete them. Thus, the information stored in each matrix column has been analyzed, and their numerical values are summed up. As each element is equal to 1 when there is information, and 0 otherwise, the summation is equal to the number of the pixels in the corresponding ionogram vertical line. When the fraction of pixels respect to the total number of elements in a matrix column is greater thana fixed fraction T_2, the entire column is assumed to be part of the noise, and then deleted. In Fig. 6.8(a)-(c) is shown an example of ionogram before and after the application of these filters, where the original ionogram is shown in black and white, too (Fig. 6.8(a)). This highlights the presence of significant noise all over the ionogram, regardless its amplitude.

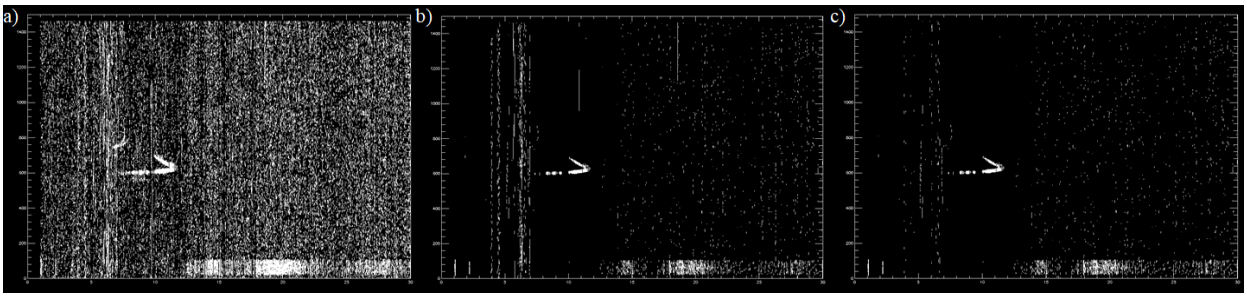

Fig. 6.8. Example of NCEI ionogram when no filters (a), only the first filter (b), and both the filters (c) described in this section are applied. The ionogram is recorded on October 5, 2016, 07:30 UT. The threshold of the filter 1 is set equal to T_1=6.5 dB, while the threshold of the filter 2 is T_2=0.1.

Different T_1, T_2, and C_t values have been tested, in order to obtain the best performance of OIASA with insufficient information. In particular, two different couples of values for T_1 and T_2 have been tested, leading to the following four different combinations for the threshold values of the two filters:

(1) T_1=6.0 dB and T_2=0.1, (6.7a)
(2) T_1=6.0 dB and T_2=0.2, (6.7b)
(3) T_1=6.5 dB and T_2=0.1, (6.7c)
(4) T_1=6.5 dB and T_2=0.2. (6.7d)

For each combination, different C_t values have been then tested, using the ROC curve method. Since the quality of the ionograms is poor, neither an experienced operator nor OIASA have been able to scale all of them. The ability of an operator to scale the MUF from the ionograms defines Positive (P) and Negative (N) cases. This means that P represents the number of cases in which an operator is able to scale the MUF from the ionogram, while N represents the remaining cases. The application of the ROC curve method to this binary classifier system, permits to assess the ability of OIASA to automatically detect and reject ionograms that even an expert operator could not interpret, in function of the value of C_t. Indeed, for a different C_t value, a different number of ionograms will be discarded (C<C_t), leading to a different number of correct (TP) or incorrect (FP) detections of good-quality ionograms.
Fig. 6.9 shows the ROC curves of C_t for the four different combinations of T_1-T_2 values. As already mentioned in the previous section, the threshold value C_t whose associated point in the corresponding plot approaches more its upper left corner, provides the best performance of the filter.
The C_t threshold values obtained following this approach are C_t =162-164 for cases (1) and (2), and C_t=162-178 for cases (3) and (4). Thus, in each case analyzed, the behaviour of OIASA in terms of rejection of ionograms with insufficient information has been the same for different values of C_t. In particular, in cases (3) and (4) the interval of values of same behaviour is quite large, from 162 to 178. This means that in these cases, no ionogram will be scaled by OIASA with C_{max} within this range, as varying C_t inside it, the same number of ionogram will be

discarded.

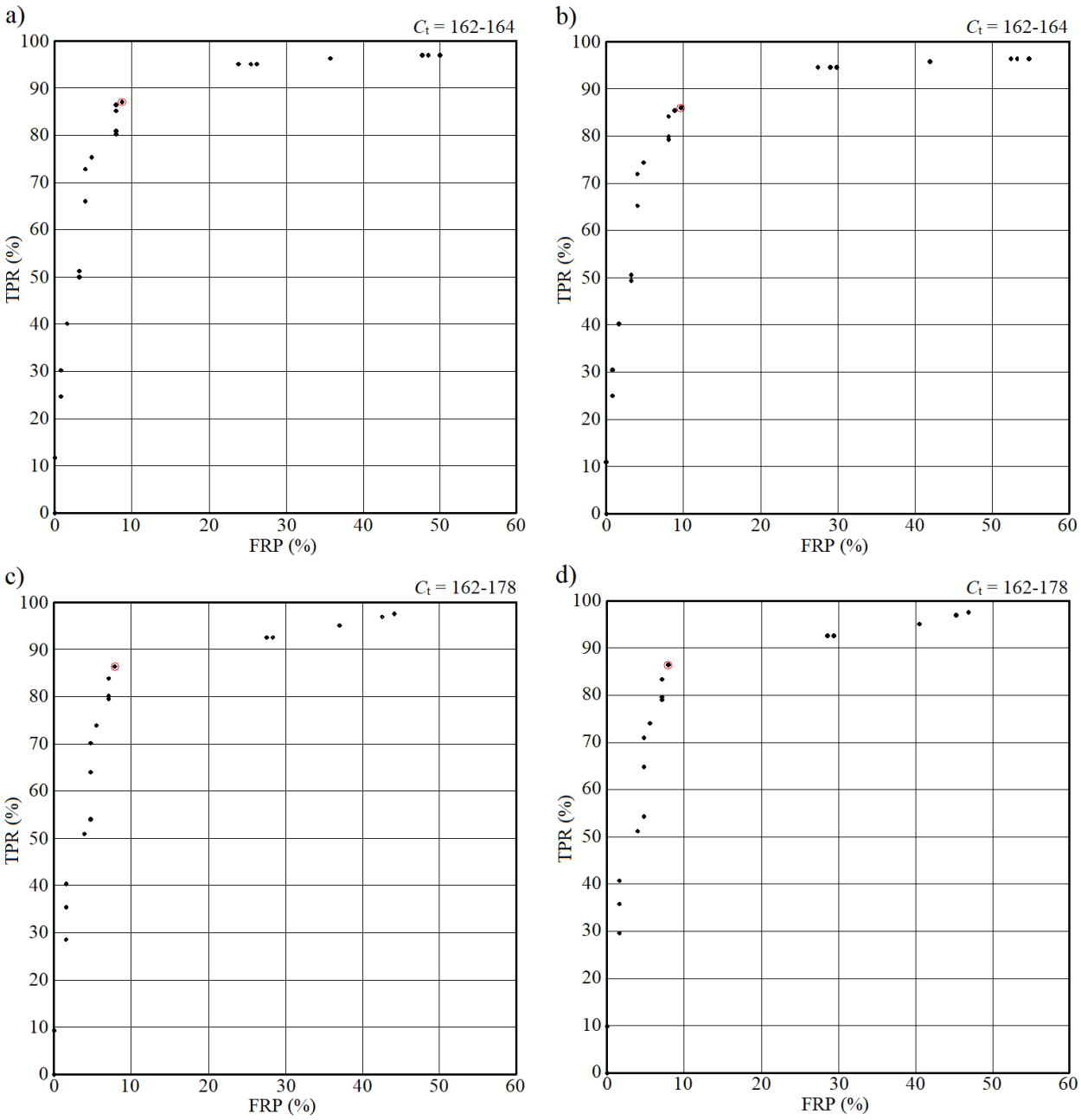

Fig. 6.9. ROC curves of C_t in case (1), with T_1=6.0 dB and T_2=0.1 (a), case (2), with T_1=6.0 dB and T_2=0.2 (b), case (3), with T_1=6.5 dB and T_2=0.1 (c), and case (4), with T_1=6.5 dB and T_2=0.2 (d).

In Tabs. 6.3(a), 6.4(a), 6.5(a), and 6.6(a) is reported the ability of both an experienced operator and OIASA to scale the ionograms, in cases (1), (2), (3), and (4), respectively, while in Tabs. 6.3(b), 6.4(b), 6.5(b), and 6.6(b)are shown the cases of accurate and acceptable autoscaled MUF values in the same cases, where the accuracy of the autoscaled MUF values has been assessed based on the comparison with the corresponding manually scaled values. In all cases C_t has been set equal to 162, being a common value for best OIASA performance in all cases.

(a)	Scaled by OIASA	Discarded by OIASA	Total	
Scaled by the operator	141 (TP)	21 (FN)	162 (P)	87.04% (TPR)
Discarded by the operator	11 (FP)	115 (TN)	126 (N)	8.73% (FPR)
Total	152	136		

(b)	Scaled by OIASA and the operator	
	# of cases	%
Accurate	43	30.5
Acceptable	83	58.9
Total	141	100.0

Tab. 6.3. Scaled and discarded ionograms by both an experienced operator and OIASA in case (1), with T_1=6.0 dB, T_2=0.1, and C_t=162 (a). Accurate and acceptable values for OIASA application on the same case (b).

(a)	Scaled by OIASA	Discarded by OIASA	Total	
Scaled by the operator	141 (TP)	23 (FN)	164 (P)	85.98% (TPR)
Discarded by the operator	12 (FP)	112 (TN)	124 (N)	9.86% (FPR)
Total	153	135		

(b)	Scaled by OIASA and the operator	
	# of cases	%
Accurate	45	31.9
Acceptable	85	60.3
Total	141	100.0

Tab. 6.4. Scaled and discarded ionograms by both an experienced operator and OIASA in case (2), with T_1=6.0 dB, T_2=0.2, and C_t=162 (a). Accurate and acceptable values for OIASA application on the same case (b).

(a)	Scaled by OIASA	Discarded by OIASA	Total	
Scaled by the operator	139 (TP)	22 (FN)	161 (P)	86.34% (TPR)
Discarded by the operator	10 (FP)	117 (TN)	127 (N)	7.87% (FPR)
Total	149	139		

(b)	Scaled by OIASA and the operator	
	# of cases	%
Accurate	57	41.0
Acceptable	95	68.3
Total	139	100.0

Tab. 6.5. Scaled and discarded ionograms by both an experienced operator and OIASA in case (3), with T_1=6.5 dB, T_2=0.1, and C_t=162 (a). Accurate and acceptable values for OIASA application on the same case (b).

(a)	Scaled by OIASA	Discarded by OIASA	Total	
Scaled by the operator	140 (TP)	22 (FN)	162 (P)	86.42% (TPR)
Discarded by the operator	10 (FP)	116 (TN)	126 (N)	7.94% (FPR)
Total	150	138		

(b)	Scaled by OIASA and the operator	
	# of cases	%
Accurate	55	39.3
Acceptable	94	67.1
Total	140	100.0

Tab. 6.6. Scaled and discarded ionograms by both an experienced operator and OIASA in case (4), with T_1=6.5 dB, T_2=0.2, and C_t=162 (a). Accurate and acceptable values for OIASA application on the same case (b).

It is noteworthy that the total numbers P and N of ionograms that an expert operator could or could not interpret, respectively, is not the same for all the cases. The reason is related to the fact that also the manual scaling has been performed on the filtered ionograms, as the original ones are affected to a noise level often too high to perform a reliable scaling. Furthermore, in this way the comparison between the ability of an experienced operator and OIASA to scale the MUF is performed under the same conditions, i.e. when the scaling is performed on the exact same ionograms. This means that the filters applied to the ionograms in order to reduce the noise, affect also the manual scaling procedure.

As can be seen from Fig.6.9 and Tabs. 6.3(a), 6.4(a), 6.5(a), and 6.6(a), the behaviour of OIASA in terms of rejection is similar in each case analyzed. This is confirmed by the C_t best values obtained, as the values 162 and 164 are in common to all cases. Since the position of the points associated to them in the ROC curve is almost the same, too, the case associated to the minimum FPR value has been chosen. Hence, the threshold values have been set equals to T_1=6.5 dB, T_2=0.1, and C_t=162, in accordance to the results obtained for case (3). The reason why the key

parameter in this decision has been the FPR value is related to the crucial need to avoid erroneous outputs. Thus, being the main goal obtaining reliable outputs, reducing the number of false positive events is considered more important than increasing the number of the true positives. Indeed, a bad output, when used for feeding a model or in a scientific study, can have a more negative effect than the lack of one more good output.

The accuracy of the data provided is an important issue, too. As can be seen comparing Tabs. 6.3(b), 6.4(b), 6.5(b), and 6.6(b), the percentages of accurate and acceptable autoscaled MUF values in the case (3) (Tabs. 6.5(b)), respectively 41.0% and 68.3%, are the highest. This confirms that the chosen values for T_1, T_2, and C_t are those associated to the best performance of OIASA. These percentages are calculated over the number of ionograms scaled by both the operator and OIASA, equal to 139. Indeed, the total number of ionograms scaled by OIASA has been 149, but 10 of these are not interpretable by an expert operator.

Following the procedure described in Section 6.1, the 149 ionograms scaled by OIASA have been converted in vertical equivalent ionograms. Then, the $f_oF_{2[Autoscala]}$ and $f_oF_{2[OIASA]}$ values corresponding to each of them, have been identified. In this case, Autoscala has been able to provide an f_oF_2 value for all the ionograms analyzed. Nevertheless, it has been not possible to calculate $f_oF_{2[OIASA]}$ in a specific case, namely October 5, 2016, 19:45 UT. This is related to an incorrect recognition by OIASA of the position of the tip of the ionogram "nose", with coordinates (MUF, $p'/2$(MUF)). Indeed, in this case the autoscaled $p'/2$ is too small to apply (6.5), being less than $R_T \cdot \sin\theta$. According to (6.5), this condition would lead to a $\sin\phi$ value greater than 1, which is not acceptable.

Fig. 6.10 shows the ionogram recorded on October 5, 2016, 19:45 UT, filtered using the threshold values T_1=6.5 dB, T_2=0.1, and scaled by OIASA with C_t=162. Being C_{max}=178, the ionogram has been actually autoscaled, even though it has insufficient information: no trace is indeed present. Thus, the analysis of this case suggests that it is reasonable to assume that when $f_oF_{2[OIASA]}$ cannot be provided, the original oblique ionogram lacks sufficient information. In order to discard such cases, a high Q value has to be associated to the corresponding autoscaled MUF. In this study Q=30 has been associated to the MUF scaled by OIASA from the ionogram recorded on October 5, 2016, 19:45 UT, in order to be greater of every Q_t tested.

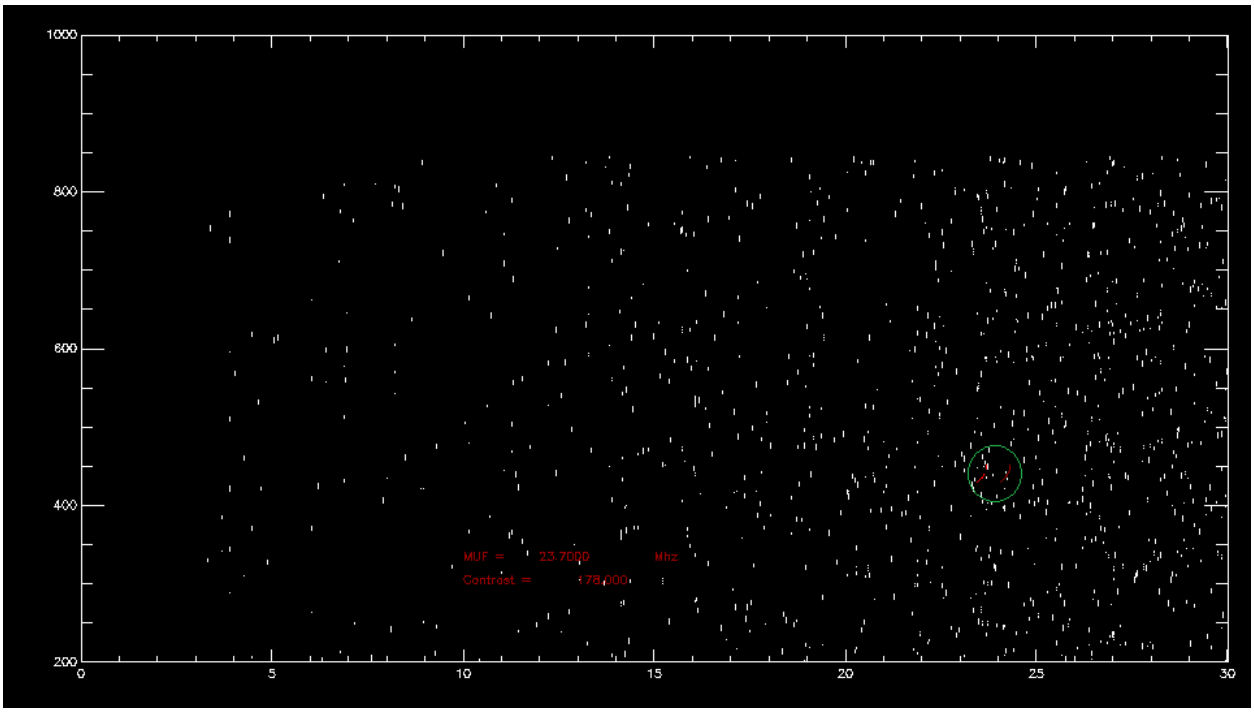

Fig. 6.10. Ionogram recorded on October 5, 2016, 19:45 UT, filtered using the threshold values T_1=6.5 dB, T_2=0.1, and scaled by OIASA with C_t=162. The position of the estimated traces is highlighted with a green circle.

After a Q value has been associated to all of the 149 ionograms scaled by OIASA and converted in vertical equivalent ionograms, the Q-based filter procedure has been applied. As the method has been applied to a poor-

quality ionograms data set, in this case the rejection procedure has been designed to discard further ionograms with no sufficient information. In that respect, it is noteworthy that applying this procedure to a poor-quality ionograms data set permits to improve the OIASA ability to reject ionograms deemed to lack sufficient information, which, conversely, cannot be tested to high-quality ionograms.
Different Q_t values have been tested, using the ROC curve method, in order to evaluate the threshold Q_t which optimize the behaviour of the whole system. Indeed, an ionogram of the original data set is discarded if $C_{max}<C_t$ or, in case it is scaled by OIASA, if $Q>Q_t$. In Fig. 6.11 is shown the ROC curve obtained varying Q_t in a proper interval. The point associated to the Q_t values which provide the best performance of the system is highlighted in the figure.

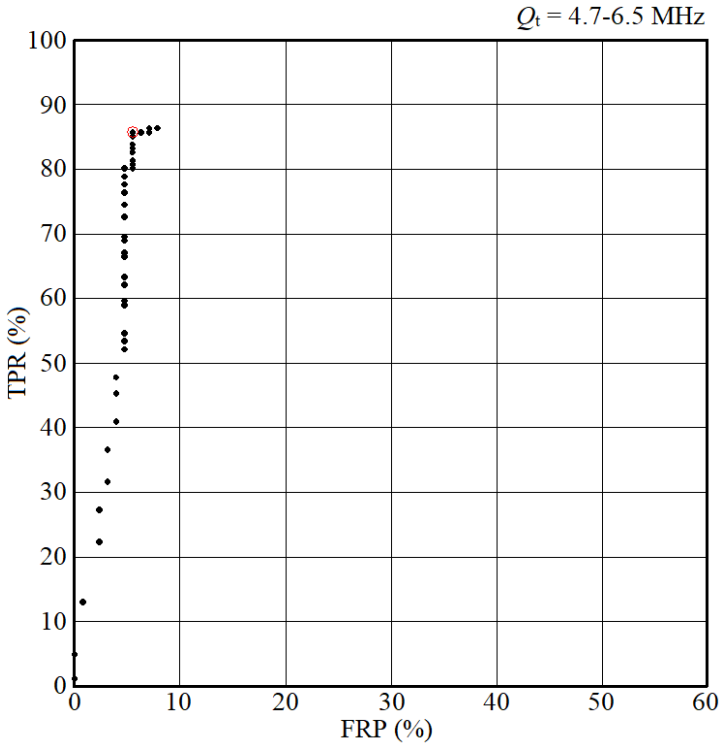

Fig. 6.11. ROC curve of Q_t assessing the behaviour of the entire system in terms of rejection of ionograms with insufficient information.

As for C_t, also in this case the best behaviour of the system analyzed is the same for different values of Q_t, which are within the interval 4.7-6.5 MHz. This means that no ionogram has a Q value within this range, as varying Q_t inside it, the same number of ionogram will be discarded.
It is worth noting that the point in Fig. 6.11 with the highest values of TPR and FPR correspond to the point associated to the best C_t value in Fig. 6.9(c). Indeed, it is the point associated to the highest Q_t value considered in the variation process, that is Q_t=30 MHz, for which no further ionogram is discarded, i.e. as if the Q-based filtering procedure was not applied at all. As Q_t decreases from this value, further ionograms will be discarded, being new True Negative (TN) cases or False Negative (FN) ones, depending on the quality of the ionogram discarded. Being P=TP+FN and N=TN+FP, with P and N fixed by the manual scaling procedure, to an increase of TN and FN corresponds a decrease of FP and TP, respectively, and, consequently, of FPR and TPR. This is the reason why all the points in the ROC curve in Fig. 6.11 are associated to lower values of FPR and TPR than the point associated to the best C_t value in Fig. 6.9(c), corresponding to the situation before applying the Q-based filtering procedure.
As can be seen by the comparison between Tabs. 6.5(a) and 6.7(a), the Q-based filtering procedure applied with Q_t=4.7-6.5 MHz has discarded further 4 ionograms, 3 of which lacks sufficient information. The new FPR and TPR values obtained are 5.5% and 85.7%, respectively. The FPR is then about 2.4% less than before, leading to a good improvement of the behaviour of the system in terms of rejection, while the TPR is only about 0.6% less than without applying the Q-based filter.

(a)	Scaled by OIASA	Discarded by OIASA	Total	
Scaled by the operator	138 (TP)	23 (FN)	161 (P)	85.7% (TPR)
Discarded by the operator	7 (FP)	120 (TN)	127 (N)	5.5% (FPR)
Total	145	143		

(b)	Scaled by OIASA and the operator	
	# of cases	%
Accurate	56	40.6
Acceptable	94	68.1
Total	138	100.0

Tab. 6.7. Scaled and discarded ionograms by both an experienced operator and OIASA, when OIASA and the *Q*-based filtering procedure are applied with C_t=162 and Q_t=4.7 MHz to the 288 NCEI ionograms analyzed (a). Accurate and acceptable values for OIASA and the *Q*-based filter application on the same data set and with the same settings (b).

In Tab. 6.7(b) are shown the cases of accurate and acceptable autoscaled MUF values when the *Q*-based filter is applied with Q_t=4.7 MHz. From the comparison between this table and Tab. 6.5(b), it can be seen that the ionogram erroneously discarded by the *Q*-based filtering procedure, recorded on October 5, 21:00 UT, has been considered accurately scaled by OIASA. The analysis of this ionogram shows that it has been rejected, because of a wrong $f_oF_{2[Autoscala]}$ estimation caused by the poor-quality of the ionogram. Indeed, as shown in Fig. 6.12(a), the ionogram is affected to significant noise even after the filtering procedure, and only a very little portion of the trace can be observed. Fig. 6.12(b) shows the vertical equivalent ionogram, along with the Autoscala and AIP outputs. It can be clearly seen that the distortion of the ionogram obtained from the oblique to vertical ionogram conversion, does not allow to distinguish the trace from the background noise. However, it is worth noting that the poor-quality of the ionogram leads to a questionable manual scaling. Thus, it represents a critical case, in which the ionogram may have been discarded by the operator. This means that the *Q*-based filtering procedure has shown a capability of discarding doubtful cases.

In conclusion, the algorithm described and tested in this study can be considered as an efficient method to improve the performance of OIASA, which can be proposed as a system to obtain the real-time MUF from oblique ionograms. Indeed, this procedure has shown a good behaviour in terms of rejecting wrong MUF estimates obtained by OIASA in different conditions. As shown in Section 6.3, the definition of the quality factor *Q* and the application of a *Q*-based filtering procedure to a high-quality ionograms data set, can lead to a decrease of autoscaled MUF values out of the range of 1.5 MHz from the corresponding manual scaled values. Moreover, as confirmed by the results obtained in this section, the application of the procedure to a poor-quality ionograms data set can improve the capability of the system to detect and reject ionograms lacks to sufficient information, which, if not rejected, would result in further wrong MUF estimates. However, the case of the ionogram shown in Fig. 6.12(a)-(b) confirms that the quality of the input ionograms is a critical issue for an automatic scaling program.

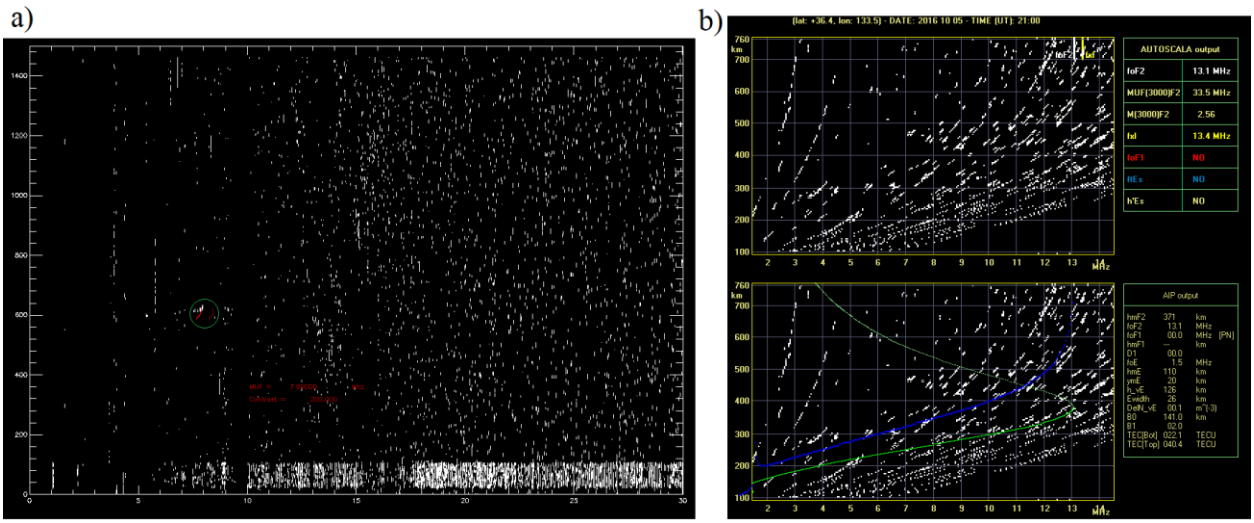

Fig. 6.12. Ionogram recorded on October 5, 2016, 21:00 UT, filtered using the threshold values T_1=6.5 dB, T_2=0.1 (a). The position of the estimated traces is highlighted with a green circle. The vertical equivalent ionogram obtained from the oblique to vertical conversion, along with the Autoscala and AIP outputs, is shown in (b).

References

[1] Scotto, C., and M. Pezzopane (2008), Removing multiple reflections from the F2 layer to improve Autoscala performance, J. Atmos. Sol. Terr. Phys., 70, 1929–1934.

[2] Norman, R.J., Cannon, P.S., 1999. An evaluation of a new two-dimensional analytic ionospheric ray-tracing technique: segmented method for analytic ray tracing (SMART). Radio Sci. 34 (2), 489–499. http://dx.doi.org/10.1029/98RS01788.

[3] Lastovicka, J., A3 IONOSPHERIC ABSORPTION MEASUREMENTS AT 1538 kHz - FIRST RESULTS, Studiageoph. et geod., 22, 1978.

[4] Penndorf, R., A spread-F index (research note), J. Atmos. Terr. Phys. 24 (6), 543-545, 1962.

[5] Tsunoda, R. T., Satellite traces: An ionogram signature for large-scale wave structure and a precursor for equatorial spread F, GEOPHYSICAL RESEARCH LETTERS, VOL. 35, L20110, doi:10.1029/2008GL035706, 2008.

[6] MacDougall, J. W., Hall, G. E., Hayashi, K., F region gravity waves in the central polar cap, Journal of Geophysical Research, vol. 102, no. A7, pp14,513-14,530, July 1997.

[7] Herman, J. R., Spread F and Ionospheric F-Region Irregularities, REVIEWS OF GEOPHYSICS, VOL.4, No. 2, MAY 1966.

[8] King, G. A. M., Spread-F on ionograms, Journal of Atmospheric and Terrestrial Physics, Vol. 32, pp. 209-221, 1970.

[9] Frank-Kamenetsky, A. and Troshichev, O., A relationship between the auroral absorption and the magnetic activity in the polar cap, Journal of Atmospheric and Solar-Terrestrial Physics, 77, 4045, 2012.

[10] Scotto, C. and Pezzopane, M., Automatic scaling of polar ionograms, Antarctic Science, doi:10.1017/S0954102011000587, 2011.

[11] Gething, P. J. D., and R. G. Maliphant (1967), Unz's application of Schlomilch's integral equation to oblique incidence observations, J. Atmos. Terr. Phys., 29, 599–600.

[12] Phanivong, B., J. Chen, P. L. Dyson, and J. A. Bennet (1995), Inversion of oblique ionograms including the Earth's magnetic field, J. Atmos. Terr. Phys., 57, 1715–1721.

[13] Reilly, M. H., and J. D. Kolesar (1989), A method for real height analysis of oblique ionograms, Radio Sci., 24, 575–583, doi:10.1029/RS024i004p00575.

[14] Huang, X., Reinisch, B.W., Kuklinski, W.S., 1996. Mid-point electron density profiles from oblique ionograms. Ann. Geophys. Italy 49 (4), 757–761. http://dx.doi.org/10.4401/ag-4012.

[15] Ippolito, A., C. Scotto, M. Francis, A. Settimi, and C. Cesaroni (2015), Automatic interpretation of oblique ionograms, Adv. Space Res., 55, 1624–1629.

[16] Ippolito, A., Scotto, C., Sabbagh, D., Sgrigna, V., Maher, P. (2016). A procedure for the reliability improvement of the oblique ionograms automatic scaling algorithm. Radio Sci. 51, doi:10.1002/2015RS005919.

[17] Martyn, D. F. (1935), The propagation of medium radio waves in the ionosphere, Proc. Phys. Soc., 47, 323–339.

[18] Gething, P. J. D. (1969), The calculation of electron density profiles from oblique ionograms, J. Atmos. Terr. Phys., 31, 347–354.

[19] Kol'tsov, V. V. (1969), Determination of virtual reflection heights from oblique sounding data, Geomagn. Aeron. (USSR), 9(5), 698–701.

[20] Scotto, C. (2009), Electron density profile calculation technique for Autoscalaionogram analysis, Adv. Space Res., 44(6), 756–766, doi:10.1016/j.asr.2009.04.037.

[21] Gardiner-Garden, R., Ayliffe, J., Durbridge, L., Frazer, G., Heitmann, A., Praschifka, J., Scarman, G., Turley, M., A new high-fidelity oblique HF receiving system, In Proc. IES2008 12th International Ionospheric Effects Symposium, pp. 482-491, 2008.

[22] Piggott, W. R., and K. Rawer (1972), U.R.S.I. Handbook of Ionogram Interpretation and Reduction, US Department of Commerce NationalOceanic and Atmospheric Administration-Environmental Data Service, Asheville, N. C.

[23] Brown, C. D., and H. T. Davis (2006), Receiver operating characteristics curves and related decision measures: A tutorial, Chemom. Intell. Lab. Syst., 80, 24–38.

[24] Grubb, R.N., Livingston, R., Bullett, T.W. A new general purpose high performance HF Radar. XXIX URSI General Assembly, Chicago, IL, USA, 2008.

7. Autoscaled MUF assimilation in RATIM

In order to give an increasingly realistic representation of the ionosphere on regional scale, a combined vertical and oblique radio-soundings data assimilation procedure has been proposed for RATIM model. As shown in Chapters 4 and 5, RATIM has demonstrated a good degree of adaptability to different ionospheric conditions, when applied over the Italian area. Different tests have been performed to assess RATIM performance in geomagnetically quiet and disturbed conditions (Sabbagh et al., 2016), and during the March 20, 2015 partial solar eclipse, when correction on critical frequencies formulation have been introduced, in order to take into account the variation of solar irradiance in such particular events.
After developing and testing the vertical plasma frequency profiles $f_p(h)$ assimilation procedure described in Chapter 4, a Maximum Usable Frequencies (MUFs) ingestion technique has been then introduced in RATIM. A simple HF ray-tracing technique has been used to model the skip distance for the frequency of a signal obliquely transmitted towards a specific ionosphere. When the input frequency is the MUF for a known radio-link under specific ionospheric conditions, the associated skip distance in the direction of the receiver corresponds to the ground range of the radio-link itself. The comparison between the real and simulated ground range values is performed for each combination of the RATIM free parameters tested during the $f_p(h)$ ingestion, introducing a further condition to the $f_p(h)$ *RMSD* minimization. The HF ray-tracing technique used is based on the ray equation, and thus strictly valid under simplified conditions, in accordance to the ray equation theory. A simplified ionosphere between the transmitter and the receiver has been assumed, extending to the whole radio-propagation channel the same parabolic vertical profile constrained to some F_2 characteristics dependent to the RATIM free parameters.
A preliminary study of application of this method is presented, when the MUF-ingesting version of RATIM has been applied to the Japanese-South Korean region. A limited data set of vertical ionograms recorded at Jeju (South Korea, 33.4° N, 126.3° E) and Icheon (South Korea, 37.1° N, 127.5° E), and oblique ionograms recorded between Kokubunji (Japan, 35.7° N, 139.5° E) and Icheon, has been used in this study. RATIM adaptability has been tested, comparing minimized $f_p(h)$ *RMSD* values when only $f_p(h)$ are ingested and applying the MUFs assimilation. Discrepancies between the real ground range and values obtained in adapting conditions are also compared, when different thresholds are applied to such discrepancies as a condition to consider effective the adapting. RATIM ability to reject incorrect data has also been tested, when $f_p(h)$ and MUF values are validated by an expert operator. Comparison between some preliminary ray-tracing results obtained applying the ray equation, Snell's law, and Fermat's principle in simplified ionospheric conditions are also presented.

7.1 Eikonal based ray-tracing technique

The MUF ingestion technique introduced in RATIM is based on the skip distance simulation for fixed frequency obliquely transmitted towards a specific ionosphere. This is calculated through numerical simulations, making use of a HF ray-tracing algorithm able to retrieve the path of a radio wave, when its frequency and elevation angle α are known. Indeed, gradually changing α for a HF signal transmitted with specific frequency, the lower limit of the distance attainable for ionospheric propagation in specific conditions can be obtained.
Different methods can be used for the HF ionospheric ray-tracing, depending on the assumption considered in the medium representation, and on the specific problem to be solved. The ray-tracing algorithm used by RATIM is based on the eikonal method (Borovskikh, 2010), as it performs a discrete integration of the differential ray equation:

$$\frac{d}{ds}\left(n(s)\frac{d\vec{r}(s)}{ds}\right) = \nabla n(s), \tag{7.1}$$

where s is the curvilinear coordinate of the ray, $\vec{r}(s)$ is the parametric equation of the trajectory, and n is the phase refraction index for the travelling radio wave, which must be known along the whole path. The local direction of the ray propagation is given by:

$$\hat{s}(\vec{r}) = \frac{d\vec{r}(s)}{ds}, \tag{7.2}$$

which represents the tangent unit vector in each point of the ray path. The eikonal method can be used assuming the wave frequencies high enough to be described in terms of rays (geometric optics approximation), and for a medium characterized by a slowly varying n in space. Since the variations in the medium have a much smaller scale length than the wavelengths in question, the ionosphere can be approximated to a homogeneous isotropic medium (Bianchi, C. and Bianchi, S., 2009). Under these assumptions, the phase spatial variations or the travelling radio wave can be related to $n(\vec{r})$ through the so-called eikonal equation:

$$|\nabla S(\vec{r})| = n(\vec{r}), \tag{7.3}$$

where the gradient of the eikonal function $S(\vec{r})$ gives the local direction of the ray propagation. Thus, the unit vector tangent to the trajectory in each point can also be expressed as:

$$\hat{s}(\vec{r}) = \frac{\nabla S(\vec{r})}{|\nabla S(\vec{r})|} = \frac{\nabla S(\vec{r})}{n(\vec{r})}, \tag{7.4}$$

where the eikonal equation (7.3) has been used. When the curvilinear coordinate of the ray is introduced, the comparison between (7.4) and (7.2) leads to:

$$n(s)\frac{d\vec{r}(s)}{ds} = \nabla S(s), \tag{7.5}$$

whose derivation relative to s produces the differential ray equation (7.1). The equation (7.1) has the advantage of describing the ray trajectory knowing only the n spatial distribution, and it can be numerically integrated much more easily respect the eikonal equation (7.3). This is particularly simple when the EMF and collisions between ions and neutrals are ignored, so that the refraction index for radio waves in the ionosphere can be expressed as a simple function of f_p. Under this simplified condition, its spatial distribution is given by:

$$n(\vec{r}) = \left(1 - \left(\frac{f_p(\vec{r})}{f}\right)^2\right)^{1/2}, \tag{7.6}$$

where f is the radio wave frequency.

Fig. 7.1(a)-(f) shows the comparison between the behaviour of the eikonal based ray-tracing algorithm used in RATIM, and results obtained using different approaches to retrieve the ray path of radio waves travelling through the ionosphere. The same parabolic $N(h)$ profile has been assumed in the whole region where radio signals with fixed frequency are obliquely transmitted upwards, following different paths depending on α, and Earth's surface and the ionosphere are both considered flat. N is fixed equal to zero from the ground up to the base of the ionosphere, modeled at 150 km, where N begin to increase up to $6 \cdot 10^{12}$ m^{-3}, reached at 450 km altitude. Black lines are obtained using the eikonal based ray-tracing algorithm used in RATIM, while green lines are obtained using Snell's law. Red circles are obtained using a ray-tracing algorithm based on the Fermat's principle (Coleman, 2011). It is noteworthy that the absence of the EMF makes the medium isotropic. Under this assumption, each trajectory can be considered to lie on the azimuthal plan, identified by the initial direction of the ray and the vertical direction over the emission point.

For isotropic media, the Fermat's principle states that the ray between two points is that for which the phase distance, or optical path, is stationary, and is given by:

$$\delta \int_A^B n ds = 0. \tag{7.7}$$

Thus, the ray is found by searching over the possible ray-paths that join the end points (A and B) to find the one that makes the phase distance stationary, making this method particularly suited to problems where the end points are known. The algorithm here used is designed to satisfy (7.7) through an iterative approach, evaluating the spatial gradient of the optical path *nds*, to be locally minimized at each step. For fixed frequency and end points, the initial ray-path through the ionosphere is represented as a randomly chosen broken lines, whose points of direction changes are those highlighted with blue empty circles in Fig. 7.1(a)-(f). A *nds* value is evaluated for each segment of the path, considering the *n* value at the segment midpoint and the segment length. At each step, the algorithm sweeps all the edge points of the broken path, moving them in the direction opposite to the local optical path gradient, calculated considering the adjacent segments. In this way, the total optical path, i.e. the sum of the *nds* values associated to each ray-path segment, decreases at each step, approaching to zero after many iterations.

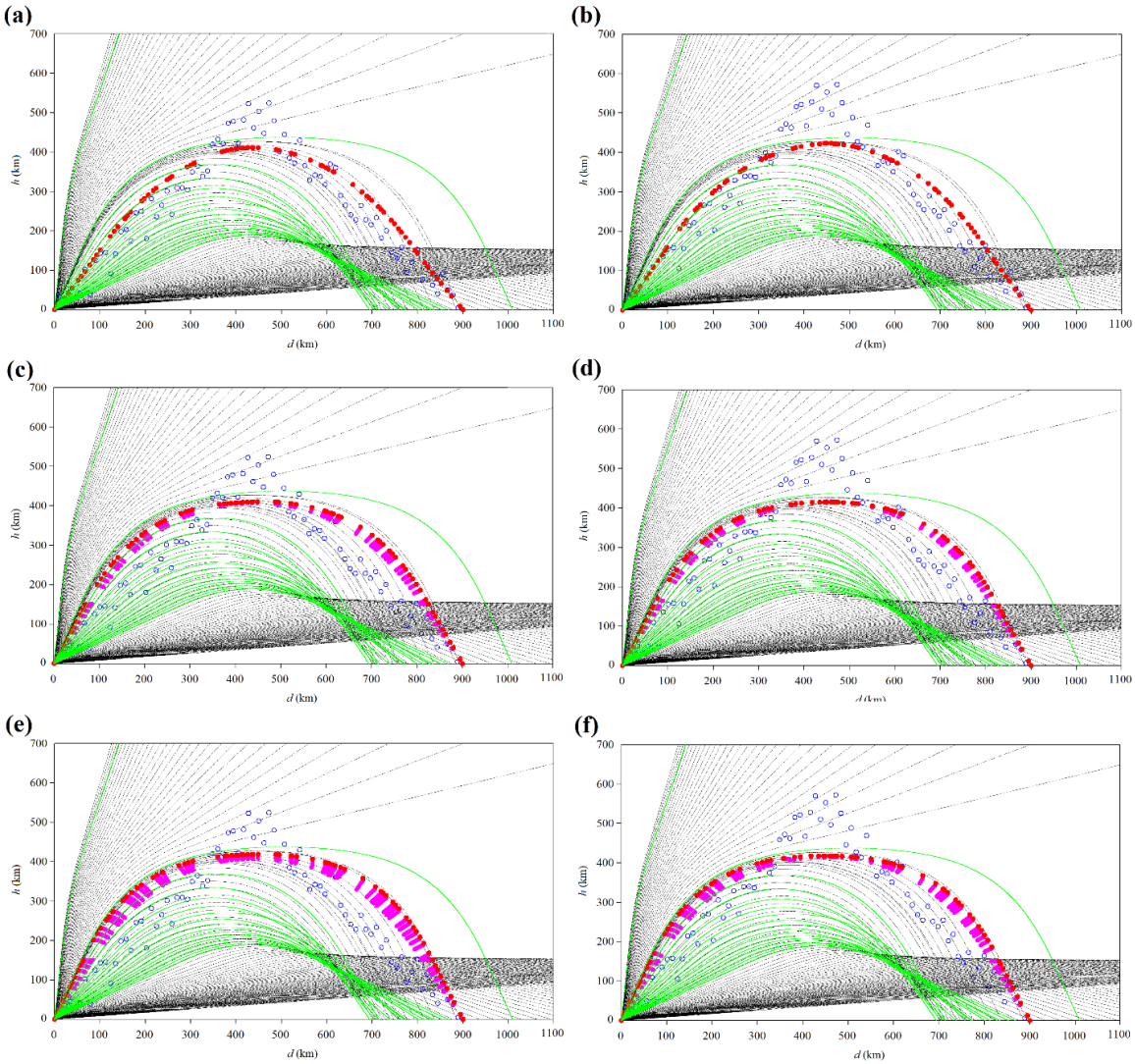

Fig. 7.1. Behaviour of the eikonal based ray-tracing algorithm used in RATIM (black lines), using Snell's law (green lines), and using Fermat's principle (red circles). Ray-paths obtained by Fermat's principle shown in (a), (c) and (e), and those in (b), (d) and (f) are obtained starting from two different random paths. The paths in (a) and (b) are obtained after 12,000 iterations, those in (c) and (d) after 120,000 iterations, and those in (e) and (f) after 600,000 iterations. Magenta circles are drawn for ray-paths whose total optical path is closer to zero than a certain small threshold. The same parabolic $N(h)$ profile has been assumed in the whole region.

From the comparison between different figures, it can be seen that when the number of the iteration is high, the total optical paths actually approaches to zero after each iteration, reaching very small values. Moreover, the ray-path obtained after many iterations does not depends of the initial condition, as the same trajectories are obtained in Figs. 7.1(e) and 7.1(f).

When the values of α are approximatively the same, ray-paths in Figs. 7.1(e) and 7.1(f) obtained through the different numerical approaches tested can be compared. The results suggested a consistence among all the methods, when applied in such simplified conditions. The eikonal based algorithm is then applied in RATIM, being more suitable for the skip distance simulation associated to fixed frequencies obliquely transmitted towards a specific ionosphere. However, the ray-tracing algorithm based on Fermat's principle used here seems to be promising as well, for this kind of application.

It is worth noting that the ray-path obtained minimizing the total optical path represents the trajectory of the Pedersen ray propagating between the end points. As suggested to results obtained starting from a low random path, shown in Figs. 7.2, the path of the low ray is associated to small values of the optical path, which however do not correspond to absolute minima. Indeed, it has been demonstrated that the solution associated to the low ray paths corresponds to a saddle point of the phase distance (Degiovanni, 2017).

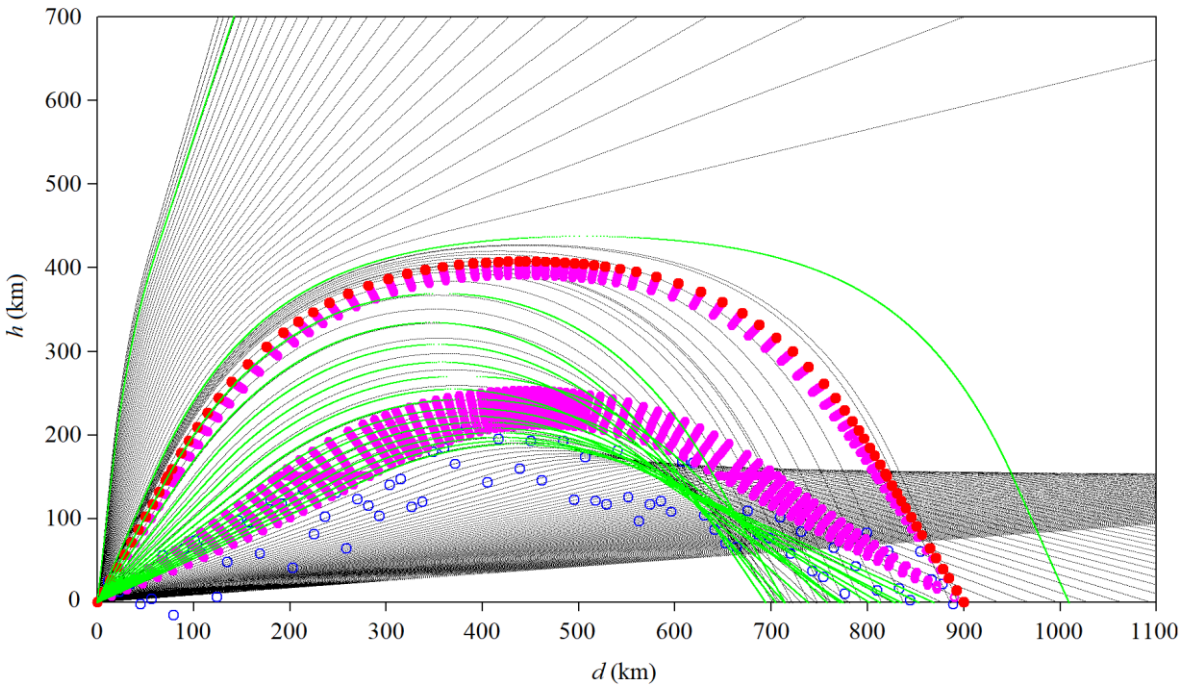

Fig. 7.2. Behaviour of the eikonal based ray-tracing algorithm used in RATIM (black lines), using Snell's law (green lines), and using Fermat's principle (red circles), in the same situation of Fig. 7.1. The results obtained using Fermat's principle have a low random path as initial condition. Magenta circles highlight the ray paths approaching those for the low and the high path.

7.2 RATIM MUFs assimilation preliminary results

A preliminary study of the combined vertical and oblique radio-soundings data assimilation procedure has been conducted, applying the MUF-ingesting version of RATIM to the Japanese-South Korean region, situated between 30.5º N to 42.0º N latitude, and 124.0º E to 142.5º E longitude. In this RATIM version, the new sunspot number internationally distributed by the Solar Influences Data analysis Center (SIDC, http://sidc.oma.be) of Brussels, Belgium, has been used for the description of the quiet ionosphere (Section 4.3), after introducing a scaling factor of 0.7. Indeed, a recent review of the way the sunspot number is determined from observations of spots on the Sun

resulted in a recalibration of its computation (Clette et al., 2014). Since the new index exceeds the old one by about a factor of 1.4, its use causes a problem for models developed using the old index. The scaling factor of 0.7 is the factor IRI-2016 model uses for ionospheric parameters modelling (Bilitza et al., 2017, and the references therein).
A limited data set of vertical ionograms recorded at Jeju (South Korea, 33.4° N, 126.3° E) and Icheon (South Korea, 37.1° N, 127.5° E) has been used in this study, along with the NOAA NCEI oblique ionograms recorded between Kokubunji (Japan, 35.7° N, 139.5° E) and Icheon at the same time. The oblique ionograms have been chosen among those used in the previous study, when 288 poor-quality test-mode oblique ionograms have been properly filtered from the HF noise, and analyzed by OIASA setting a contrast threshold C_t equal to 162. As described in Chapter 6, the Q-based filter procedure has also been applied to the considered oblique ionograms, in order to select MUF values to be ingested, with quality factor Q less than 4.7 MHz. In particular, a subset of 144 ionograms recorded during October 5, November 3, and November 19, 2016 every half an hour has been selected for this study. However, in 4 cases the $f_p(h)$ are missing in both the adapting stations, so that the adjustment procedure could not be performed.
The MUF ingestion technique introduced in RATIM is based on the skip distance simulation for fixed frequency obliquely transmitted towards a specific ionosphere. When the input frequency is equal to the MUF for a known radio-link under specific ionospheric conditions, the associated skip distance obtained in the direction of the receiver corresponds to the ground range D of the radio-link itself. The eikonal based ray-tracing algorithm described in the previous section has then been used to calculate the lower limit of the distance attainable for the propagation of radio waves at frequencies equal to MUF values autoscaled by OIASA for the Kokubunji-Icheon radio-link. A simplified ionosphere has been assumed, extending the same parabolic vertical profile to the whole radio-propagation channel. The profile is constrained to RATIM modeled characteristics, being its maximum anchored to the F_2 peak values modeled by RATIM over the radio-link mid-point, and being the thickness of the parabolic profile, related to B_0 modeled at the same point. For each combination of values for the RATIM free parameters Δf_oF_2, Δh_mF_2, and $\Delta\delta h_vE$ tested during the Jeju and Icheon $f_p(h)$ ingestion, the comparison between the real and the simulated D values for the Kokubunji-Icheon radio-link is performed, introducing a further adapting condition. Indeed, when a $f_p(h)$ *RMSD* is compared to the minimum value previously selected, it can be considered better than the latter only if the associated ground range discrepancy ΔD is less than a fixed threshold. Otherwise, it is discarded even though its value is lower than the current minimum one.
Adapted $f_p(h)$ *RMSD* values obtained when only $f_p(h)$ are ingested, and applying the MUFs assimilation with different ΔD thresholds, have been compared, in order to assess RATIM adaptability in different conditions. ΔD values obtained when MUFs assimilation has been performed have been compared as well. These results, averaged considering all available data, are reported in Tab. 7.1, along with percentages of success of the adjustment procedure. Tab. 7.2 shows the same values, obtained considering only validated input data. Following the approach used in the previous studies, validation of $f_p(h)$ profiles has been performed observing the ionograms from which they are restored (see Section 4.4), while validation of MUF values is based on the manually scaled values (see Sections 6.3 and 6.4).

	# cases	# MUF	# adapted	% adapted	⟨*RMSD*⟩ (MHz)	# ΔD	⟨ΔD⟩ (km)
Only $f_p(h)$ adapting	140	-	118	84.29	0.36	-	-
$f_p(h)$ and MUF adapting, ΔD_t = 50 km	140	72	94	67.14	0.36	28	32
$f_p(h)$ and MUF adapting, ΔD_t = 20 km	140	72	89	63.57	0.37	24	11

Tab. 7.1. Percentages of success of the adjustment procedure (4th column), adapting *RMSD*s (5th coloumn), and ΔD values (7h coloumn), obtained when only $f_p(h)$ are ingested (1st row), and applying the MUFs assimilation with different ΔD_t (2nd and 3rd row). All these values are obtained averaging over all available data. The total number of the considered cases (1st column), the number of autoscaled MUF available (2nd coloumn), the number of cases in which the adjustment procedure has been effective (3rd column), and the number of ΔD values obtained (6th coloumn) are also reported.

	# cases	# MUF	# adapted	% adapted	⟨*RMSD*⟩ (MHz)	# ΔD	⟨ΔD⟩ (km)
Only $f_p(h)$ adapting	65	-	62	95.38	0.31	-	-
$f_p(h)$ and MUF adapting, ΔD_t = 50 km	65	23	58	89.23	0.32	16	31
$f_p(h)$ and MUF adapting, ΔD_t = 20 km	65	23	56	86.15	0.33	14	12

Tab. 7.2. Percentages of success of the adjustment procedure (4th column), adapting *RMSD*s (5th coloumn), and ΔD values (7th coloumn), obtained when only $f_p(h)$ are ingested (1st row), and applying the MUFs assimilation with different ΔD_t (2nd and 3rd row). All these values are obtained averaging over only validated data. The total number of the considered cases (1st column), the number of autoscaled MUF available (2nd coloumn), the number of cases in which the adjustment procedure has been effective (3rd column), and the number of ΔD values obtained (6th coloumn) are also reported.

The results reported in Tab. 7.1 confirm that RATIM shows a capability to adapt to actual ionospheric condition even when applied in the Japanese-South Korean region. In particular, the model maintains this characteristic even when autoscaled MUF values from an oblique radio-sounding performed in the considered region are ingested, simultaneously with the $f_p(h)$ over a pair of ionospheric stations in the same area. Adapted *RMSD* values obtained in the different cases analyzed are in good agreement with those reported in Chapters 4 and 5. Moreover, adapting *RMSD* values are not nearly influenced by the MUF assimilation procedure. Conversely, assimilating MUF values decrease the percentage of success of the adjustment procedure, as a result of the further condition introduced to consider effective the adapting. Analyzing the data quality in cases of adapting failure, it can be seen than an enhanced failure percentage is the result of a capability of poor-quality data rejection, when the MUFs assimilation procedure is introduced. Indeed, , the MUF-ingesting RATIM version has adapted to very few incorrect MUF values in the data set, namely in only 4 cases over 24, even when it is able to fit $f_p(h)$ profiles alone. Figs. 7.3(a)-(b) and 7.4 show an example of such cases, in which validated $f_p(h)$ are ingested along with a not acceptable MUF value. While RATIM can fit the profiles with a *RMSD* equal to 0.41 MHz, the adjustment procedure fails when the model tries to ingest the wrong MUF.

Some cases in the data set suggest that when the MUFs assimilation procedure is introduced, RATIM shows also an improved capability of poor-quality $f_p(h)$ rejection. Indeed, when only $f_p(h)$ are ingested, RATIM often adapts to incorrect ones. When also a MUF value is assimilated, the ingested data usually turn out to be not consistent each other, and the adjusting procedure fails. An example of such behaviour is shown in Figs. 7.5 and 7.6, reporting a case in which only the Icheon vertical ionogram is available. Even though the retrieved $f_p(h)$ comes from a wrong f_oF_2 autoscaling, RATIM is able to fit it with a *RMSD* equal to 0.42 MHz. However, when it ingests the profile and the MUF simultaneously, the adjustment procedure fails. In this case, the autoscaled MUF is considered as "Accurate", although the poor-quality of the ionogram. However, the manual scaling has been validated observing the temporal series of ionograms around the hour of the considered sounding.

Finally, comparing the behaviour of the MUF-ingesting version of RATIM with different ΔD_t, it can be seen that the percentage of success of the adjustment procedure slightly decrease lowering its value, suggesting a slightly lower adaptability for lower ΔD_t. However, averaged adapting *RMSD* values turn out not to be nearly influenced by the set ΔD_t value, while the averaged adapting ΔD decrease lowering ΔD_t. This means that the degree of adaptability can be assessed better when low ΔD_t value are chosen.

(a)

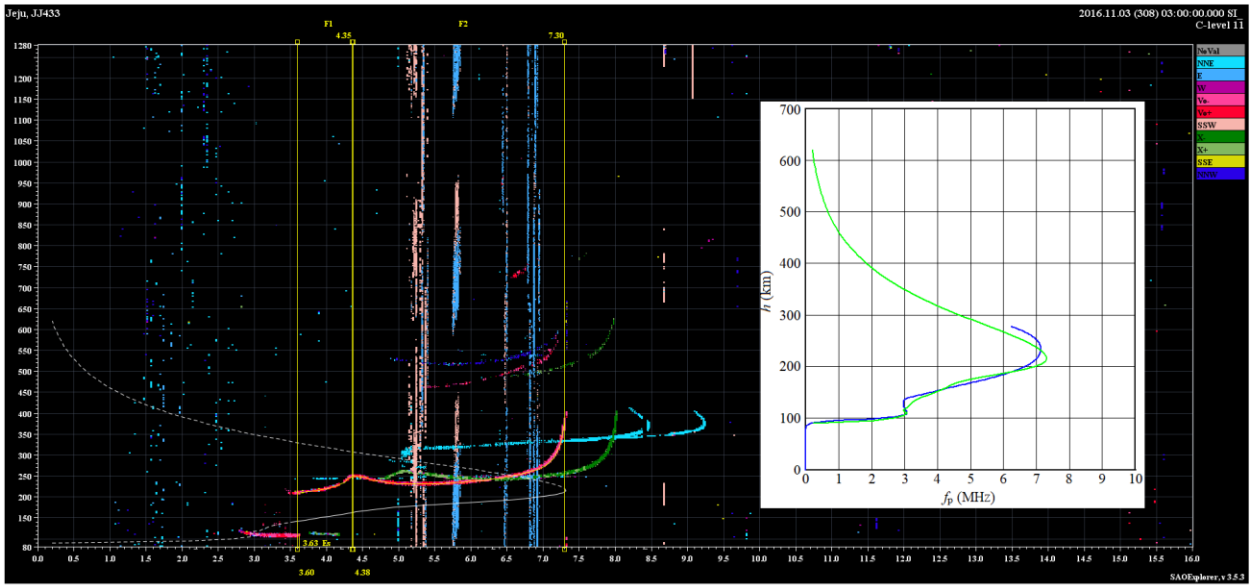

(b)

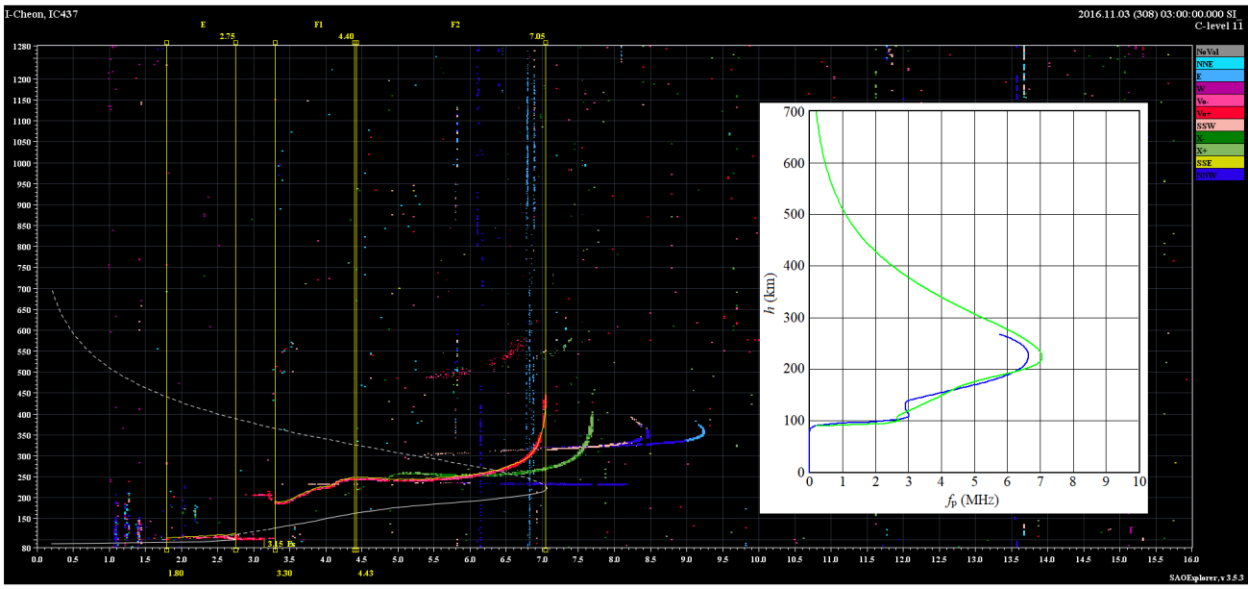

Fig. 7.3. Vertical ionograms recorded on November 3, 2016 at 03.00 UT over Jeju (South Korea, 33.4° N, 126.3° E) (a) and Icheon (South Korea, 37.1° N, 127.5° E) (b), along with the corresponding $f_p(h)$ retrieved from ARTIST. The white box on the right shows the result of the adjusting procedure, where green $f_p(h)$ are those retrieved from the corresponding ionograms and the blue ones are those modeled by RATIM in adapting conditions.

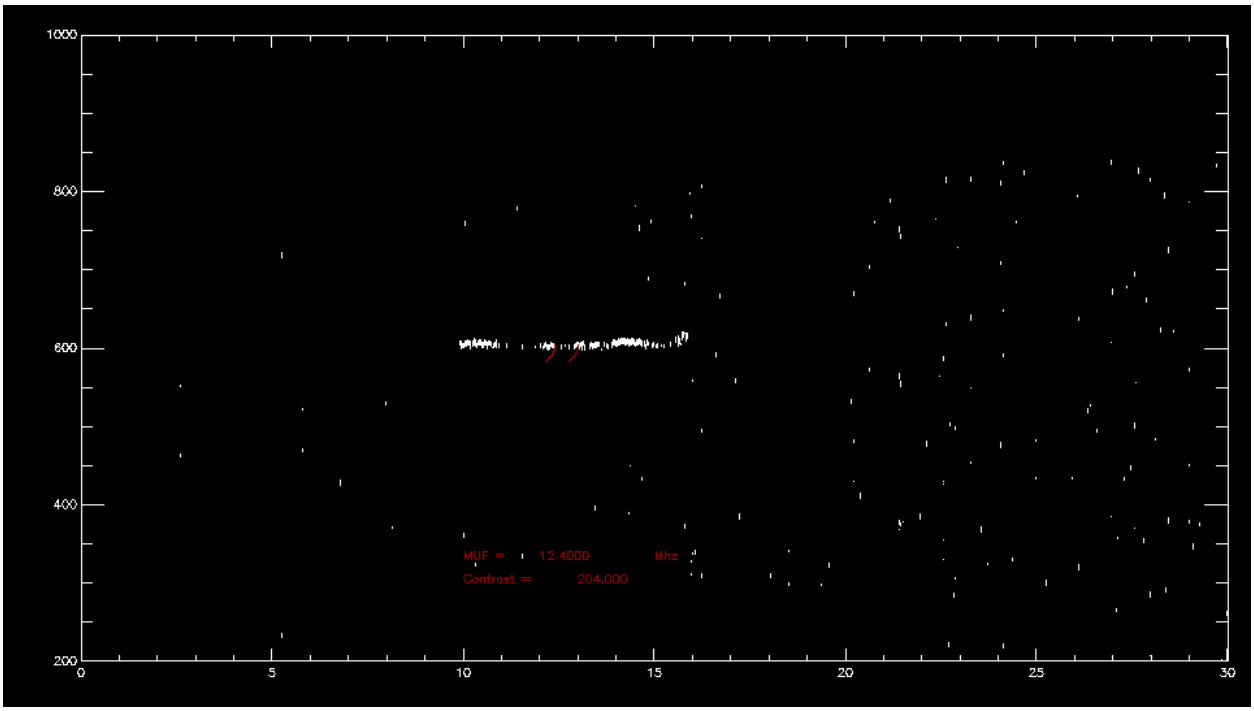

Fig. 7.4. Oblique ionogram from the oblique ionospheric radio-sounding performed between Kokubunji (Japan, 35.7° N, 139.5° E) and Icheon (South Korea, 37.1° N, 127.5° E) on November 3, 2016 at 03.00 UT. The ionogram shown is properly filtered before applying OIASA, whose MUF and contrast outputs are also reported.

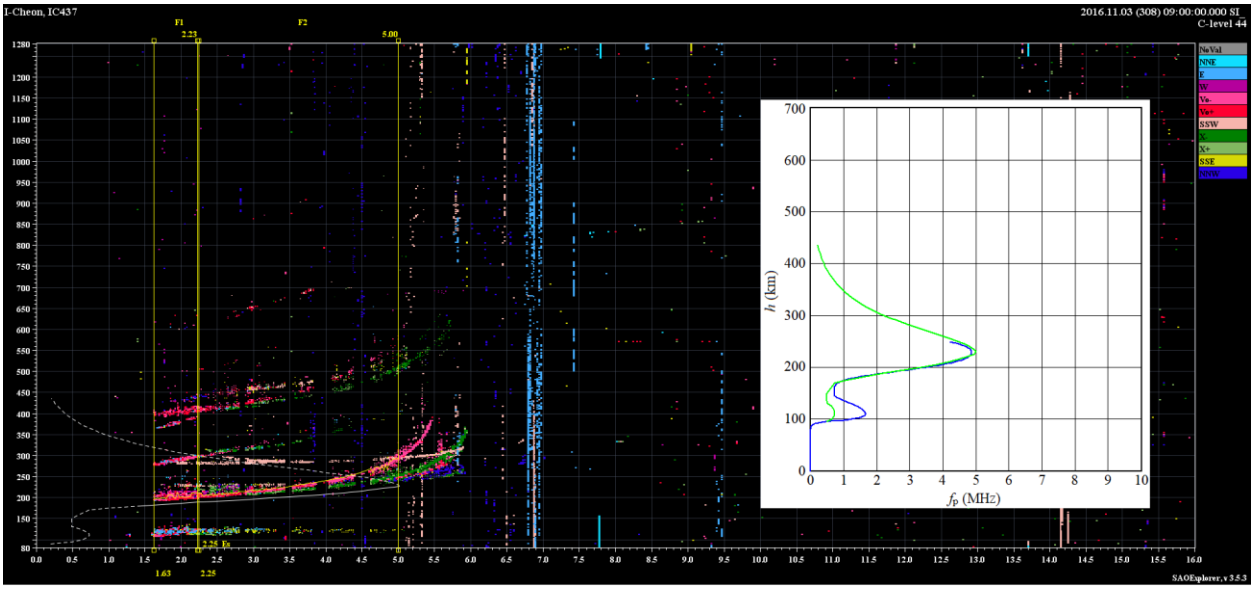

Fig. 7.5. Vertical ionogram recorded on November 3, 2016 at 09.00 UT over Icheon (South Korea, 37.1° N, 127.5° E) (b), along with the corresponding $f_p(h)$ retrieved from ARTIST. The white box on the right shows the result of the adjusting procedure, where green $f_p(h)$ is that retrieved from the corresponding ionogram and the blue one is that modeled by RATIM in adapting conditions.

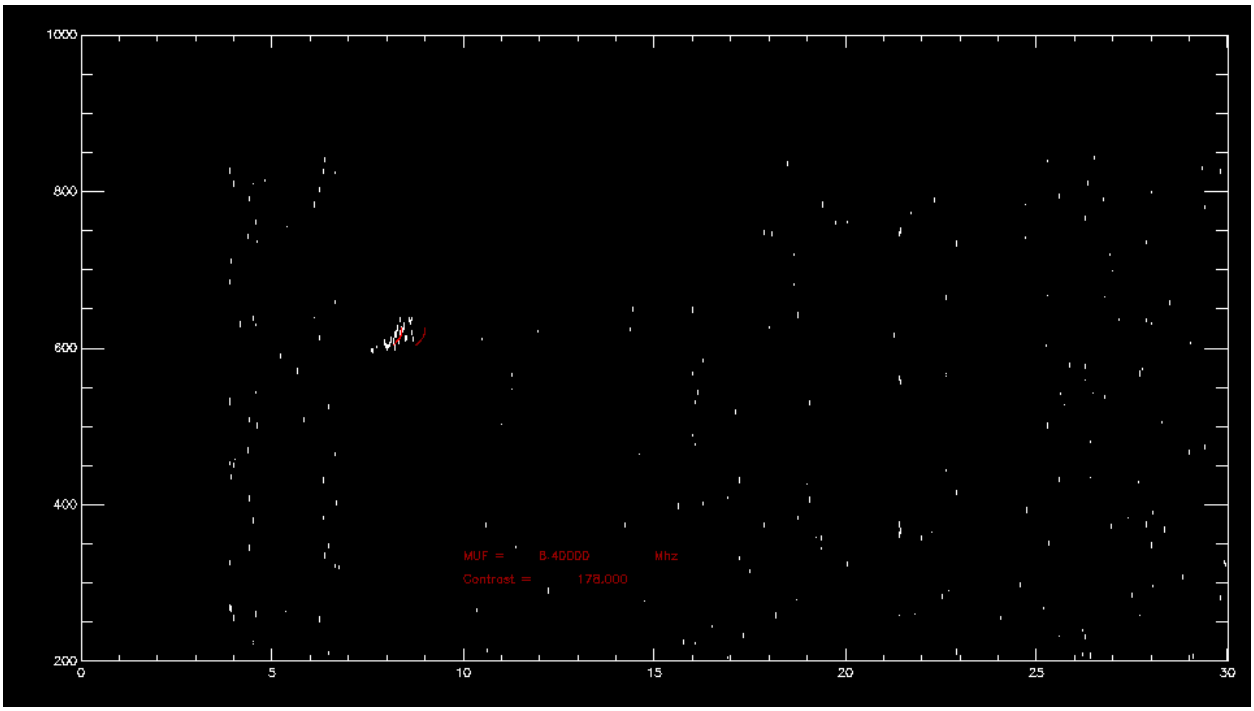

Fig. 7.6. Oblique ionogram from the oblique ionospheric radio-sounding performed between Kokubunji (Japan, 35.7° N, 139.5° E) and Icheon (South Korea, 37.1° N, 127.5° E) on November 3, 2016 at 09.00 UT. The ionogram shown is properly filtered before applying OIASA, whose MUF and contrast outputs are also reported.

Results reported in Tab. 7.2 are representative of RATIM behaviour when no incorrect input data are ingested. The fact that the percentages reported come to be higher than the corresponding values in Tab. 7.1 in every case, indicates that the model is able to more frequently fit correct ionosonde data than incorrect ones. This behaviour is the same regardless the nature of the input data and can be considered a further confirmation of the RATIM capability of rejecting low-quality data even when MUF values are ingested. However, a progressive decrease of these percentages is still observed when the MUF assimilation is performed, and when the value of the set ΔD_t is lowered down. Even in this case, the *RMSD* values still not vary significantly neither introducing the MUF assimilation nor varying ΔD_t. Conversely, averaged adapting ΔD decrease with ΔD_t, still suggesting a better degree of adaptability for low ΔD_t. Furthermore, computational times for the free parameters adjusting procedure are quite the same setting ΔD_t equal to 50 km and 20 km, although much longer than those needed to fit $f_p(h)$ profiles alone. Indeed, the mean time required when MUF values are ingested is about 90 minutes, versus a computational time less than 15 minutes for $f_p(h)$ assimilation alone. At present, this limits the possibility to apply the proposed assimilation technique for real-time characterization of the ionosphere, making this stage not yet operational.
As an example, some products are reported in in Figs. 7.7(a)-(c) and 7.8(a)-(b), when RATIM is applied to the Japanese-South Korean region October 5, 2016 at 06.00 UT, ingesting both retrieved $f_p(h)$ at Jeju and Icheon, and OIASA autoscaled MUF values from the radio-link between Kokubunji and Icheon. In particular, f_p maps at fixed different altitudes are shown in Fig. 7.7(a)-(c), while f_p cross-sectional for longitude φ=137.0º and fixed latitude λ=35.0º are reported in Figs. 7.8(a)-(b).

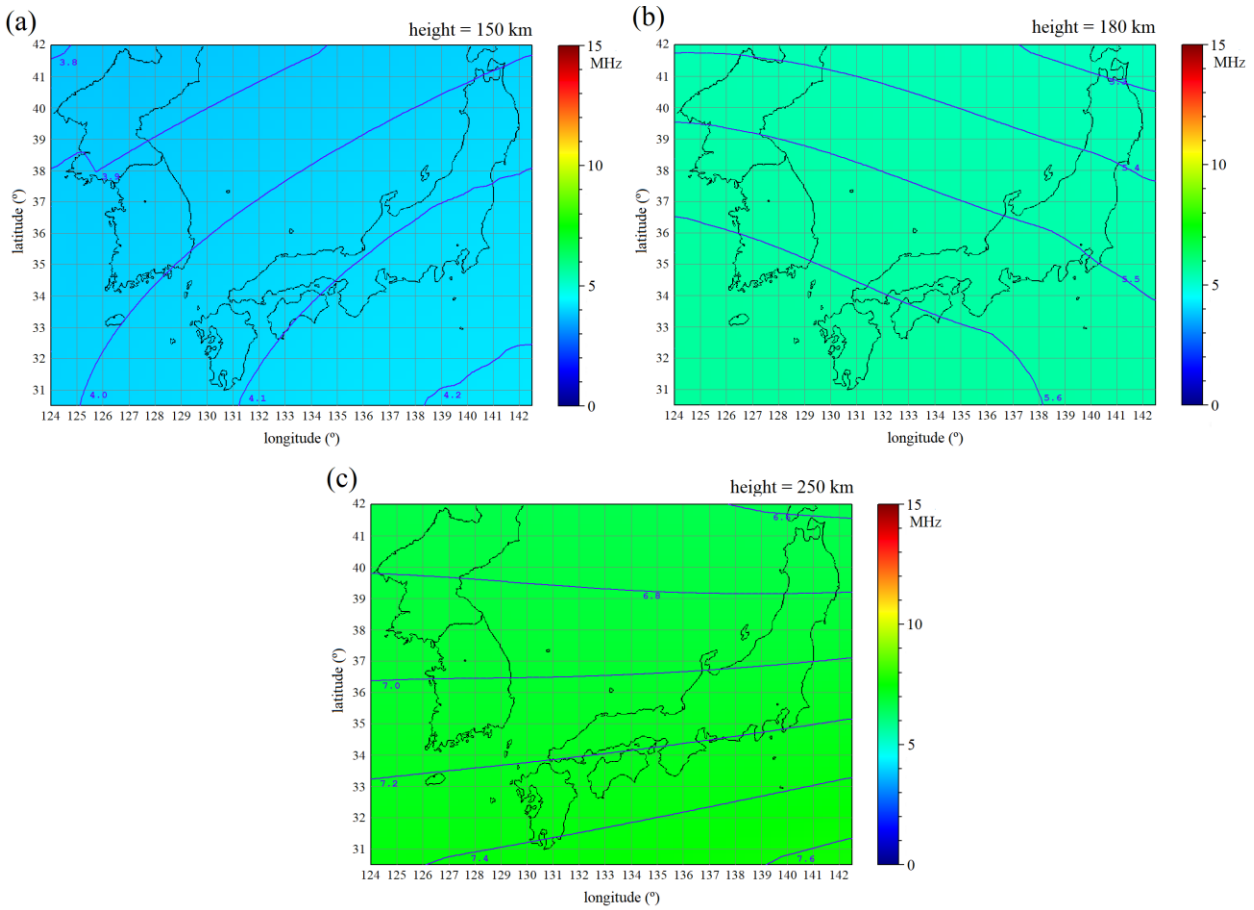

Fig. 7.7. Maps of $f_p(\varphi,\lambda)$ for h=150 km (a), h=180 km (b), and h=250 km (c), obtained for October 5, 2016 at 01.00 UT through the RATIM ingestion of both retrieved $f_p(h)$ at Jeju (South Korea, 33.4° N, 126.3° E) and Icheon (South Korea, 37.1° N, 127.5° E), and OIASA autoscaled MUF values from the radio-link between Kokubunji (Japan, 35.7° N, 139.5° E) and Icheon (South Korea, 37.1° N, 127.5° E).

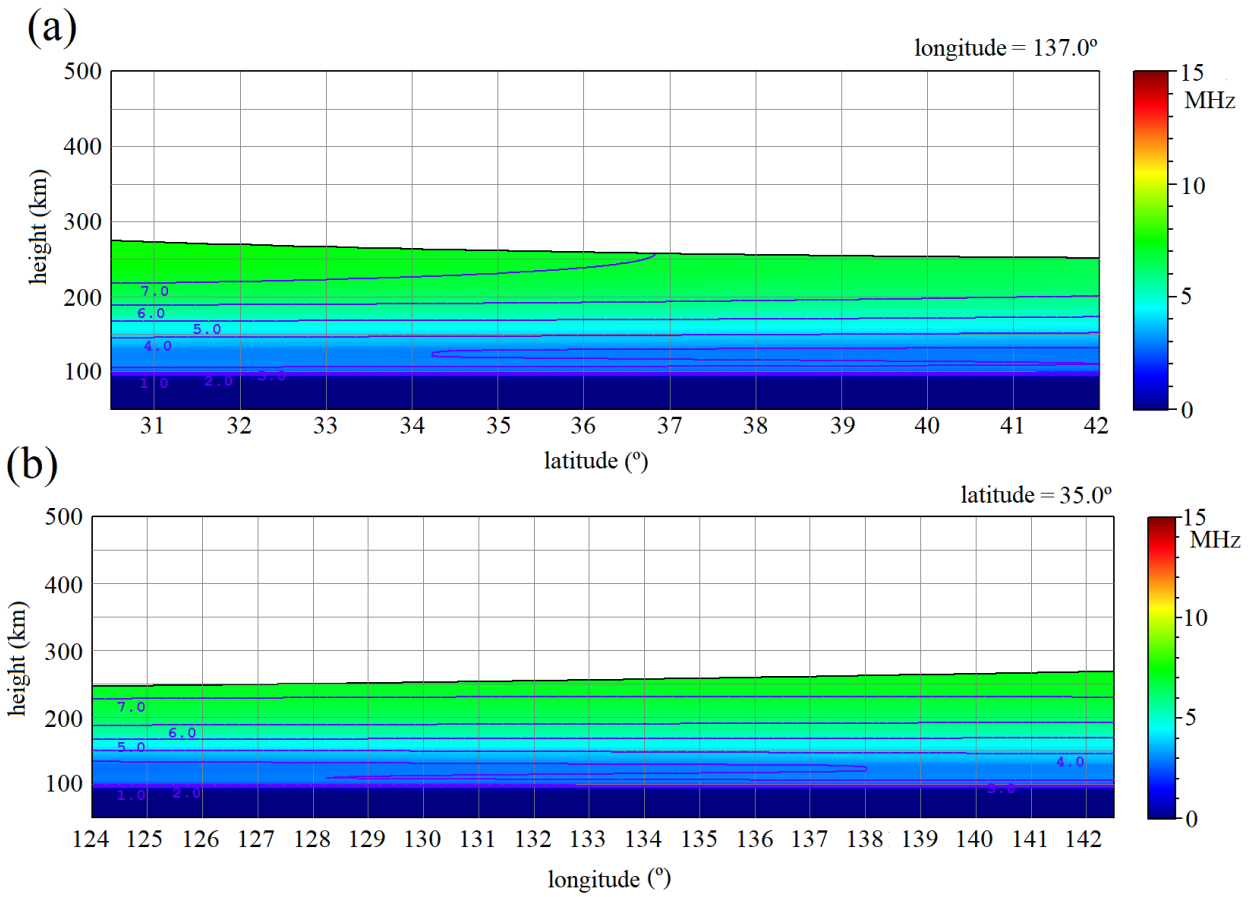

Fig. 7.8. Maps of $f_p(h,\lambda)$ for φ=137.0º (a) and $f_p(h,\varphi)$ for λ=35.0º, obtained for October 5, 2016 at 01.00 UT through the RATIM ingestion of both retrieved $f_p(h)$ at Jeju (South Korea, 33.4° N, 126.3° E) and Icheon (South Korea, 37.1° N, 127.5° E), and OIASA autoscaled MUF values from the radio-link between Kokubunji (Japan, 35.7° N, 139.5° E) and Icheon (South Korea, 37.1° N, 127.5° E).

References

[1] Sabbagh, D., Scotto, C., Sgrigna, V., 2016. A regional adaptive and assimilative three-dimensional ionospheric model. Adv. Space Res. 57 (5), 1241-1257, doi:10.1016/j.asr.2015.12.038.

[2] Borovskikh, A. V., 2010. Eikonal equations for an inhomogeneous anisotropic medium. Journal of Mathematical Sciences, Vol. 164, No. 6.

[3] Bianchi, C., Bianchi, S., 2009. Problema generale del ray-tracing nella propagazione ionosferica – Formulazione dellla ray theory e metodo del ray tracing. Rapporti Tecnici INGV, No. 104.

[4] Coleman, C.J., 2011. Point-to-point ionospheric ray-tracing by a direct variational method. Radio Sci. 46, RS5016, doi:10.1029/2011RS004748.

[5] Degiovanni, M., 2017. Private communication.

[6] Clette, F., Svalgaard, L., Vaquero, J.M., Cliver, E.W., 2014. Revisiting the Sunspot Number. A 400-Year Perspective on the Solar Cycle. Space Sci. Rev. 186, 35-103. doi: 10.1007/s11214-014-0074-2.

[7] Bilitza, D., Altadill, D., Truhlik, V., Shubin, V., Galkin, I., Reinisch, B., X. Huang, 2017. International Reference Ionosphere 2016: From ionospheric climate to real-time weather predictions. Space Weather 15, 418‐429, doi:10.1002/2016SW001593.

Summary and conclusions

[1] A regional 3D ionospheric model has been developed, with the aim to build a tool able to provide a realistic representation of the bottom-side ionospheric *N* distribution on regional scale from the ingestion of ionosonde data, with particular reference to oblique ionograms. Despite the advent of new methods for the investigation of the ionosphere, the vertical radio-sounding technique is still the most widely used, as it permits to continuously have reliable real-data with global coverage. The oblique radio-sounding technique can provide information not accessible to the vertical ionospheric sounding and it is also promising for monitoring purposes. Therefore, the Regional Assimilative Three-dimensional Ionospheric Model (RATIM) has been designed to ingest both vertical and oblique ionogram data. More precisely, RATIM has been developed to become part of a system which starts from the vertical and oblique radio-soundings and provides *N* specification on a particular area, exploiting the abilities of modern autoscaling software and using HF ray-tracing techniques. In this work, the problems concerning the automatic interpretation of ionograms, HF ray-tracing techniques, ionospheric modelling, and data assimilation have been addressed.

[2] The first ability implemented in RATIM has been the ingestion of $f_p(h)$ retrieved from vertical ionograms. The procedure consists in minimizing the *RMSD*s between the observed and modeled values of $f_p(h)$ at the points where observations are available, in order to set the best values for some model free parameters, to be regionally applied to overcome the climatological description of the ionosphere.

[3] This ability of the model has been tested in the region of latitude from 36.0º N to 47.5º N and longitude from 6.0º E to 19.0º E in different conditions, assimilating $f_p(h)$ from a pair of adapting stations and performing accuracy tests over a third station. The percentages of success of the adjustment procedure have been higher than 90% in every condition, except in some cases during day-time and geomagnetic disturbances, and adapted $f_p(h)$ *RMSD*s have been always between 0.2 MHz and 0.6 MHz, representing a good degree of adaptability. *RMSD*s at the test station, almost always under 1 MHz, have not shown a clear relation with the geomagnetic activity, demonstrating a certain irregular fluctuation. However, f_oF_2 *RMSE* and the relative improvement over climatology in Rome have been compared with those obtained for the SWIF model at middle latitudes, highlighting a better performance of RATIM in terms of accuracy.

[4] Data analysis considering all available data and only validated ones have been compared, confirming that erroneous input data affects the model performances in terms of accuracy. However, a certain capability of the model to reject poor-quality data is suggested from the results, even though the percentage of accepted low-quality input data is still high (73.49%).

[5] A further test has been performed on the same area during the March 20, 2015 partial solar eclipse over the same area, improving RATIM performance by adding new empirical formulations for the ionospheric critical frequencies during solar eclipse conditions. Results obtained in terms of adaptability and accuracy have been promising, being both the adapting and test mean *RMSD*s below 0.4 MHz, both considering all available data and using only validated $f_p(h)$.

[6] In order to achieve improvements on oblique ionograms autoscaling, this work includes a contribution to the development of a method to increase the reliability of MUF values autoscaled by the Oblique Ionograms Automatic Scaling Algorithm (OIASA). Such a method has been applied to a new test-mode oblique ionograms data set recorded in South Korea, from oblique radio-soundings performed between Kokubunji (Japan) and Icheon (South Korea), situated 1079 km apart.

[7] To reduce the HF noise affecting the ionograms, different filters have been applied, choosing the filters threshold values as to obtain the best OIASA performance in terms of rejection of ionograms with insufficient information.

The ROC curve method has been used to choose the contrast threshold C_t associated to the best compromise between FPR and TRP for the MUF autoscaling process. T_1=6.5 dB and T_2=0.1 have been chosen as thresholds for the filters, and C_t=162 for the contrast, obtaining a TPR greater than 86.3% and a FPR less than 7.9%.

[8] To improve the reliability of the autoscaled MUF values, a further filtering procedure has been applied, based on the association of a quality factor Q to each MUF autoscaled. This is made converting the oblique ionograms in vertical equivalent ones to be processed by Autoscala, and evaluating the discrepancies between f_oF_2 values obtained from the MUF and the vertical ionogram autoscaling. The ROC curve method has been used to choose the best Q threshold for the filter, in accordance to the best performance obtained by the entire system to discard ionograms lacking sufficient information. Q_t=4.7MHz has been set, reducing the FPR of about 2.4%, versus a reduction of the TPR of only about 0.6%.

[9] For the MUF assimilation in RATIM, the application of a HF ray-tracing algorithm is needed, in order to achieve ionospheric radio-propagation modelling capability. A ray-tracing technique based on the ray equation has been used for the simulation of the ground range D between the end points of an oblique radio-sounding from the corresponding MUF, when the presence of the EMF and collisions is neglected. A simplified ionosphere between the transmitter and the receiver has been assumed, extending to the whole radio-propagation channel the same parabolic vertical profile constrained to some F_2 characteristics dependent to the RATIM free parameters.

[10] A method for the MUF assimilation in RATIM has been proposed, introducing a further condition for the adapting to be effective. This condition is based on the comparison between the real and the simulated D values associated to the ingested MUF. The comparison is performed for each combination of values assumed by the RATIM free parameters, tested during the $f_p(h)$ ingestion, when a threshold in ΔD discards cases of simulated D not enough close to the real value.

[11] A preliminary study of the combined vertical and oblique radio-soundings data assimilation procedure has been carried out over the region of latitude from 30.5º N to 42.0º N, and longitude from 124.0º E to 142.5º E. $f_p(h)$ from a pair of adapting stations have been ingested, along with MUF values autoscaled by OIASA from Kokubunji-Icheon ionograms. The obtained averaged adapted $f_p(h)$ *RMSD* values confirm the good degree of adaptability of the model, being always less than 0.4 MHz. The percentage of success of the adjustment procedure drops from 84.29% to 67.14% when MUF values are assimilated setting ΔD_t=50 km, up to 63.57% setting ΔD_t=50 km, as a consequence of the poor-quality data rejection ability. Some cases suggest that it even improves assimilating autoscaled MUF values, as in this case the ingestion of bad $f_p(h)$ fails more often. Conversely, *RMSD*s have not been nearly influenced by the MUF assimilation procedure, whereas averaged ΔD values obtained when the MUFs are ingested decrease lowering the threshold ΔD_t, suggesting a better degree of adaptability for ΔD_t=20 km than for ΔD_t=50 km.

[12] The results obtained applying RATIM in different operative conditions can be assessed as promising, regarding its integration in a more complex system for the automatic interpretation of vertical and oblique ionograms. Indeed, a system suitable to accomplish this task needs to different modules communicating each other in order to achieve improved abilities. The successful application of RATIM in conjunction with the systems for the automatic interpretation of vertical and oblique ionograms, and for HF ray-tracing applications, paves the way to new methods for the ionosonde data assimilation in order to achieve an increasingly realistic representation of the actual bottom-side ionosphere. Although computational times for the data ingestion in the model are still not suitable to be operative, future efforts oriented to develop faster algorithms and procedures for the automatic communication between different systems, could be directed in order to obtain an improved modelling capability to be applied in real-time.

[13] Further efforts must be also oriented to improve the ionospheric modeling. In particular, the modeling of the E valley should be furtherly studied, along with the shape of the F_1 region. This could be done by comparing

different well-established models with new data set from different sources, in particular Incoherent Scatter Radar (ISR). New tests on the RATIM ability to fit the actual ionosphere in different conditions must also be run, widening the data set and including different regions, even at different latitudes. Besides, RATIM performance during different hours and perturbed conditions must be furtherly studied, improving its adaptability when significant changes in the profiles shape occur, as for instance, during dawn and dusk hours. Moreover, differences in day-time and night-time condition over different adapting stations may occur simultaneously, giving rise in modelling and data assimilation difficulties.

[14] Much still remains to be done in the field of the automatic scaling of the oblique ionograms, too. The OIASA ability to scale the MUF for different radio-links and in different conditions should be further tested, along with its capability to discard ionograms with insufficient informations and erroneous output. The possibility to obtain further information from the oblique ionograms, in addition to the MUF between the receiver and the transmitter, must be explored, with their potential assimilation in RATIM.

[15] The achievement of the goal of retrieving the electron density distribution in a radio-propagation channel of an oblique radio-sounding from the corresponding ionogram still requires much progress. The combined use of ionospheric and radio-propagation model capability could be exploited to generate simulated oblique ionograms to be compared to measured ones, obtaining a realistic representation of the electron density distribution through the target function method. In this context, improvements on ray-tracing techniques in anisotropic media, could lead to a more reliable characterization of the ionosphere in the signals propagation area.

The contents of this work have been described in the following scientific papers:

[1] Sabbagh, D., Scotto, C., Sgrigna, V. (2016). A regional adaptive and assimilative three-dimensional ionospheric model. Adv. Space Res. 57 (5), 1241-1257, doi:10.1016/j.asr.2015.12.038.

[2] Ippolito, A., Scotto, C., Sabbagh, D., Sgrigna, V., Maher, P. (2016). A procedure for the reliability improvement of the oblique ionograms automatic scaling algorithm. Radio Sci. 51, doi:10.1002/2015RS005919.

And have been presented at the following international conferences:

[1] Sabbagh, D.*, Scotto, C., Sgrigna, V. A regional adaptive and assimilative 3D ionospheric model. Oral presentation at URSI AT-RASC 2015, Gran Canaria, Canary Islands (Spain), May 18 -25, 2015.

[2] Ippolito, A.*, Scotto, C., Sabbagh, D., Sgrigna, V. A procedure for the automatic scaling of oblique ionograms. Oral presentation at URSI AT-RASC 2015, Gran Canaria, Canary Islands (Spain), May 18 -25, 2015.

[3] Sabbagh, D.*, Scotto, C., Sgrigna, V. Improvements on f_oF_1 estimation at polar regions. Oral presentation at EGU General Assembly 2016, Vienna (Austria), April 17-22, 2016.

[4] Ippolito, A.*, Settimi, A., Scotto, C., Sabbagh, D., Sgrigna, V. Effect of Solar Eclipse of March 20, 2015 on the Ionosphere. Poster at EGU General Assembly 2016, Vienna (Austria), April 17-22, 2016.

[5] Sabbagh, D.*, Ippolito, A., Scotto, C., Bullett, T., Mabie, J., Sgrigna, V. OIASA application to oblique radio-sounding data recorded in Korea. Poster at EGU General Assembly 2017, Vienna (Austria), April 23-28, 2017.

Besides, a paper on the ionospheric effects of the March 20, 2015 partial solar eclipse over Italy is under development, and a paper on the contribution to automatic scaling of vertical ionograms is planned.